

**UCLA**

**UCLA Electronic Theses and Dissertations**

**Title**

Structure-based Studies on Tau Protein Aggregation and Toxicity

**Permalink**

<https://escholarship.org/uc/item/1xw9w4zr>

**Author**

Chang, Howard W.

**Publication Date**

2013

Peer reviewed|Thesis/dissertation

UNIVERSITY OF CALIFORNIA

Los Angeles

Structure-based Studies on Tau Protein Aggregation and Toxicity

A dissertation submitted in partial satisfaction of the requirements for the  
degree Doctor of Philosophy in Biochemistry & Molecular Biology

By

Howard W Chang

2013

© Copyright by  
Howard W. Chang  
2013

# ABSTRACT OF THE DISSERTATION

## Structure-based Studies on Tau Protein Aggregation and Toxicity

by

Howard W. Chang

Doctor of Philosophy in Biochemistry

University of California, Los Angeles, 2013

Professor David S. Eisenberg, Chair

Tau protein aggregates represent a type of amyloid that are the pathological hallmark of over 20 neurodegenerative diseases, termed tauopathies. These include Alzheimer's disease, progressive supranuclear palsy, and frontotemporal dementia and parkinsonism linked to chromosome 17 (FTDP-17). Given the association between the presence of tau aggregates and pathology, the field has a clear interest in determining whether said aggregates can be prevented, and if doing so would be a viable therapeutic strategy. Yet, much emerging evidence implicates soluble oligomers formed from the same protein to be the toxic species in many amyloid diseases. There is thus also a substantial effort devoted to identifying and characterizing these oligomers.

To see whether a rationally-designed peptidic inhibitor of tau fibril formation works as designed, I adapted and refined a kinetic fluorescence-based assay to test candidate inhibitors in two model systems. Using Nanogold particles, I also developed a new negative-stain electron microscopy-based method to ascertain whether an effective inhibitor actually blocks aggregation as designed, and employed mass-per-unit-length measurements from scanning transmission electron microscopy to support the findings. Using covalently-labeled fibrillogenic peptides, I also tried to create a FRET-based assay to screen for compounds that dissolve pre-formed fibrils. Shifting from working exclusively on insoluble assemblies, I later characterized segments from tau protein that we hypothesized would form toxic oligomers. I did this using a combination of cytotoxicity assays and biochemical methods.

This dissertation describes my findings. I determined that the inhibitors specifically block tau fibril formation, and that they indeed do so by capping and preventing elongation of nascent filaments. I also was able to show that a FRET-based disaggregation assay is viable, although no effective compounds were identified in a pilot screen. And finally, I identified a segment of tau protein that exhibits characteristics suggesting that it is the region responsible for tau's forming toxic oligomers.

The dissertation of Howard W. Chang is approved.

---

James U. Bowie

---

Reid C. Johnson

---

David S. Eisenberg, Committee Chair

University of California, Los Angeles

2013

## DEDICATION PAGE

I dedicate this work to my parents, Belle and Michael, and to my wife, Anni.

# Table of Contents

|   |     |
|---|-----|
| CHAPTER 1: INTRODUCTION AND DISSERTATION LAYOUT .....   | 1   |
| CHAPTER 2: STRUCTURE-BASED DESIGN OF NON-NATURAL AMINO-ACID<br>INHIBITORS OF AMYLOID FIBRIL FORMATION ..... | 6   |
| CHAPTER 3: THE SUPRAMOLECULAR STRUCTURE OF TAU FIBRILS .....  | 48  |
| CHAPTER 4: DEVELOPMENT OF A HIGH-THROUGHPUT SCREENING ASSAY FOR<br>DISAGGREGANTS OF STERIC ZIPPERS .....    | 80  |
| CHAPTER 5: TOWARDS ELUCIDATION OF THE MECHANISM OF TOXICITY IN<br>TAUOPATHIES .....                         | 109 |



## List of Figures and Tables

|  |    |
|--|----|
| <b>Figure 2.1.</b> Design and Characterization of Peptide Inhibitors of Amyloid Fibril Formation .....                     | 8  |
| <b>Figure 2.2.</b> Designed D-peptide Delays Tau K12 Fibril Formation in a Sequence-specific Manner .....                  | 8  |
| <b>Figure 2.3.</b> Mechanism of Interaction.....   | 9  |
| <b>Figure 2.4.</b> Designed Non-natural Peptide Inhibits <sup>248</sup> PAP <sup>286</sup> Fibril Formation .....          | 9  |
| <b>Figure 2.5 (S1).</b> D-TLKIVW Design Model .....  | 15 |
| <b>Figure 2.6 (S2).</b> Other Designed D-amino Acid Tau Inhibitor Models .....   | 17 |
| <b>Figure 2.7 (S3).</b> Steric Repulsion Between D-TLKIVW and VQIVYK Molecules Disrupts Fibril Growth .....                | 19 |
| <b>Figure 2.8 (S4).</b> Designed D-peptides Delay VQIVYK and Tau K12 Fibril Formation .....                                | 20 |
| <b>Figure 2.9 (S5).</b> D-TLKIVW Delays Fibril Formation in a Ratio-dependent Manner.....                                  | 22 |
| <b>Figure 2.10 (S6).</b> D-TLKIVW Decreases the Fibril Propagation Rate of VQIVYK and the Tau Constructs K12 and K19 ..... | 24 |
| <b>Figure 2.11 (S7).</b> Scrambled Inhibitors Demonstrate Sequence Specificity in the Design Model .....                   | 26 |
| <b>Figure 2.12 (S8).</b> L-TLKIVW Diastereomer Has Little Effect on Tau Fibril Formation .....                             | 28 |

|   |    |
|---|----|
| <b>Figure 2.13 (S9).</b> D-TLKIVW Is Not a General Inhibitor of Fibril Formation .....  | 30 |
| <b>Figure 2.14 (S10).</b> Quantification of Nanogold-labeled D-TLKIVW Bound to K19 Fibrils .....  | 31 |
| <b>Figure 2.15 (S11).</b> D-TLKIVW Interacts with VQIVYK and K19 Fibrils .....  | 32 |
| <b>Figure 2.16 (S12).</b> The 500 MHz <sup>1</sup> H Spectra of D-TLKIVW and D-LKTWIV .....   | 33 |
| <b>Figure 2.17 (S13).</b> D-TLKVIW Does Not Interact with Soluble VQIVYK .....  | 34 |
| <b>Figure 2.18 (S14).</b> D-TAKIVW Has Little Effect on Tau Fibril Formation .....  | 35 |
| <b>Figure 2.19 (S15).</b> Binding Orientations of Designed Inhibitor of <sup>248</sup> PAP <sup>286</sup> Fibril Formation .....                                    | 37 |
| <b>Figure 2.20 (S16).</b> The Chemical Structure of the Non-natural Peptide Trp-His-Lys-chAla-Trp-hydroxyTic (WW61) .....   | 39 |
| <b>Figure 2.21 (S17).</b> Inhibitory Effect of the Designed Peptide WW61 on Seeded <sup>248</sup> PAP <sup>286</sup> Fibril Formation .....                         | 40 |
| <b>Figure 2.22 (S18).</b> Inhibitory Effect of the Designed Peptide, WW61, on Unseeded <sup>248</sup> PAP <sup>286</sup> Fibril Formation .....                     | 41 |
| <b>Figure 2.23 (S19).</b> The Non-natural Peptide WW61 Shows a Ratio-dependent Inhibition Effect on Seeded <sup>248</sup> PAP <sup>286</sup> Fibril Formation ..... | 42 |
| <b>Figure 2.24 (S20).</b> Negative-stain Electron Micrographs Show the Effect of the Inhibitor WW61 on <sup>248</sup> PAP <sup>286</sup> Fibril Formation .....     | 43 |
| <b>Figure 2.25 (S21).</b> No Inhibitory Effect of the Control Peptides GIHKQK and PYKLWN on Seeded <sup>248</sup> PAP <sup>286</sup> Fibril Formation .....         | 44 |
| <b>Figure 2.26 (S22).</b> Control HIV Infectivity Assays .....  | 45 |
| <b>Table 2.1 (S1).</b> Comparison of D-peptides and Controls .....  | 46 |
| <b>Table 2.2 (S2).</b> Data Collection and Refinement Statistics (Molecular Replacement) .....  | 47 |
| <b>Table 3.1.</b> Diseases Associated with Tau Aggregation .....  | 62 |

|  |     |
|--|-----|
| <b>Figure 3.1.</b> The Complete Amino Acid Sequence of Full Length Human Tau (htau40) .....  | 63  |
| <b>Figure 3.2.</b> Domain Architecture of Human Tau Isoforms .....   | 64  |
| <b>Figure 3.3.</b> Negatively Stained Transmission Electron Micrographs of Nanogold-labeled Inhibitor Apparently Bound Along the Side of K19 Fibrils ..... | 65  |
| <b>Figure 3.4.</b> Bar Diagrams of Full Length Tau and K19 .....   | 66  |
| <b>Figure 3.5.</b> Transmission Electron Micrographs of K19 Fibrils .....  | 67  |
| <b>Figure 3.6.</b> Scanning Transmission Electron Micrographs of K19 Fibrils .....   | 68  |
| <b>Figure 3.7.</b> Validation of the Correction Factor Used to Determine MPL Values of K19 Fibrils .....   | 69  |
| <b>Figure 3.8.</b> MPL Measurements of K19 Fibrils as Determined by STEM .....   | 70  |
| <b>Table 4.1.</b> Small Molecules Used to Monitor Amyloid Aggregation .....  | 92  |
| <b>Figure 4.1.</b> FRET Probes Used to Monitor VQIVYK Aggregation .....  | 93  |
| <b>Figure 4.2.</b> Formation of a Steric Zipper Induces FRET in Labeled VQIVYK .....   | 94  |
| <b>Figure 4.3.</b> FRET Activity in DV7W Is Correlated with Amyloid Fibril Formation .....   | 95  |
| <b>Figure 4.4.</b> Aggregation-induced FRET in DV7W is Reversible .....  | 96  |
| <b>Figure 4.5.</b> Guandinium Hydrochloride (GdHCl) Dissolved DV7W Fibrils in a Dose-dependent Manner .....  | 97  |
| <b>Figure 4.6.</b> Monitoring Fluorescence at Either 340 or 480 nm Is Suitable for a High Throughput Screen of DV7W Disaggregation .....                   | 98  |
| <b>Figure 4.7.</b> Results from a Pilot High Throughput Screen (HTS) .....   | 99  |
| <b>Table 5.1.</b> Tau Tandem Repeat Constructs Predicted to Form Cylindrin-like Assemblies .....   | 121 |
| <b>Figure 5.1.</b> The 3D Profile Method Predicts that TauTR1, TauTR5, and TauTR6 will Form Amyloid-like Fibrils, but not TauTR2 .....                     | 122 |

|  |     |
|--|-----|
| <b>Figure 5.2.</b> Transmission Electron Micrographs of Amyloid-like Fibrils Formed by Tau Tandem Repeats TauTR1, TauTR5, and TauTR6 ..... | 123 |
| <b>Figure 5.3.</b> MTT Assays Indicate that a Soluble Preparation of TauTR1 Is Toxic to a Human Cell Line .....                            | 124 |
| <b>Figure 5.4.</b> The Toxic Form of TauTR1 Is in an Oligomeric State .....  | 125 |

## Acknowledgments

First and foremost, I would like to thank David Eisenberg, my doctoral thesis advisor. I am thankful not only for his considerable scientific guidance, but also for serving as a role model for professionalism and his perpetually optimistic outlook. I know that when I face difficult situations in the future, I will always think of what Dr. Eisenberg would do. Aside from our direct interactions, I am also grateful for his ability to attract laboratory members of such high caliber, for they have made my laboratory experience all the more positive as well.

Over the last 5 years, I have crossed paths with dozens of graduate students, postdoctoral scholars, and research staff in Dr. Eisenberg's, other professors', and campus core labs: Prof. Rob Clubb, Prof. Joe Loo, Prof. April Pyle, Prof. Ken Houk, Prof. Heather Maynard, Prof. Dave Teplow, Robert Damoiseaux, Winnie Hwang, Rachel Loo, Martin Phillips, Greg Khitrov, Sergey Ryazantsev, Tracy Blois, Mary Jane Knight, Ryan Stafford, Heedok Hong, Nathan Joh, Liz Massey-Gendel, Megan Plotkowski, Scott Robson, Valerie Villareal, Huiying Li, Rich Llewellyn, Chris Miller, Rebecca Nelson, Marcin Apostol, Jed Wiltzius, Poh Teng, Luki Goldschmidt, Heather MacFarlane, Minglei Zhao, Andrew Min, Anni Zhao, Angie Soriaga, Natalie Anderson, Riki Stevenson, Einat Sprinzak, James Stroud, Arturo Medrano-Soto, Zhefeng Guo, Jacques-Philippe Colletier, Linda Miallau, Meytal Landau, Cong Liu, Dan Li, Jiyong Park, Lin Jiang, Boris Brumshtein, Alice Soragni, Lorena Saelices-Gomez, Dan Anderson, Duilio Cascio, Michael Sawaya, Lukasz Salwinski, Lisa Johnson, Jose Rodriguez, Sarah Griner, Smriti Sangwan, Liz Guenther, Weixia Yu, Mari Gingery, Tom Holton, Magda Ivanova, Jason Navarro, Michael Collazo, and Alex Lisker. Big and small, each has influenced my scientific growth, and whatever success I had in graduate school would not have been possible without them.

I would like to especially thank Stuart Sievers, who was exceptionally generous with his time and mentored me closely over my first few years. I would also like to extend a special thanks to Rebecca Nelson, who took on the unenviable task of sitting down to explain to me the theories and mathematics behind protein crystallography.

I thank the members of my thesis committee, Dr. James Bowie and Dr. Reid Johnson, for taking the time to hear my crazy ideas with good humor, and for volunteering ideas when inspiration temporarily ran dry.

I am grateful for support from the Ruth L. Kirschstein National Research Service Award (GM007185), NIH, and HHMI.

And, of course, I thank my family for their unending support and motivation.

Completing graduate school can be a trying endeavor, with many difficult times. But thanks to the many individuals helping and encouraging me along the way, I can safely say that there were never *bad* times. Thank you all.

## VITA

|           |   |
|-----------|---|
| 2004-2005 | Crew Chief<br>Skysurfer Hot Air Balloon Company   |
| 2005      | B.S. in Biochemistry and Cell Biology<br>University of California, San Diego  |
| 2005-2006 | Research Assistant<br>Neurome, Inc.   |
| 2007      | University Fellowship<br>University of California, Los Angeles  |
| 2007      | Teaching Assistant<br>Department of Chemistry and Biochemistry,<br>University of California, Los Angeles                          |
| 2009      | MBI Lake Arrowhead Retreat Best Poster Award<br>Molecular Biology Institute<br>University of California, Los Angeles              |
| 2008-2011 | Cellular and Molecular Biology Predoctoral Training Grant<br>Molecular Biology Institute<br>University of California, Los Angeles |
| 2008-2011 | Chemistry-Biology Interface Training Program (Associate)<br>University of California, Los Angeles                                 |

## PUBLICATIONS AND PRESENTATIONS

**Chang, H. W.**, Sievers, S. A., Karanicolas, J., Baker, D., and Eisenberg, D. S. Structure-based Inhibitors of Amyloid Fibril Formation. Poster presented at the 2009 David S. Sigman Lecture and Symposium. Los Angeles, CA. January 30, 2009.

**Chang, H. W.**, Sievers, S. A., Karanicolas, J., Baker, D., and Eisenberg, D. S. Structure-based Design of a D-peptide Inhibitor of Tau Fibril Formation. Poster presented at the West Coast Protein Crystallography Workshop XIX. Pacific Grove, CA. April 5 – 8, 2009.

Perugia, E., **Chang, H. W.**, Eisenberg, D. S., and Addadi, L. The Atomic Basis of the Right-handed Chirality Exhibited by Serum Amyloid A. Poster presented at the FASEB Summer Research Conference – Amyloid Fibril Formation and Protein Misfolding: Molecular Mechanisms and Cellular Effects. Snowmass Village, CO. June 28 – July 3, 2009.

**Chang, H. W.**, Sievers, S. A., Karanicolas, J., Baker, D., and Eisenberg, D. S. Characterizing a Structure-based Peptidic Inhibitor of Amyloid Fibril Formation. Poster presented at the 2009 CBI Day. Los Angeles, CA. August 7, 2009.

Perugia, E., **Chang, H. W.**, Eisenberg, D. S., and Addadi, L. The Atomic Basis of the Right-handed Chirality Exhibited by Serum Amyloid A. Poster presented at the 2009 MBI Annual Lake Arrowhead Retreat. Lake Arrowhead, CA. October 16 – 18, 2009.

**Chang, H. W.**, Sievers, S. A., Karanicolas, J., Baker, D., and Eisenberg, D. S. Characterization of a Structure-based Inhibitor of Tau Fibril Formation. Poster presented at the 2010 CBI Day. Los Angeles, CA. August 6, 2010.

**Chang, H. W.**, Sievers, S. A., Karanicolas, J., Baker, D., and Eisenberg, D. S. Poster presented at the UCLA ACCESS Affinity Fair. Los Angeles, CA. September 15 – 17, 2010.

Sievers, S. A.\*, Karanicolas, J.\*, **Chang, H. W.\***, Zhao, A.\*, Jiang, L.\*, Zirafi, O., Stevens, J. T., Münch, J., Baker, D., and Eisenberg, D. (2011). Structure-based design of non-natural amino-acid inhibitors of amyloid fibril formation. *Nature*. 475, 96-100.

**Chang, H. W.**, Sievers, S. A., Karanicolas, J., Baker, D., and Eisenberg, D. S. Characterization of a Structure-based Inhibitor of Tau Fibril Formation. Poster presented at the 2011 David S. Sigman Lecture and Symposium. Los Angeles, CA. February 24, 2011.

**Chang, H. W.**, and Eisenberg, D. S. A Screen for Compounds to Undo Tau Protein Fibrillization from Alzheimer's Disease. Poster presented at the 2011 CBI Day. Los Angeles, CA. August 5, 2011.



# Chapter 1: Introduction and Dissertation Layout

Over the course of my PhD research, I have investigated the binding mechanism of a structure-based peptidic inhibitor of tau fibril formation, the supramolecular structure of tau fibrils, a high-throughput screening assay for disaggregants of tau steric zippers, and the mechanism of toxicity in tauopathies.

Chapter 2 presents a reprint of our 2011 article in *Nature*, in which we design and characterize structure-based peptide inhibitors of amyloid fibril formation (Sievers et al., 2011). Stuart Sievers and I jointly developed the assay to determine candidate inhibitors' efficacy against the tau protein construct K19, and I refined the protocol to similarly assay the inhibitors' effects on the peptidic model Ac-VQIVYK-NH<sub>2</sub>. In order to confirm that the inhibitor binds as designed, I also designed an assay utilizing Nanogold, a particle used to visualize proteins and peptides under microscopy (Hainfield, 1996). This work not only lent support for the steric zipper model of amyloid fibrils on an atomic level, but it also validated a general approach to generating potential therapeutics against tauopathies and amyloid diseases overall.

Chapter 3 of the dissertation is a manuscript in preparation describing work that follows up on the article presented in chapter 2. In it, I investigate the supramolecular architecture of tau protein fibrils, associated with the neurofibrillary tangles observed in the brains of Alzheimer's disease and tauopathy patients. Joseph Wall at the Brookhaven National Laboratory acquired scanning transmission electron micrographs (Ksiezak-Reding and Wall, 2005) from K19 fibrils which I prepared. Using these micrographs, I recorded mass-per-unit length measurements of the fibrils, and calculated that the fibrils are likely composed of pairs of  $\beta$ -

sheets, supporting the VQIVYK steric zipper our lab had previously modeled to represent the core of tau fibrils (Sawaya et al., 2007). Moreover, the acquired micrographs and measurements derived from them helped to support conclusions we made regarding the binding of a peptide inhibitor of tau fibril formation, detailed in the manuscript contained in the previous chapter.

Chapter 4 describes my development of a high-throughput screen for small molecules capable of breaking apart preformed amyloid fibrils. By affixing components of a FRET pair to the N- and C- termini of the amyloidogenic segment VQIVYK from tau, I developed an assay which would monitor the aggregation state as a function of FRET activity. Previous work had demonstrated a proof-of-concept of this approach, but had never shown the process to be reversible and scalable (Deng et al., 2007). I performed experiments that confirmed FRET activity is correlated with assembly of fibrils, and that loss of FRET is correlated with disassembly of fibrils. I also adapted these observations to make the assay amenable to a high-throughput format using a well-known metric (Zhang et al., 1999). A pilot screen of compounds yielded no effective disaggregants, however, demonstrating the incredible stability of these fibrils, and suggesting that using small molecules may not be a viable strategy to break apart existing fibrils.

Chapter 5 describes experiments that I have done in pursuit of identifying the toxic species of tau aggregate in tauopathies. To date, studies have implicated both insoluble fibrils (Mocanu et al., 2008) and soluble oligomers (Lasagna-Reeves et al., 2012) as the toxic species in these diseases, with the field yet to reach consensus. Building upon a study in our lab identifying cylindrin as a model for toxic oligomers (Laganowsky et al., 2012), Rebecca Nelson identified six segments from tau protein predicted to form similar assemblies. I cloned, produced, purified, and characterized tandem repeats of these segments, finding one that forms a toxic oligomer .

The work that I have performed support the view that soluble oligomers are the toxic species in tau.

## References

Deng, W., Cao, A., and Lai, L. (2007). Detecting the inter-peptide arrangement and maturation process of transthyretin (105-115) amyloid fibril using a FRET pair with short Förster distance. *Biochemical and Biophysical Research Communications*. *362*, 689-694.

Hainfeld, J. F. (1996). Labeling with nanogold and undecagold: techniques and results. *Scanning Microscopy. Supplement*. *10*, 309-22.

Ksiezak-Reding, H., and Wall, J. S. (2005). Characterization of paired helical filaments by scanning transmission electron microscopy. *Microscopy Research and Technique*. *67*, 126-140.

Laganowsky, A., Liu, C., Sawaya, M. R., Whitelegge, J. P., Park, J., Zhao, M., Pensalfini, A., Soriaga, A. B., Landau, M., Teng, P. K., Cascio, D., Glabe, C., and Eisenberg, D. (2012). Atomic view of a toxic amyloid small oligomer. *Science*. *335*, 1228-1231.

Lasagna-Reeves, C. A., Castillo-Carranza, D. L., Sengupta, U., Sarmiento, J., and Troncoso, J., Jackson, G. R., and Kaye, R. (2012). Identification of oligomers at early stages of tau aggregation in Alzheimer's disease. *FASEB Journal*. *26*, 1946-1959.

Mocanu, M. M., Nissen, A., Eckermann, K., Khlistunova, I., Biernat, J., Drexler, D., Petrova, O., Schönig, K., Bujard, H., Mandelkow, E., Zhou, L., Rune, G., and Mandelkow, E. M. (2008). The potential for beta-structure in the repeat domain of tau protein determines aggregation, synaptic decay, neuronal loss, and coassembly with endogenous tau in inducible mouse models of tauopathy. *Journal of Neuroscience*. *28*, 737-748.

Sawaya, M. R., Sambashivan, S., Nelson, R., Ivanova, M. I., Sievers, S. A., Apostol, M. I., Thompson, M. J., Balbirnie, M., Wiltzius, J. J., McFarlane, H. T., Madsen, A. Ø., Riek, C., and

Eisenberg, D. (2007). Atomic structures of amyloid cross- $\beta$  spines reveal varied steric zippers. *Nature*. *447*, 453–457.

Sievers, S. A., Karanicolas, J., Chang, H. W., Zhao, A., Jiang, L., Zirafi, O., Stevens, J. T., Münch, J., Baker, D., and Eisenberg, D. Structure-based design of non-natural amino-acid inhibitors of amyloid fibril formation. (2011). *475*, 96-100.

Zhang, J. H., Chung, T. D., and Oldenburg, K. R. (1999). A simple statistical parameter for use in evaluation and validation of high throughput screening assays. *Journal of Biomolecular Screening*. *4*, 67-73.

## Chapter 2: Structure-based Design of Non-natural Amino-acid Inhibitors of Amyloid Fibril Formation

This chapter is a reprint of:

Structure-based design of non-natural amino-acid inhibitors of amyloid fibril formation  
Stuart A. Sievers, John Karanicolas, Howard W. Chang, Anni Zhao, Lin Jiang, Onofrio Zirafi,  
Jason T. Stevens, Jan Münch, David Baker, and David Eisenberg.  
*Nature*. 2011 July 07; **475** (96-100)

### Abstract

In this chapter, I present a reprint of an article in which we report the structure-based design of peptidic inhibitors of amyloid fibril formation. Stuart Sievers and I developed and performed kinetic assays to determine the effectiveness of inhibitors against protein and peptide models of tau fibril formation. I also designed and implemented the Nanogold-inhibitor studies that show the inhibitor operates in accordance with the design model. Our work confirms the central role that steric zipper segments play in the context of full-length proteins, and represents a plausible strategy for developing pharmaceuticals against amyloid diseases in general.

## Structure-based design of non-natural amino-acid inhibitors of amyloid fibril formation

Stuart A. Sievers<sup>1\*</sup>, John Karanicolas<sup>2,3\*</sup>, Howard W. Chang<sup>1\*</sup>, Anni Zhao<sup>1\*</sup>, Lin Jiang<sup>1\*</sup>, Onofrio Zirafi<sup>4</sup>, Jason T. Stevens<sup>3</sup>, Jan Münch<sup>4</sup>, David Baker<sup>2</sup> & David Eisenberg<sup>1</sup>

Many globular and natively disordered proteins can convert into amyloid fibrils. These fibrils are associated with numerous pathologies<sup>1</sup> as well as with normal cellular functions<sup>2,3</sup>, and frequently form during protein denaturation<sup>4,5</sup>. Inhibitors of pathological amyloid fibril formation could be useful in the development of therapeutics, provided that the inhibitors were specific enough to avoid interfering with normal processes. Here we show that computer-aided, structure-based design can yield highly specific peptide inhibitors of amyloid formation. Using known atomic structures of segments of amyloid fibrils as templates, we have designed and characterized an all-D-amino-acid inhibitor of the fibril formation of the tau protein associated with Alzheimer's disease, and a non-natural L-amino-acid inhibitor of an amyloid fibril that enhances sexual transmission of human immunodeficiency virus. Our results indicate that peptides from structure-based designs can disrupt the fibril formation of full-length proteins, including those, such as tau protein, that lack fully ordered native structures. Because the inhibiting peptides have been designed on structures of dual- $\beta$ -sheet 'steric zippers', the successful inhibition of amyloid fibril formation strengthens the hypothesis that amyloid spines contain steric zippers.

The finding that dozens of pathologies, including Alzheimer's disease, are associated with amyloid fibrils has stimulated research on fibril inhibition. One approach uses the self-associating property of proteins that form fibrils to poison fibril formation with short peptide segments<sup>6–11</sup>. A second approach is based on screening for molecules that can disrupt fibril formation<sup>12,13</sup>. Here we take a third approach to fibril inhibition: structure-based design of non-natural peptides targeted to block the ends of fibrils. With advanced sampling techniques and by minimizing an appropriate energy function, we identify novel candidate inhibitors computationally from a large peptide space that interact favourably with our template structure. This approach has been made possible by the determination of several dozen fibril-like atomic structures of segments from amyloid-forming proteins<sup>14–16</sup>.

These structures reveal a common motif called a steric zipper, in which a pair of  $\beta$ -sheets is held together by the interdigitation of their side chains<sup>14</sup>. Using as templates the steric-zipper structures formed by segments of two pathological proteins, we have designed inhibitors that cap fibril ends. As we show, the inhibitors greatly slow the fibril formation of the parent proteins of the segments, offering a route to designed chemical interventions and supporting the hypothesis that steric zippers are the principal structural elements of these fibrils.

One of the two fibril-like steric zippers that we have chosen as a target for inhibitor design is the hexapeptide VQIVYK, residues 306–311 of the tau protein, which forms intracellular amyloid fibrils in Alzheimer's disease<sup>17</sup>. This segment has been shown to be important for fibril formation of the full-length protein and itself forms fibrils

with biophysical properties similar to full-length tau fibrils<sup>15,18,19</sup>. Our second template for inhibitor design, identified by the '3D profile' algorithm<sup>20,21</sup>, is the steric-zipper structure of the peptide segment GGVLVN from the amyloid fibril formed by <sup>248</sup>PAP<sup>286</sup>, a proteolytic fragment containing residues 248–286 of prostatic acid phosphatase, a protein abundant in semen. <sup>248</sup>PAP<sup>286</sup> fibrils, also known as semen-derived enhancer of virus infection (SEVI), enhance human immunodeficiency virus (HIV) infection by orders of magnitude in cell culture studies, whereas the monomeric peptide is inactive<sup>22</sup>.

Our computational approach to designing non-natural peptides that inhibit fibril formation is summarized in Fig. 1 for the VQIVYK segment of tau protein; the same general strategy is used for the GGVLVN segment of <sup>248</sup>PAP<sup>286</sup>. In both systems, we design a tight interface between the inhibiting peptide and the end of the steric zipper to block additional segments from joining the fibril. By sampling L or D amino acids, or commercially available non-natural amino acids, we can design candidate inhibitors with side chains that maximize hydrogen bonding and hydrophobic interactions across the interface.

We propose that the steric-zipper structures of the VQIVYK and GGVLVN segments represent the spines of the fibrils formed by the parent proteins containing these segments. Supporting our hypothesis are our results that D-amino-acid inhibitors designed on the VQIVYK steric-zipper template inhibit fibril formation not only of the VQIVYK segment, but also of two tau constructs, K12 and K19<sup>23,24</sup> (Fig. 2a). Similarly, the peptide composed of non-natural amino acids designed on the GGVLVN template inhibits the fibril formation of <sup>248</sup>PAP<sup>286</sup> and greatly inhibits the HIV infectivity of human cells in culture.

To design a D-amino-acid hexapeptide sequence that interacts favourably with the VQIVYK steric zipper<sup>15</sup>, and prevents further addition of tau molecules to the fibril, we used the Rosetta software<sup>25</sup>. This led to the identification of four D-amino-acid peptides: D-TLKIVW, D-TWKLVV, D-DYYFEF and D-YVIER, in which the prefix signifies that all  $\alpha$ -carbon atoms are in the D configuration (Fig. 2b, c, Supplementary Figs 1 and 2 and Supplementary Table 1). In the D-TLKIVW design model (Fig. 2b, c and Supplementary Fig. 1), the inhibitor packs tightly across the top of the VQIVYK steric-zipper structure, maintaining all main-chain hydrogen bonds. The side-chain hydrogen bonding between layers of stacked Gln307 residues is replaced in the designed interface by an interaction with D-Lys3. Several hydrophobic interactions between D-TLKIVW and the two VQIVYK  $\beta$ -strands contribute to the favourable binding energy (Supplementary Table 1). In the design, the D-peptide blocks the addition of another layer of VQIVYK, both above the D-peptide and across on the mating  $\beta$ -sheet (Supplementary Fig. 3). D-Leu2 of the designed inhibitor prevents the addition of a VQIVYK molecule above it through a steric clash with Ile308 of VQIVYK and on the mating sheet through a clash with Val306 and Ile308 (Supplementary Fig. 3). These steric clashes involving D-Leu2 are intended to block fibril growth.

<sup>1</sup>Departments of Biological Chemistry and Chemistry and Biochemistry, Howard Hughes Medical Institute, UCLA, Box 951970, Los Angeles, California 90095-1570, USA. <sup>2</sup>Department of Biochemistry and Howard Hughes Medical Institute, University of Washington, Seattle, Washington 98195, USA. <sup>3</sup>Center for Bioinformatics and Department of Molecular Biosciences, University of Kansas, 1200 Sunnyside Avenue, Lawrence, Kansas 66045-7534, USA. <sup>4</sup>Institute of Molecular Virology, University Hospital Ulm, Meyerhofstrasse 1, 89081 Ulm, Germany.

\*These authors contributed equally to this work.

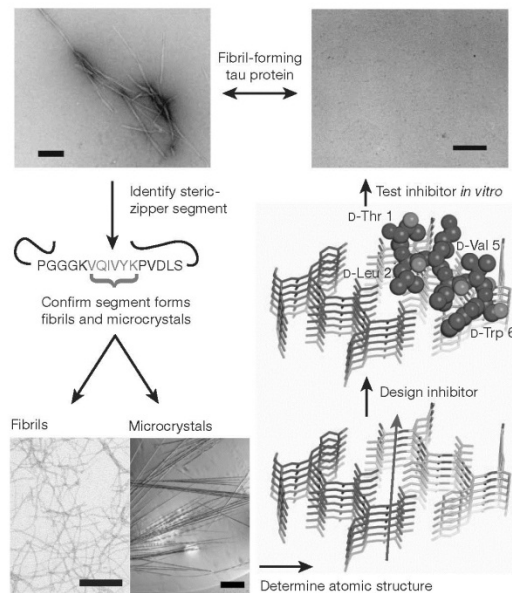


**Figure 1 | Design and characterization of peptide inhibitors of amyloid fibril formation.** Tau constructs form fibrils *in vitro*<sup>24</sup> (top left; scale bar, 200 nm). The VQIVYK segment in isolation forms fibrils and microcrystals (bottom left; fibril scale bar, 200 nm; microcrystal scale bar, 100  $\mu$ m). The atomic structure of the fibril-like VQIVYK segment reveals a characteristic steric-zipper motif<sup>25</sup> comprising a pair of interacting  $\beta$ -sheets (purple and grey) running along the fibril axis (grey arrow) (bottom right). We designed a D-amino-acid peptide to bind to the end of the steric-zipper template and prevent fibril elongation (middle right). The D-peptide (red) is designed to satisfy hydrogen bonds and make favourable non-polar interactions with the molecule below, while preventing the addition of other molecules above and on the opposite  $\beta$ -sheet. As shown *in vitro*, the designed D-peptide prevents the formation of fibrils when incubated with tau K19 (upper right; scale bar, 200 nm).

We used fluorescence spectroscopy and electron microscopy to assess whether the designed D-peptides inhibit the fibril formation of the tau segment VQIVYK and of the tau constructs K12 and K19. Of our designed inhibitors, D-TLKIVW is the most effective (Supplementary Fig. 4). Electron microscopy, performed after three days, verified that incubation with equimolar D-TLKIVW prevents K19 fibril formation, which would otherwise have occurred within the elapsed time (Fig. 1, upper right). D-TLKIVW delays fibril formation of VQIVYK, K12 and K19 even when present in sub-equimolar concentration (Supplementary Fig. 5). A fivefold molar excess of D-TLKIVW delays K12 fibril formation for more than two weeks in some experimental replicates (Supplementary Fig. 5c, d). In tenfold molar excess, D-TLKIVW prevents the fibril formation of K12 for more than 60 hours in the presence of preformed K12 fibril seeds, suggesting that the peptide interacts with fibrils (Fig. 2d). Also, kinetic analysis shows that the fibril elongation rate decreases in the presence of increasing concentrations of inhibitor peptide (Supplementary Fig. 6). The large increase in lag time in unseeded reactions may be due to interactions with small aggregates formed during the process of fibril formation.

To investigate the specificity of the designed inhibitor, we tested scrambled sequence variants of D-TLKIVW that have poor (that is, high) calculated energies and unfavourable packing (Supplementary Table 1). The scrambled peptides D-TIKWVL, D-TIWKVL and D-LKTWIV have little inhibitory effect when present at an equimolar

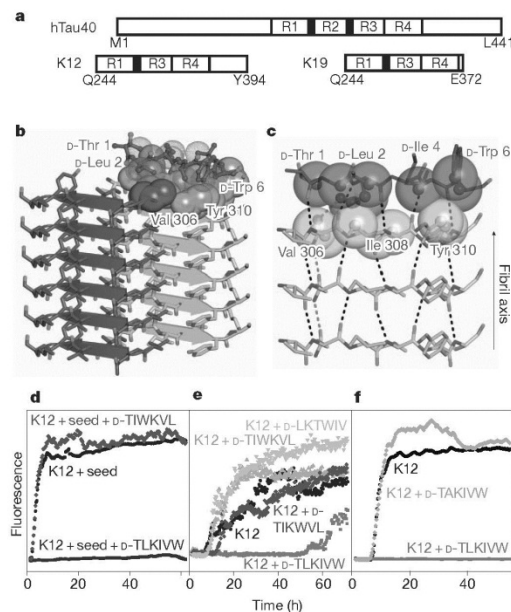


**Figure 2 | Designed D-peptide delays tau K12 fibril formation in a sequence-specific manner.** a, Tau construct composition<sup>25</sup>. The longest human tau isoform found in the central nervous system, hTau40 (Uniprot ID, P10636-8), contains four microtubule-binding repeats, R1 to R4, whereas K12 and K19 lack R2. The black bars at the amino termini of R2 and R3 represent the fibrillogenic segments VQINK and VQIVYK, respectively. b, The inhibitor D-TLKIVW (red) is designed to interact with atoms on both  $\beta$ -strands of the VQIVYK steric zipper (grey) primarily through hydrophobic packing and hydrogen-bonding interactions. c, The inhibitor interacts with the VQIVYK  $\beta$ -strand below. The transparent spheres show where the two molecules interact favourably. Black and red dashes indicate main-chain and side-chain hydrogen bonds, respectively. Stereo views of b and c are shown in Supplementary Fig. 1. d, The seeded fibril formation of 50  $\mu$ M K12 in the presence and absence of a tenfold molar excess of peptide was monitored by Thioflavin S fluorescence. In the presence of the scrambled peptide D-TIWKVL (dark green) and alone (black), seeded K12 fibril formation occurs with almost no lag time. However, D-TLKIVW prevents fibril formation for days (maroon). e, At equimolar concentrations, D-TLKIVW (red) inhibits the fibril formation of 50  $\mu$ M K12. D-TIKWVL (blue), with only three residues scrambled, shows weak inhibition. However, no inhibition is observed for either D-TIWKVL (green) or D-LKTWIV (cyan). f, The replacement of D-Leu 2, designed to clash with VQIVYK on the opposite sheet, with D-Ala eliminates the inhibition of fibril formation.

ratio with VQIVYK, K12 and K19 (Fig. 2e and Supplementary Fig. 7), showing that the inhibition is sequence specific. Also, the diastereomer, L-TLKIVW, is less effective than D-TLKIVW (Supplementary Fig. 8). As a further test of the specificity of our design, we confirmed that D-TLKIVW is unable to block the fibril formation of amyloid- $\beta$ , which also is associated with Alzheimer's disease (Supplementary Fig. 9). This suggests that the D-peptide inhibitor is not general to amyloid systems, but is specific to the VQIVYK interface in tau protein. Such specificity is essential for designed inhibitors if they are not to interfere with proteins that natively function in an amyloid state<sup>3</sup>.

To confirm that the designed D-peptide inhibits in accordance with the design model (Fig. 2b, c and Supplementary Fig. 1), we performed several additional tests. First we visualized the position of the inhibitor D-TLKIVW relative to fibrils of the tau construct K19 using electron microscopy. We covalently linked Monomaleimido Nanogold particles



both to the inhibitor and, separately, to a scrambled hexapeptide, D-LKTWIV. We used a blind counting assay and found that, relative to Nanogold alone, D-TLKIVW shows a significant binding preference for the end of fibrils, in contrast to the scrambled control peptide, D-LKTWIV (Fig. 3a and Supplementary Fig. 10).

As a further test of the model, we used NMR to characterize the binding affinity of D-TLKIVW for tau fibrils. The  $^1\text{H}$  NMR spectra for D-TLKIVW were collected in the presence of increasing concentrations of VQIVYK or K19 fibrils. Because neither K19 nor VQIVYK contains tryptophan, we were able to monitor the  $^1\text{H}$  resonance of the indole proton of the tryptophan in our inhibitor. When bound to a fibril, the inhibitor, D-TLKIVW, is removed from the soluble phase and the  $^1\text{H}$  resonance is diminished<sup>26</sup> (Fig. 3b and Supplementary Fig. 11). As a control, we also measured spectra for the non-inhibiting peptide D-LKTWIV present with D-TLKIVW in the same reaction mixture. As shown in Fig. 3b, the presence of VQIVYK fibrils at a given concentration reduces the D-TLKIVW indole resonance much more than it does the D-LKTWIV indole resonance. Spectra of the two peptides are shown in Supplementary Fig. 12. By monitoring the D-TLKIVW indole resonance over a range of VQIVYK fibril concentrations, we estimate the apparent dissociation constant of the interaction between D-TLKIVW and VQIVYK fibrils to be  $\sim 2\ \mu\text{M}$  (Supplementary Fig. 11a and Methods). This value corresponds to a standard free binding energy of  $\sim 7.4\ \text{kcal mol}^{-1}$ , with  $\sim 2.5\ \text{kcal mol}^{-1}$  from non-polar interactions and  $\sim 4.9\ \text{kcal mol}^{-1}$  from six hydrogen bonds (Methods). Repeating the NMR binding experiment with K19 fibrils yields a similar trend (Supplementary Fig. 11b). To determine whether D-TLKIVW has affinity for soluble VQIVYK, we measured  $^1\text{H}$  NMR spectra of D-TLKIVW and D-LKTWIV in the presence of increasing amounts of soluble VQIVYK. Only a slight change in the respective chemical shifts of the indole proton peaks of D-TLKIVW and D-LKTWIV is observed, even at a 70-fold molar excess of VQIVYK (Supplementary Fig. 13). This, together with the ability of the peptide to prevent seeded fibril formation, suggests that D-TLKIVW does not interact with monomers but rather with a structured, fibril-like species.

As another test of our design model, we replaced the D-Leu residue with D-Ala in D-TLKIVW. Our structural model suggests that D-Leu 2 of D-TLKIVW is important for preventing tau fibril formation because of its favourable interaction with the Ile residue of the VQIVYK molecule below and with Ile and the first Val of VQIVYK across the steric zipper (Fig. 2b, c and Supplementary Fig. 1). The D-Ala replacement

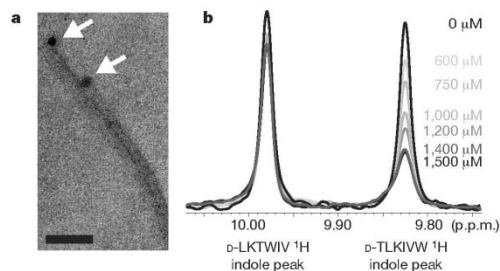


**Figure 3 | Mechanism of interaction.** a, Nanogold covalently bound to D-TLKIVW localizes at the ends (arrows) of two tau K19 fibrils. Scale bar, 50 nm. b, The inhibitor D-TLKIVW binds to fibrils with an estimated affinity constant in the low micromolar range, as shown by the indole proton region of the 500-MHz  $^1\text{H}$  NMR spectra of D-TLKIVW (9.83 p.p.m.) and D-LKTWIV (9.98 p.p.m.) in the presence of increasing concentrations of VQIVYK fibrils. The resonance of the D-TLKIVW indole proton is reduced in the presence of increasing concentrations of VQIVYK fibrils, whereas the indole proton signal for the scrambled control peptide D-LKTWIV is only slightly affected. Fibril solutions contained 0–1,500  $\mu\text{M}$  VQIVYK monomers, as indicated.

eliminates these interactions and, furthermore, removes a steric clash that would occur were another VQIVYK molecule placed across from the inhibitor (Supplementary Fig. 3 and Supplementary Table 1). When the D-Ala variant is incubated with VQIVYK and the tau constructs, it has no inhibitory effect on fibril formation (Fig. 2f and Supplementary Fig. 14). This confirms that D-Leu 2 is critical for the efficacy of D-TLKIVW, consistent with our model.

In summary, although our electron microscopy, NMR and D-Ala replacement results support a model in which the designed peptide D-TLKIVW binds to the ends of tau fibrils, they do not constitute proof that the inhibitors bind exactly as anticipated in the designs (Supplementary Fig. 15).

To expand on our design methodology, we computationally designed an inhibitor of  $^{248}\text{PAP}^{286}$  fibril formation containing non-natural L-amino acids (Fig. 4b and Supplementary Fig. 16), using the GGVLVN structure as a template (Fig. 4a and Supplementary Table 2). This peptide, Trp-His-Lys-chAla-Trp-hydroxyTic (WW61), contains an Ala derivative,  $\beta$ -cyclohexyl-L-alanine (chAla) and a Tyr/Pro derivative, 7-hydroxy-(S)-1,2,3,4-tetrahydroisoquinoline-3-carboxylic acid (hydroxyTic), both of which increase contact area with the GGVLVN template. The non-natural chAla forms hydrophobic interactions with the Leu residue in the steric-zipper interface, and hydroxyTic supports the favourable placement of chAla through hydrophobic packing (Fig. 4b and Supplementary Fig. 16b).

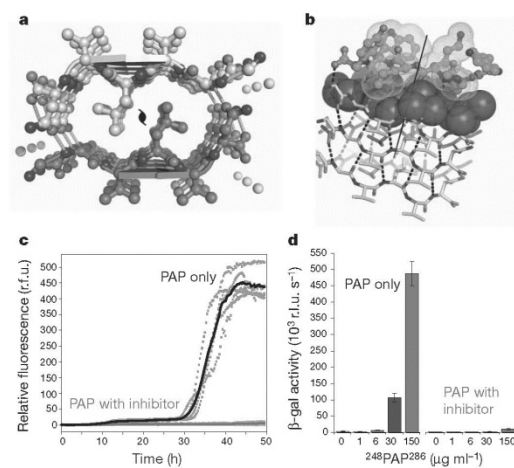


**Figure 4 | Designed non-natural peptide inhibits  $^{248}\text{PAP}^{286}$  fibril formation.** a, The view down the fibril axis of the crystal structure of the GGVLVN steric zipper reveals two mating  $\beta$ -sheets with parallel, in-register  $\beta$ -strands (hydrogen bonds, green dashed lines; water molecules, yellow spheres). b, View roughly perpendicular to a fibril of three layers, with the atoms of the side chains of the top layer shown as purple spheres. On top is a designed non-natural peptide inhibitor, Trp-His-Lys-chAla-Trp-hydroxyTic (blue; see Supplementary Fig. 16). c, The inhibitor blocks  $^{248}\text{PAP}^{286}$  fibril formation, as shown by monitoring Thioflavin T fluorescence. With a twofold molar excess of the inhibitor (pale red), the fluorescence remains low over the course of the experiment for all five replicates, unlike in the absence of inhibitor (grey). Mean fluorescence values are shown as solid red and black lines with and without the inhibitor, respectively. r.f.u., relative fluorescence units. d, HIV infection rates were determined by monitoring  $\beta$ -galactosidase ( $\beta$ -gal) activity. Agitated  $^{248}\text{PAP}^{286}$  alone efficiently increases viral infection, whereas  $^{248}\text{PAP}^{286}$  mixtures incubated with inhibitor were unable to enhance HIV infection. Peptide concentrations during virion treatment are indicated on the x axis. Error bars show the s.d. of three measurements per sample. r.l.u., relative light units.

Moreover, we propose that the bulky side chains and steric constraints of hydroxyTic provide hindrance to further fibril growth.

This designed peptide, WW61, effectively delays both seeded and unseeded fibril formation of  $^{248}\text{PAP}^{286}$  *in vitro* (Fig. 4c and Supplementary Figs 17 and 18). In the presence of a twofold molar excess of this inhibitor, seeded fibril formation is efficiently blocked for more than two days (Fig. 4c). Furthermore, we see that increasing the concentration of this inhibitor extends the fibril formation lag time (Supplementary Fig. 19). These inhibition assay results were further confirmed by electron microscopy (Supplementary Fig. 20). As a control for specificity, we tested the effect of GIHKQK, from the amino terminus of  $^{248}\text{PAP}^{286}$ , and PYKLWN, a peptide with the same charge as WW61. Neither peptide affected fibril formation kinetics, indicating that the inhibitory activity of the designed peptide is sequence specific (Supplementary Fig. 21).

Because  $^{248}\text{PAP}^{286}$  fibrils (SEVI) have been shown to enhance HIV infection<sup>23</sup>, using a functional assay we investigated whether WW61 is able to prevent this enhancement. In this experiment, we treated HIV particles with  $^{248}\text{PAP}^{286}$  solutions that had been agitated for 20 hours (to allow fibril formation) in the presence or absence of WW61, and infected TZM-bl indicator cells. As has been previously observed, SEVI efficiently enhanced HIV infection<sup>22</sup>. However,  $^{248}\text{PAP}^{286}$  incubated with the designed inhibitor prevented HIV infection (Fig. 4d).

We performed several control experiments to verify that the lack of infectivity observed in the assay is indeed due to the inhibition of SEVI formation. First we confirmed that in the absence of SEVI the designed inhibitor WW61 does not affect HIV infectivity (Supplementary Fig. 22a). We also found that the control peptides GIHKQK and PYKLWN, which do not inhibit  $^{248}\text{PAP}^{286}$  fibril formation, fail to decrease HIV infectivity (Supplementary Fig. 22b). Additionally, we observed that WW61 has no inhibitory effect on polylysine-mediated HIV infectivity<sup>27</sup>, further ruling out a non-specific electrostatic interaction mechanism (Supplementary Fig. 22a). Together, these results demonstrate that a peptide capable of preventing  $^{248}\text{PAP}^{286}$  fibril formation also inhibits the generation of virus-enhancing material.

Structure-based design of inhibitors of amyloid fibril formation has been challenging in the absence of detailed information about the atomic-level interactions that form the fibril spine. So far, one of the most successful structure-based approaches to preventing fibril formation has been to stabilize the native tetrameric structure of transthyretin<sup>28</sup>. That approach is well suited to the prevention of fibril formation of proteins with known native structures, but other proteins involved in amyloid-related diseases, such as tau protein, amyloid- $\beta$  and  $^{248}\text{PAP}^{286}$ , lack fully ordered native structures<sup>29</sup>. Our structure-based approach makes it possible to design inhibitors independent of native structure. Instead, the templates are atomic-level structures of short, fibril-forming segments<sup>14,15</sup>. By using these fibril-like templates, and adopting computational methods successful in designing novel proteins and protein-protein interfaces<sup>25,30</sup>, we have created specific inhibitors of proteins that normally form fibrils. These results support the hypothesis that the steric zipper is a principal feature of tau-related and SEVI fibrils, and suggest that, with current computational methods and steric-zipper structures, we have the tools to design specific inhibitors to prevent the formation of other amyloid fibrils.

## METHODS SUMMARY

We used crystal structures of hexapeptide segments of VQIVYK and GGVLVN as templates to design peptide inhibitors using the Rosetta software<sup>25</sup>. Briefly, this algorithm searches possible side-chain conformations (called rotamers) of all amino acids in a peptide  $\beta$ -strand backbone stacked onto the fibril end of both segment structures. The Rosetta software is extended to sample the approximate side-chain conformation of non-natural D and L amino acids by adapting side-chain torsion angles from those in their natural counterparts. The lowest energy set of side-chain rotamers is identified by combinatorial optimization of a potential consisting of a term for the Lennard-Jones potential, an orientation-dependent hydrogen-bond potential term, an implicit solvation term and a structure-derived side-chain and backbone torsional potential term.

Full Methods and any associated references are available in the online version of the paper at [www.nature.com/nature](http://www.nature.com/nature).

Received 6 December 2010; accepted 21 April 2011.

Published online 15 June 2011.

1. Westermark, P. *et al.* A primer of amyloid nomenclature. *Amyloid* **14**, 179–183 (2007).
2. Maji, S. K. *et al.* Functional amyloids as natural storage of peptide hormones in pituitary secretory granules. *Science* **325**, 328–332 (2009).
3. Fowler, D. M., Koulou, A. V., Balch, W. E. & Kelly, J. W. Functional amyloid – from bacteria to humans. *Trends Biochem. Sci.* **32**, 217–224 (2007).
4. Astbury, W. T. & Dickinson, S. The X-ray interpretation of denaturation and the structure of the seed globulins. *Biochem. J.* **29**, 2351–2360 (1935).
5. Calamai, M., Chiti, F. & Dobson, C. M. Amyloid fibril formation can proceed from different conformations of a partially unfolded protein. *Biophys. J.* **89**, 4201–4210 (2005).
6. Tjernberg, L. O. *et al.* Arrest of  $\beta$ -amyloid fibril formation by a pentapeptide ligand. *J. Biol. Chem.* **271**, 8545–8548 (1996).
7. Findels, M. A. Peptide inhibitors of  $\beta$  amyloid aggregation. *Curr. Top. Med. Chem.* **2**, 417–423 (2002).
8. Sciarretta, K. L., Gordon, D. J. & Meredith, S. C. Peptide-based inhibitors of amyloid assembly. *Methods Enzymol.* **413**, 273–312 (2006).
9. Soto, C., Kindy, M. S., Baumann, M. & Frangione, B. Inhibition of Alzheimer's amyloidosis by peptides that prevent  $\beta$ -sheet conformation. *Biochem. Biophys. Res. Commun.* **226**, 672–680 (1996).
10. Kokkoni, N., Stott, K., Amjee, H., Mason, J. M. & Doig, A. J. N-methylated peptide inhibitors of amyloid aggregation and toxicity. Optimization of the inhibitor structure. *Biochemistry* **45**, 9906–9918 (2006).
11. Sato, T. *et al.* Inhibitors of amyloid toxicity based on  $\beta$ -sheet packing of A $\beta$ 40 and A $\beta$ 42. *Biochemistry* **45**, 5503–5516 (2006).
12. Larbig, G., Pickhardt, M., Lloyd, D. G., Schmidt, B. & Mandelkow, E. Screening for inhibitors of tau protein aggregation into Alzheimer paired helical filaments: a ligand based approach results in successful scaffold hopping. *Curr. Alzheimer Res.* **4**, 315–323 (2007).
13. Wiesehan, K. *et al.* Selection of D-amino-acid peptides that bind to Alzheimer's disease amyloid peptide  $\text{a}\beta_{1-42}$  by mirror image phage display. *ChemBioChem* **4**, 748–753 (2003).
14. Nelson, R. *et al.* Structure of the cross- $\beta$  spine of amyloid-like fibrils. *Nature* **435**, 773–778 (2005).
15. Sawaya, M. R. *et al.* Atomic structures of amyloid cross- $\beta$  spines reveal varied steric zippers. *Nature* **447**, 453–457 (2007).
16. Wiltzius, J. *et al.* Molecular mechanisms for protein-encoded inheritance. *Nature Struct. Mol. Biol.* **16**, 973–978 (2009).
17. Selkoe, D. J. Alzheimer's disease: genes, proteins, and therapy. *Physiol. Rev.* **81**, 741–766 (2001).
18. Goux, W. J. *et al.* The formation of straight and twisted filaments from short tau peptides. *J. Biol. Chem.* **279**, 26868–26875 (2004).
19. von Bergen, M. *et al.* Assembly of  $\tau$  protein into Alzheimer paired helical filaments depends on a local sequence motif (<sup>306</sup>VQIVYK<sup>311</sup>) forming  $\beta$  structure. *Proc. Natl Acad. Sci. USA* **97**, 5129–5134 (2000).
20. Goldschmidt, L., Teng, P. K., Riek, R. & Eisenberg, D. Identifying the amyloids, proteins capable of forming amyloid-like fibrils. *Proc. Natl Acad. Sci. USA* **107**, 3487–3492 (2010).
21. Thompson, M. J. *et al.* The 3D profile method for identifying fibril-forming segments of proteins. *Proc. Natl Acad. Sci. USA* **103**, 4074–4078 (2006).
22. Münch, J. *et al.* Semen-derived amyloid fibrils drastically enhance HIV infection. *Cell* **131**, 1059–1071 (2007).
23. Friedhoff, P., von Bergen, M., Mandelkow, E. M., Davies, P. & Mandelkow, E. A nucleated assembly mechanism of Alzheimer paired helical filaments. *Proc. Natl Acad. Sci. USA* **95**, 15712–15717 (1998).
24. Wille, H., Drewes, G., Biernat, J., Mandelkow, E. M. & Mandelkow, E. Alzheimer-like paired helical filaments and antiparallel dimers formed from microtubule-associated protein tau *in vitro*. *J. Cell Biol.* **118**, 573–584 (1992).
25. Kuhlman, B. *et al.* Design of a novel globular protein fold with atomic-level accuracy. *Science* **302**, 1364–1368 (2003).
26. Chen, Z., Krause, G. & Reif, B. Structure and orientation of peptide inhibitors bound to  $\beta$ -amyloid fibrils. *J. Mol. Biol.* **354**, 760–776 (2005).
27. Roan, N. R. *et al.* The cationic properties of SEVI underlie its ability to enhance human immunodeficiency virus infection. *J. Virol.* **83**, 73–80 (2009).
28. Petrassi, H. M., Klabunde, T., Sacchetti, J. & Kelly, J. W. Structure-based design of N-phenyl phenoxazine transthyretin amyloid fibril inhibitors. *J. Am. Chem. Soc.* **122**, 2178–2192 (2000).
29. Schweers, O., Schonbrunn-Hanebeck, E., Marx, A. & Mandelkow, E. Structural studies of tau protein and Alzheimer paired helical filaments show no evidence for  $\beta$ -structure. *J. Biol. Chem.* **269**, 24290–24297 (1994).
30. Fleishman, S. J. *et al.* Computational design of proteins targeting the conserved stem region of influenza hemagglutinin. *Science* **332**, 816–821 (2011).

Supplementary Information is linked to the online version of the paper at [www.nature.com/nature](http://www.nature.com/nature).

**Acknowledgements** We thank M. I. Ivanova, J. Corn, T. Kortemme, D. Anderson, M. R. Sawaya, M. Phillips, S. Sambashivan, J. Park, M. Landau, A. Laganowsky, Q. Zhang, R. Clubb, F. Guo, T. Yeates, J. Nowick, J. Zheng and M. J. Thompson for discussions; the HHMI, NIH, NSF, Gates Foundation and Joint Center for Translational Medicine for support; R. Peterson for help with NMR experiments; E. Mandelkow for providing tau constructs; R. Riek for providing amyloid- $\beta$ ; and J. Stroud for amyloid- $\beta$  preparation.

RESEARCH LETTER

Support came from the Damon Runyon Cancer Research Foundation (J.K.), the Ruth L. Kirschstein National Research Service Award (H.W.C.), the programme for junior professors by the Ministry of Science, Baden-Württemberg (J.M.), and a UCLA-IGERT bioinformatics traineeship (S.A.S.).

**Author Contributions** S.A.S., J.K., D.B., J.M. and D.E. designed the project. J.K. and S.A.S. created the design protocol. J.K. designed the D-peptides. L.J. expanded the design methodology and designed the non-natural amino-acid peptides. S.A.S., H.W.C. and A.Z. performed the fluorescence experiments and electron microscopy, and analysed kinetic data. A.Z. determined the structure of GGVLN. O.Z. performed the HIV

infectivity experiments. J.T.S. determined the tau fibril elongation rates. S.A.S. performed the NMR experiments. S.A.S., J.K. and D.E. wrote the manuscript and coordinated contributions by other authors.

**Author Information** Atomic coordinates and structure factors for the reported GGVLN structure have been deposited in the Protein Data Bank with accession code 3PPD. Reprints and permissions information is available at [www.nature.com/reprints](http://www.nature.com/reprints). The authors declare no competing financial interests. Readers are welcome to comment on the online version of this article at [www.nature.com/nature](http://www.nature.com/nature). Correspondence and requests for materials should be addressed to D.E. ([david@mbi.ucla.edu](mailto:david@mbi.ucla.edu)).

## METHODS

**Computational design.** Computational designs were carried out using the Rosetta software<sup>25</sup> (<http://www.rosettacommons.org>). This algorithm involves building side-chain rotamers of all amino acids onto a fixed protein backbone. The lowest energy set of side-chain rotamers is then identified as those which minimize an energy function containing a Lennard-Jones potential, an orientation-dependent hydrogen-bond potential, a solvation term, amino-acid-dependent reference energies and a statistical torsional potential that depends on the backbone and side-chain dihedral angles.

**D-amino-acid tau inhibitors.** The crystal structure of VQIVYK (ref. 15; Protein Data Bank ID, 2ON9) was used as a starting scaffold for computational design. To take full advantage of the statistical nature of the rotamer library and some terms in the Rosetta energy function, the stereochemistry of the fibril scaffold was inverted so that design would take place using L-amino acids. An extended L-peptide was aligned with the N, C and O backbone atoms of the D-fibril scaffold. This L-peptide was subsequently redesigned, keeping all atoms of the D-fibril fixed. The stereochemistry of the final design model was then inverted, yielding a D-peptide designed to cap an L-fibril. We inspected the finished models to confirm that inversion of the stereochemistry at the Thr and Ile C $\beta$  atoms did not make the designs energetically unfavourable. Energetic consequences of incorporating a D inhibitor peptide in the middle of an L fibril were subsequently evaluated to ensure that fibril propagation could not continue after association of an inhibitor. Calculations of the area buried and shape complementarity were performed with AREAIMOL<sup>31</sup> and SC<sup>32</sup>, respectively.

**L-peptide <sup>246</sup>PAP<sup>286</sup> inhibitors.** The crystal structure of GGVLVN (PDB ID, 3PPD) was used as a template for the following design procedure. An extended L-peptide was aligned according to crystal symmetry. Small, random perturbations of the L-peptide were performed to optimize the rigid-body arrangement between the fibril template and the peptide inhibitor. Full sequence optimization of the inhibitor was performed using the Rosetta software package, allowing residues directly contacting the inhibitor to repack; other scaffold residues remained fixed. Because the design calculations use a discrete rotamer representation of the side chains, we next performed simultaneous quasi-Newtonian optimization of the inhibitor rigid-body orientation, the side-chain torsion angles and, in some cases, the backbone torsion angles using the full-atom Rosetta energy function. This optimization was essential to the subsequent assessment of the inhibition of the design. Several iterative runs of small perturbations in inhibitor placement, interface design and refinement were performed to improve hydrogen-bonding and packing interactions. The designs that ranked highest on the basis of the total binding energy between the inhibitor and the fibril scaffold and the interfacial shape complementarity<sup>33</sup> were subsequently synthesized and tested.

For each initial active L-peptide design, the non-natural L-amino acids were incorporated using a growth strategy. Non-natural amino acids, structurally similar to those of initial active designs, were selected on the basis of their solubility, side-chain shape and commercial availability. Side-chain conformations were approximately sampled by adopting side-chain torsion angles from those in their natural counterparts. Sequence optimization of the inhibitor was performed and the optimal set of rotamers identified using Monte Carlo simulated annealing with the full-atom energy function described above. The resulting designs were ranked on the basis of the total binding energy between the inhibitor and the fibril scaffold. **Tau construct expression and purification.** pNG2 expression vectors (derived from pET-3b<sup>33</sup>) containing either the K12 or K19 gene were provided by E. Mandelkow<sup>34</sup>. Expression in BL21(DE3) *Escherichia coli*<sup>35</sup> was induced with 1 mM isopropyl thiogalactoside when the absorbance  $A_{600\text{ nm}}$  was between 0.8 and 1.0, and cells were collected after 3–4 h. K12 and K19 were purified on the basis of previously described methods<sup>32</sup>. Cells were pelleted for 20 min at 4,700g and resuspended in 20 mM MES, pH 6.8, 1 mM EDTA, 0.2 mM MgCl<sub>2</sub>, 5 mM DTT, 1 mM PMSF and a protease inhibitor cocktail. The cells were sonicated for 2.5 min and, following addition of NaCl to bring cell lysate to 0.5 M NaCl, the lysate was boiled for 20 min. The lysate was sedimented at 30,000g for 20 min and dialyzed twice against 20 mM MES, pH 6.8, 50 mM NaCl, 1 mM EDTA, 1 mM MgCl<sub>2</sub>, 2 mM DTT and 0.1 mM PMSF at 4 °C. The dialysate was pelleted for 20 min at 30,000g and filtered before cation exchange chromatography on an AKTA Explorer (GE Pharmacia) with a HighTrap HP SP 5-ml column (GE Healthcare). The sample was eluted with a linear gradient of up to 60% buffer B (20 mM MES, pH 6.8, 1 M NaCl, 1 mM EDTA, 1 mM MgCl<sub>2</sub>, 2 mM DTT and 0.1 mM PMSF). Size exclusion chromatography was optionally performed with a Superdex 75 10/300 GL column (GE Healthcare) in PBS buffer (137 mM NaCl, 3 mM KCl, 10 mM Na<sub>2</sub>HPO<sub>4</sub>, 2 mM KH<sub>2</sub>PO<sub>4</sub>, pH 7.4) with 1 mM DTT on the AKTA Explorer depending on preparation purity as assessed by SDS polyacrylamide gel electrophoresis.

**Tau construct inhibition assays.** Fibril formation assays were performed on the basis of previously published protocols<sup>35, 36</sup>. Reaction mixtures (150  $\mu$ l) containing

50  $\mu$ M tau K12 or K19, as determined by the Micro BCA Protein Assay Kit (Pierce), were incubated in 250 mM sodium phosphate buffer, pH 7.4, with 1 mM DTT, 12.5  $\mu$ M heparin (average molecular mass, 6,000 Da; Sigma) and 10  $\mu$ M Thioflavin S (ThS; MP Bio). Inhibitor peptides (CS Bio, Celtek Biosciences) were dissolved in 250 mM phosphate buffer, pH 7.4, to 0.5 mM and added at specified molar ratios. Reactions were split into a minimum of three replicates in black, 96-well, optically clear plates (Nunc), sealed with Corning pressure-sensitive sealing tape and monitored using either a Varioskan plate reader (Thermo Scientific), for K12, or a SpectraMax M5, for K19. The fluorescence signal was measured every 15 min with excitation and emission wavelengths of 440 and 510 nm, respectively, at 37 °C, with continuous shaking at 900 r.p.m. with a diameter of 1 mm for K12, and with quiescent incubation with shaking 2 s before each reading for K19. Plots showing the fluorescence trace of the replicate with median lag time for each sample were created using R<sup>38</sup>. Plots of lag time depict the mean time value at which each replicate crossed an arbitrary fluorescence value above noise background (values were selected per experiment and applied to all samples). Error bars represent the standard deviation of the replicate lag times for each sample.

**Seeded K12 fibril formation assays.** Seeds were produced by incubating 50  $\mu$ M K12 as above, but without ThS present, and were added at 0.25% (v/v). Peptide stock concentrations were 0.75 mM and were added at a final concentration of tenfold molar excess relative to soluble K12. Reaction mixtures were otherwise prepared and monitored as above.

**VQIVYK inhibition assays.** The VQIVYK fibril formation assay was modified from a previously published protocol<sup>36</sup>. Buffers and plates were kept on ice to delay VQIVYK fibril formation while the reaction mixtures were prepared. Replicate solutions of 180  $\mu$ l of 25 mM MOPS, pH 7.2, 100  $\mu$ M ThS and inhibitor peptides were added to black, clear-bottomed, 96-well Nunc plates with 1/8-inch PTFE beads (Orange Products). Acetylated and amidated VQIVYK (Genscript) was dissolved in H<sub>2</sub>O to 1.3 mM and filtered through a Millipore Microcon 100-kDa filter device at 14,000g for 5 min at 4 °C to remove large aggregates (final concentration, ~1 mM). Filtered VQIVYK (20  $\mu$ l) was added to each reaction well. ThS fluorescence was monitored at room temperature every 2 min using a SpectraMax M5 fluorometer with 2 s of mixing before each reading.

**Amyloid- $\beta$  fibril formation assay.** Lyophilized amyloid- $\beta$ (1–42) was diluted to 0.2 mg ml<sup>-1</sup> in 50 mM NH<sub>4</sub>OH and filtered with a 0.2- $\mu$ m filter. The reaction mixture contained a final concentration of 11.5  $\mu$ M amyloid- $\beta$ (1–42), 10  $\mu$ M Thioflavin T (ThT), 23 mM NH<sub>4</sub>OH in 100 mM bicine, pH 9.1, and 11.5  $\mu$ M D-TLKIVW in reactions with peptide present. Reactions were split into four replicates and the ThT fluorescence signal was measured every minute (excitation wavelength, 440 nm; emission wavelength, 510 nm), at 37 °C, with continuous shaking at 960 r.p.m. with a 1-mm diameter in a Varioskan fluorometer.

**Electron microscopy.** Sample (5  $\mu$ l) was applied to glow-discharged, 400-mesh carbon-coated, formvar films on copper grids (Ted Pella) for 3 min. Grids were rinsed twice with distilled water and stained with 1% uranyl acetate for 90 s. Grids were examined in a Hitachi H-7000 transmission electron microscope at 75 keV or a JEOL JEM1200-EX operating at 80 keV.

**Tau fibril formation kinetic analysis.** The nucleation ( $k_1$ ) and propagation ( $k_2$ ) rates were determined by fitting the form of the Fink–Watzky two-step mechanism<sup>41</sup>. Plateau values were determined and the remaining parameters were fitted using the 'leasqr' nonlinear least-squares regression function (<http://fly.istc.cnr.it/pub/software/octave/leasqr/>) through the OCTAVE software package (<http://www.gnu.org/software/octave/>).

**Preparation of peptide-gold conjugates.** Peptide-Nanogold conjugates were prepared as described earlier for similarly sized peptides<sup>42</sup>. Briefly, 60 nmol of the peptides CGGG-(D)-TLKIVW and CGGG-(D)-LKTWIV (CS Bio) were dissolved in 110  $\mu$ l of phosphate-buffered saline (20 mM, pH 6.5, 0.15 M NaCl), added to 6 nmol of Monomaleimido Nanogold (Nanoprobes), dissolved in 200  $\mu$ l H<sub>2</sub>O and incubated for 1 h at room temperature (22 °C) with constant rotation. Peptide-Nanogold conjugates were separated from excess unbound peptides by membrane centrifugation (Microcon-10 system, Amicon) using a molecular mass cut-off of 10 kDa. Peptide-Nanogold conjugates were then diluted into phosphate-buffered saline, aliquoted and stored at -20 °C for no longer than one month.

**Preparation of K19 fibrils.** K19 fibrils were generated by incubating 100  $\mu$ M soluble K19 with 25  $\mu$ M 6-kDa heparin overnight at 37 °C in phosphate buffer (50 mM, pH 7.4). K19 fibrils were sonicated for 15 s, using a microtip set to 35% amplitude. Residual heparin and small oligomers were removed by centrifuging the mixture through a 100-kDa Microcon concentrator for 10 min at 14,000g, washing the retentate with phosphate buffer and repeating three times; the retentate was restored to its original volume with phosphate buffer. These short fibril segments were stored at 4 °C for no longer than one week. For NMR studies, fibril samples were similarly prepared, but were washed in H<sub>2</sub>O and concentrated to 2 mM K19 (by monomer).

**Preparation of samples for Nanogold binding experiments.** Nanogold conjugated inhibitor (or control) (10 nM) was incubated with 1.67  $\mu\text{M}$  K19 fibrils (by monomer) in MOPS buffer (25 mM, pH 7.2) for 1 h. We applied 5  $\mu\text{l}$  of it to a glow-discharged, 400-mesh carbon-stabilized copper grid (Ted Pella) for 3 min. The grids were washed twice with  $\text{H}_2\text{O}$  and 10  $\mu\text{l}$  of the Goldenhance reagent was applied for 10 s. The grids were washed five times with  $\text{H}_2\text{O}$  and negatively stained with 2% uranyl acetate.

**Quantification and localization of Nanogold binding.** For each sample, 75 Nanogold particles  $\approx 15$  nm in diameter were counted and classified as bound or unbound. The 15-nm cut-off was chosen to exclude unbound, but adjacent, particles enlarged by Goldenhance that only apparently bind fibrils. To establish the localization of the binding observed, individual Nanogold particles bound to fibrils were categorized as bound to the fibril end or side. In both of these experiments, sample identities were concealed from the microscopist to ensure unbiased counting. Grids were examined with a JEOL JEM1200-EX and images were recorded using DIGITALMICROGRAPH (Gatan).

**Statistical analysis of Nanogold binding.** We compared counts of Nanogold-conjugated peptides and unconjugated Nanogold bound to fibrils or localizing to fibril ends. Twenty-one unconjugated Nanogold particles out of 75 counted bound to fibrils. We modelled Nanogold particles bound to fibrils using a binomial distribution with parameters  $n = 75$  (sample size: number of observations) and  $P = 0.28$  (probability of success). In a separate experiment, 22 unconjugated Nanogold particles bound to fibrils that localized to fibril ends, following a binomial distribution with  $n = 105$  and  $P = 0.21$ .

Because the number of counts is fairly large, we assumed a normal distribution and used a standard Z-test to compare the number of bound Nanogold-peptide conjugates with the expected distribution based on the number of bound, unconjugated Nanogold particles. We used an analogous analysis to determine the significance of localization to fibril ends.

The numbers of Nanogold-D-TLKIVW conjugates bound to fibrils ( $x_{\text{bound}} = 43$ ,  $n = 75$ ) and bound Nanogold-D-TLKIVW conjugates localizing to the end of fibrils ( $x_{\text{end}} = 49$ ,  $n = 86$ ) were significantly different from the corresponding numbers for Nanogold alone, whereas the number of Nanogold-D-LKTIVW conjugates bound ( $x_{\text{bound}} = 15$ ,  $n = 75$ ) or the number localized to fibril ends ( $x_{\text{end}} = 17$ ,  $n = 100$ ) did not differ significantly from the corresponding numbers for Nanogold alone.

**VQIVYK preparation for binding studies.** Acetylated and amidated VQIVYK peptide (Genscript) was dissolved to 1 mM in 25 mM MOPS, pH 7.2, and incubated at room temperature for at least 24 h. Fibrils were washed with  $\text{H}_2\text{O}$ , concentrated using an Amicon ultracentrifugal filter with a 3-kDa molecular mass cut-off and resuspended in  $\text{H}_2\text{O}$  to a final concentration (by monomer) of 4 mM. Soluble VQIVYK was prepared by dissolving VQIVYK peptide (CS Bio) with free amino and carboxy termini in  $\text{H}_2\text{O}$ .

**$^1\text{H}$  NMR sample preparation and measurements.** NMR samples were prepared with 5%  $\text{D}_2\text{O}$  and 10 mM NaOAc, pH 5.0. D-peptides were added from 1 mM stocks in  $\text{H}_2\text{O}$  to a final concentration of 100  $\mu\text{M}$ . Soluble and fibrillar VQIVYK and tau protein were added at indicated concentrations to make a final volume of 550  $\mu\text{l}$ .  $^1\text{H}$  NMR spectra measured at 500 MHz were collected on a Bruker DRX500 at 283 K.  $\text{H}_2\text{O}$  resonance was suppressed through presaturation. Spectra were processed with XWINNMR 3.6.

**Binding constant estimations.** NMR data were analysed to estimate a binding constant for the interaction between D-TLKIVW and VQIVYK fibrils. At about 1,000  $\mu\text{M}$  VQIVYK (concentration as monomer), 50% of D-TLKIVW is bound (Supplementary Fig. 11). The steric-zipper model suggests that there are two monomers per 4.7 Å (0.47-nm) layer in a fibril<sup>14</sup>—such that the number of monomers per fibril is given by [fibril length (nm)]  $\times$  (2 monomers per 0.47 nm)—and we estimate the fibril concentration using the monomer concentration:  $[\text{VQIVYK}]_{\text{fibril}} = [\text{VQIVYK}]_{\text{monomer}} / (\text{monomers per fibril})$ . If we assume one binding site and estimate from electron microscopy an average length of  $\approx 140$  nm per fibril, then there are about 600 monomers per fibril, and the apparent dissociation constant is about 2  $\mu\text{M}$ .

**Hydrogen-bonding energy calculation.** We used AREAIMOL<sup>11</sup> to calculate the non-polar and polar areas buried by the interaction between D-TLKIVW with the VQIVYK steric zipper (Fig. 2b, c and Supplementary Fig. 1). We calculate buried areas of 201, 24 and 102 Å<sup>2</sup> for carbon, nitrogen and oxygen atoms, respectively. Using the atomic solvation parameters of ref. 43, we estimate that the free energy of transferring the inhibitor from a non-polar phase to an aqueous phase,  $\Delta G_{\text{solvation}}$  is approximately 2.5 kcal mol<sup>-1</sup>. On the basis of an apparent dissociation constant of 2  $\mu\text{M}$ , we estimate the total free energy change of bringing the inhibitor into contact with the VQIVYK steric-zipper template,  $\Delta G_{\text{binding}}$ , to be 7.4 kcal mol<sup>-1</sup>. From the interaction model (Fig. 2c and Supplementary Fig. 1), we maintain six hydrogen bonds between D-TLKIVW and VQIVYK, and estimate the free energy change per hydrogen bond to be  $(\Delta G_{\text{binding}} - \Delta G_{\text{solvation}}) / 6$ , or  $\approx 0.8$  kcal mol<sup>-1</sup>.

**GGVLN crystallization and structure determination.** The GGVLN peptide was dissolved in 10 mM Tris, pH 9, at 1.8 mg ml<sup>-1</sup> and crystallized in 10% (w/v) PEG-8000, 0.1 M MES, pH 6.0, and 0.2 M Zn(OAc)<sub>2</sub>. X-ray diffraction data was collected at APS beamline 24-ID-E. Phases were determined by molecular replacement using an idealized  $\beta$ -strand in PHASER<sup>44</sup>. Crystallographic refinement was performed using REFMAC<sup>45</sup>. Model building was performed with COOT<sup>46</sup> and illustrated with PYMOL<sup>47</sup>.

**$^{248}\text{PAP}^{286}$  fibril formation and inhibition.** Fmoc- $\beta$ -cyclohexyl-L-alanine and Fmoc-7-hydroxy-(S)-1,2,3,4-tetrahydroisoquinoline-3-carboxylic acid were purchased from AnaSpec and the inhibitor peptide Trp-His-Lys-chAla-Trp-hydroxyTic (WW61) was synthesized by Celtek Biosciences.  $^{248}\text{PAP}^{286}$  and WW61 were dissolved as  $\times 1.25$  and  $\times 5$  stocks in PBS, respectively, and filtered with a 0.1- $\mu\text{m}$  filter.  $^{248}\text{PAP}^{286}$  was diluted with PBS to 0.66 mM and ThT was added to 10  $\mu\text{M}$  final concentration. Samples were optionally mixed with 1.32 mM WW61 and vortexed. Five replicates of 150  $\mu\text{l}$  were immediately dispensed into a 96-well plate. In dose-response experiments, WW61 final concentrations were 0.33, 0.66 and 1.32 mM. Plates were continuously agitated at 960 r.p.m. at 37 °C, and ThT fluorescence readings were recorded (excitation wavelength, 440 nm; emission wavelength, 482 nm) at 15-min intervals with a Varioskan Flash fluorometer. Lag time was determined when fluorescence crossed an arbitrary value (3 r.f.u.) above background.

**Effect of WW61 on fibril-mediated enhancement of HIV-1 infection.** The CCR5 tropic molecular HIV-1 clone NL4\_3/92TH014-2<sup>48</sup> was generated by transient transfection of 293T cells with proviral DNA. Supernatants were collected 48 h later and p24 concentrations determined by ELISA. TZM-bl reporter cells encoding a *lacZ* gene under the control of the viral LTR promoter were obtained through the NIH AIDS Research and Reference Reagent Program and provided by Dr John C. Kappes, Dr Xiaoyun Wu and Tranzyme<sup>49</sup>. HIV-1 (40  $\mu\text{l}$ ) containing 0.1 ng of p24 antigen was incubated with 40- $\mu\text{l}$  dilutions of mixtures of  $^{248}\text{PAP}^{286}$  and inhibitory peptide, WW61, that was either freshly prepared or had been agitated for 23 h. Peptide concentrations and experimental conditions during agitation were similar to those described above. Thereafter, 20  $\mu\text{l}$  of the mixtures were used to infect 180  $\mu\text{l}$  of TZM-bl cells seeded the day before ( $10^5$  per well). Two days later, infection rates were determined by quantifying  $\beta$ -galactosidase activities in cellular lysates using the Gal-Screen assay (Applied Biosystems, T1027). Luminescence was recorded on an Orion microplate luminometer as relative light units per second.

**Effect of WW61 on polylysine-mediated enhancement of HIV-1 infection.** Polylysine (Sigma Aldrich) (50  $\mu\text{l}$ ) was mixed with an equal volume of WW61. Thereafter, 35- $\mu\text{l}$  fivefold dilutions of the polylysine-WW61 mixture or polylysine alone were incubated with the same volume of virus and incubated for 5 min at room temperature. Polylysine-WW61 concentrations were 100, 20, 4, 0.8, 0.16, 0.032, 0.064 and 0  $\mu\text{g ml}^{-1}$  during pre-incubation with virus stocks. Thereafter, 20  $\mu\text{l}$  of each mixture was added to 180  $\mu\text{l}$  of TZM-bl cells. The infection rate was determined two days later as described above.

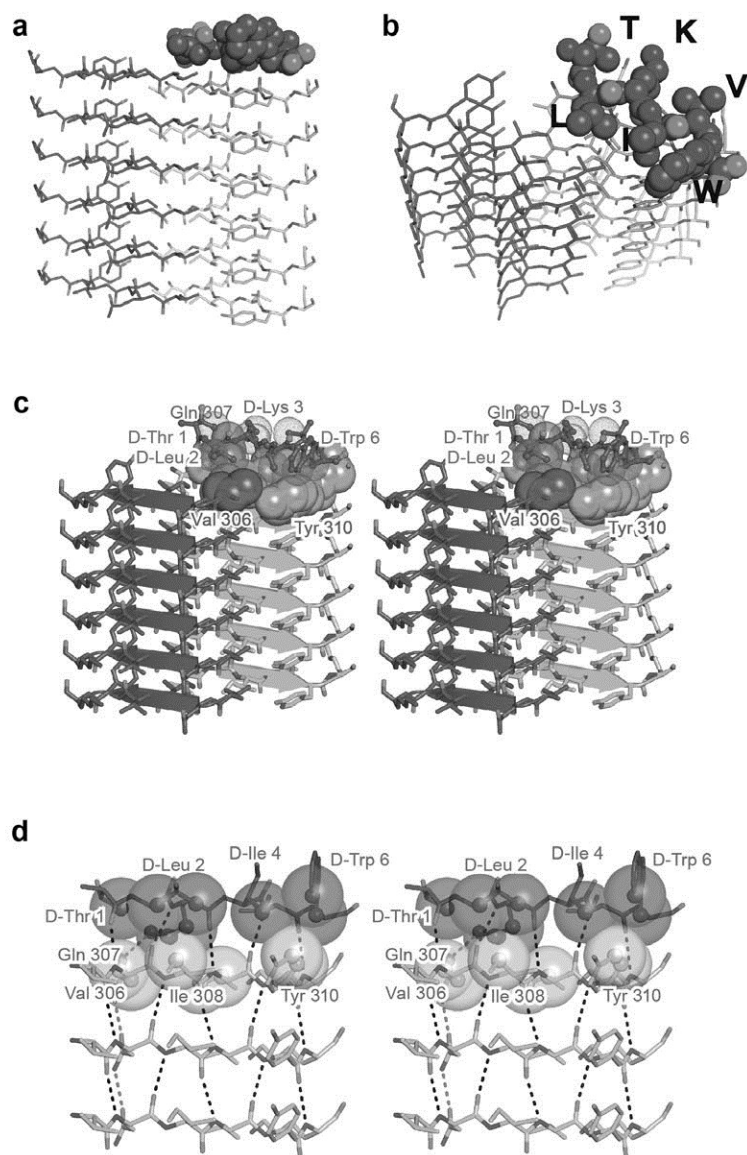
**Effect of WW61, GIHKQK and PYKLWN on HIV-1 infection.** Each peptide (40  $\mu\text{l}$ ) was incubated with an equal volume of virus containing 1 ng of p24 antigens for 5 min at room temperature. Peptide concentrations were 150, 30, 6, 1.2 and 0  $\mu\text{g ml}^{-1}$  during pre-incubation with virus stocks. Thereafter, 20  $\mu\text{l}$  of each mixture was added separately to 180  $\mu\text{l}$  of TZM-bl cells (tenfold dilution) and the infection rate was determined as above.

- Collaborative Computational Project, Number 4. The CCP4 suite: programs for protein crystallography. *Acta Crystallogr. D* **50**, 760–763 (1994).
- Lawrence, M. C. & Colman, P. M. Shape complementarity at protein/protein interfaces. *J. Mol. Biol.* **234**, 946–950 (1993).
- Studier, F. W., Rosenberg, A. H., Dunn, J. J. & Dubendorff, J. W. Use of T7 RNA polymerase to direct expression of cloned genes. *Methods Enzymol.* **185**, 60–89 (1990).
- Biernat, J. et al. The switch of tau protein to an Alzheimer-like state includes the phosphorylation of two serine-proline motifs upstream of the microtubule binding region. *EMBO J.* **11**, 1593–1597 (1992).
- Barghorn, S., Biernat, J. & Mandelkow, E. Purification of recombinant tau protein and preparation of Alzheimer-paired helical filaments in vitro. *Methods Mol. Biol.* **299**, 35–51 (2005).
- Friedhoff, P., Schneider, A., Mandelkow, E. M. & Mandelkow, E. Rapid assembly of Alzheimer-like paired helical filaments from microtubule-associated protein tau monitored by fluorescence in solution. *Biochemistry* **37**, 10223–10230 (1998).
- Pérez, M., Valpuesta, J. M., Medina, M., Montejó de Garcini, E. & Avila, J. Polymerization of tau into filaments in the presence of heparin: the minimal sequence required for tau-tau interaction. *J. Neurochem.* **67**, 1183–1190 (1996).
- Schweers, O., Mandelkow, E. M., Biernat, J. & Mandelkow, E. Oxidation of cysteine-322 in the repeat domain of microtubule-associated protein tau controls the in vitro assembly of paired helical filaments. *Proc. Natl. Acad. Sci. USA* **92**, 8463–8467 (1995).

39. R Development Core Team. *R: A Language and Environment for Statistical Computing* (R Foundation for Statistical Computing, Vienna) (<http://www.r-project.org>) (2008).
40. Rojas Quijano, F. A., Morrow, D., Wise, B. M., Brancia, F. L. & Goux, W. J. Prediction of nucleating sequences from amyloidogenic propensities of tau-related peptides. *Biochemistry* **45**, 4638–4652 (2006).
41. Morris, A. M., Watzky, M. A., Agar, J. N. & Finke, R. G. Fitting neurological protein aggregation kinetic data via a 2-step, minimal "Ockham's razor" model: the Finke-Watzky mechanism of nucleation followed by autocatalytic surface growth. *Biochemistry* **47**, 2413–2427 (2008).
42. Schmidt, K., Segond von Banchet, G. & Heppelmann, B. Labelling of peptides with 1.4 nm gold particles to demonstrate their binding sites in the rat spinal cord. *J. Neurosci. Methods* **87**, 195–200 (1999).
43. Eisenberg, D., Wesson, M. & Yamashita, M. Interpretation of protein folding and binding with atomic solvation parameters. *Chem. Scr.* **29A**, 217–221 (1989).
44. McCoy, A. J. *et al.* Phaser crystallographic software. *J. Appl. Crystallogr.* **40**, 658–674 (2007).
45. Murshudov, G. N., Vagin, A. A. & Dodson, E. J. Refinement of macromolecular structures by the maximum-likelihood method. *Acta Crystallogr. D* **53**, 240–255 (1997).
46. Emsley, P. & Cowtan, K. Coot: model-building tools for molecular graphics. *Acta Crystallogr. D* **60**, 2126–2132 (2004).
47. DeLano, W. L. *PyMOL Molecular Viewer* (<http://www.pymol.org>) (2002).
48. Papkalla, A., Munch, J., Otto, C. & Kirchhoff, F. Nef enhances human immunodeficiency virus type 1 infectivity and replication independently of viral coreceptor tropism. *J. Virol.* **76**, 8455–8459 (2002).
49. Platt, E. J., Wehrly, K., Kuhmann, S. E., Chesebro, B. & Kabat, D. Effects of CCR5 and CD4 cell surface concentrations on infections by macrophagetropic isolates of human immunodeficiency virus type 1. *J. Virol.* **72**, 2855–2864 (1998).

# SUPPLEMENTARY INFORMATION

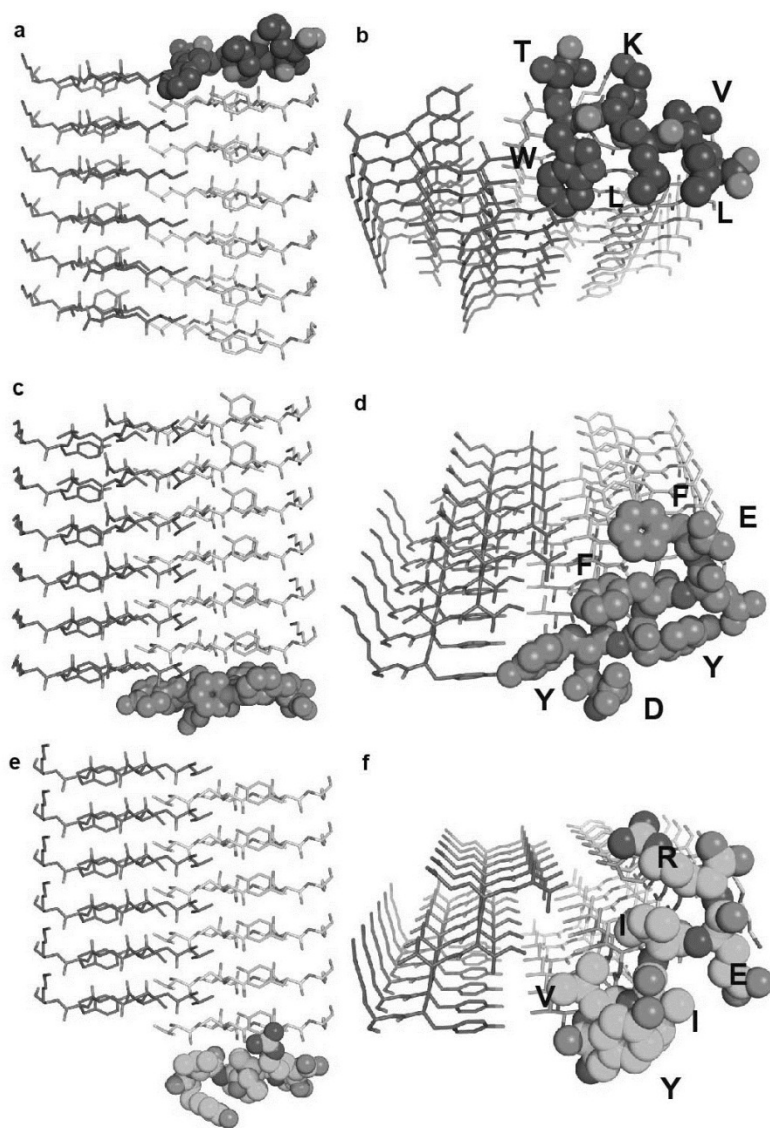
doi:10.1038/nature10154



**Supplementary Figure 1. d-TLKIVW design model.** The modeled interaction of D-TLKIVW with VQIVYK (pdb id: 2ON9) is shown. **a**, The side view and top-down view, **b**,

of the designed inhibitor, D-TLKIVW (red), interacting with the VQIVVK steric zipper structure in purple and grey. **c**, The wall-eyed stereo view of the modeled D-TLKIVW segment on the VQIVVK steric-zipper structure shows complementarity between D-TLKIVW (red ball-and-stick representation) and both  $\beta$ -strands of VQIVVK. The D-TLKIVW molecule (dot-sphere representation) fits well on the surface of the pair of  $\beta$ -sheets from VQIVVK molecules (shown as spheres). **d**, In this stereo view, the purple  $\beta$ -sheet of VQIVVK is removed to show the interactions between D-TLKIVW and the grey VQIVVK  $\beta$ -sheet. The side chains of D-Leu2, D-Ile4, and D-Trp6 of D-TLKIVW make favorable interactions with the grey sheet from the VQIVVK molecule. Transparent spheres show interacting atoms in the model. D-Leu2 and D-Ile4 also interact with the N-terminal Val306 and Ile308 of the mating VQIVVK molecule. D-Lys3 of D-TLKIVW replaces the side chain hydrogen bonding interaction of stacked Gln in the VQIVVK structure (red dashes). Black dashes show the main chain hydrogen bonds between layers of peptide.

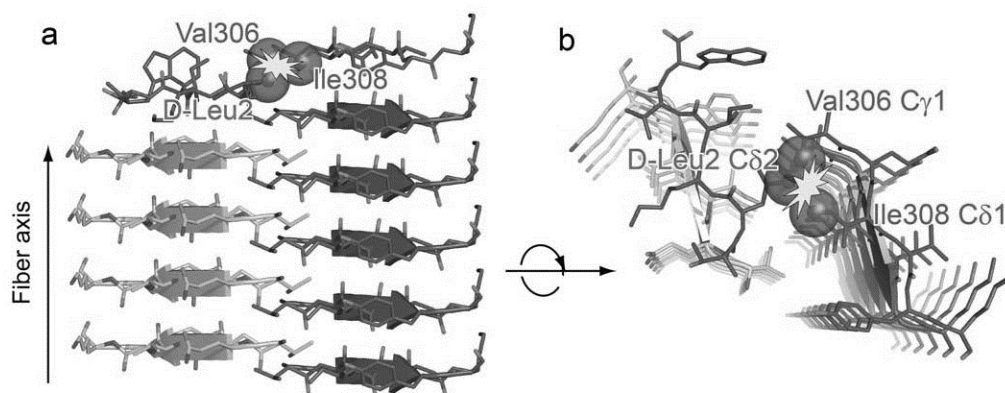




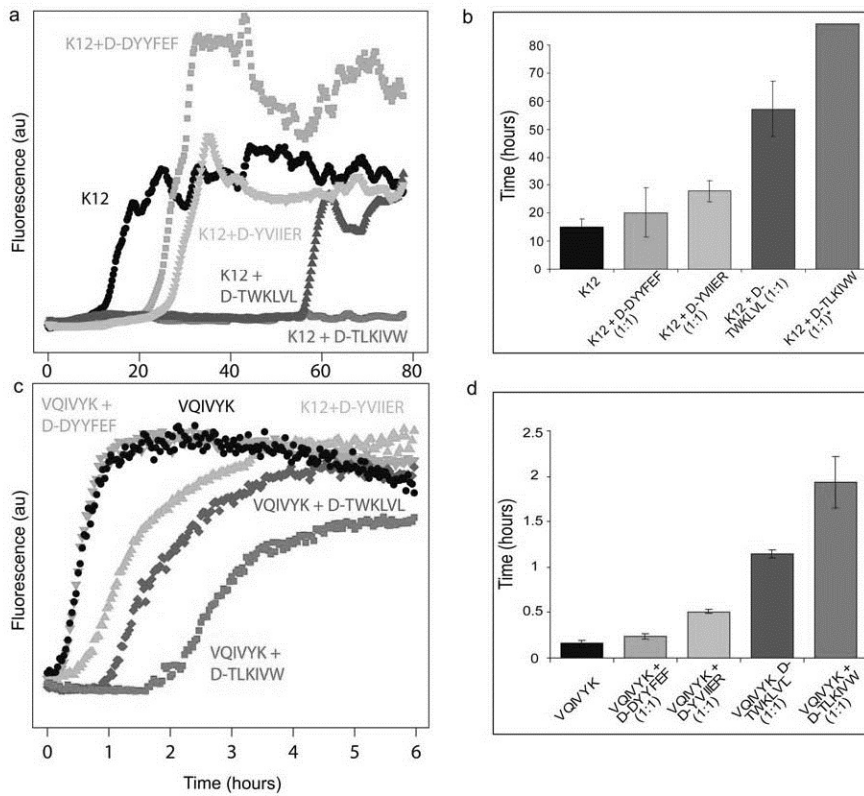
**Supplementary Figure 2. Other designed D-amino acid tau inhibitor models.**

Besides D-TLKIVW, three additional D-amino acid peptides were predicted. The side view a, and top-down view b, of D-TWKLVL (in blue) show how the D-TWKLVL model is

predicted to interact with VQIVYK (purple and grey  $\beta$ -sheets). The bulky D-Trp2 residue would prevent the addition of another VQIVYK molecule on top of the purple  $\beta$ -sheet. **c** and **d**, D-DYYFEF was designed to interact with both faces of the hydrophobic VQIVYK steric zipper bottom, with the inner facing tyrosine and phenylalanine residues interacting with the  $\beta$ -sheet across the steric zipper interface. **e** and **f**, The bottom inhibitor D-YVIIER was designed to interact with the bottom grey  $\beta$ -sheet of VQIVYK, testing the hypothesis that an arginine residue would pack favorably against Tyr311 of VQIVYK.

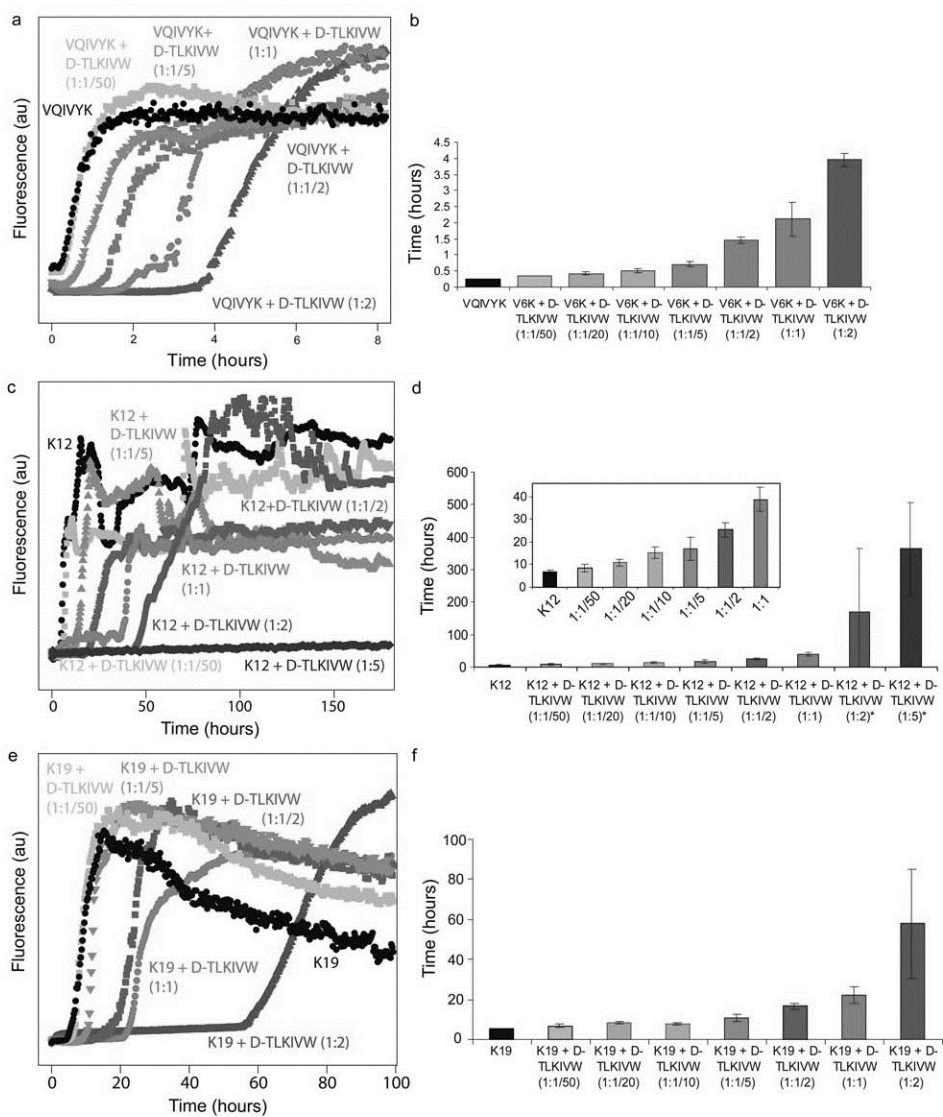


**Supplementary Figure 3. Steric repulsion between D-TLKIVW and VQIVYK molecules disrupts fibril growth.** The modeled interaction between D-TLKIVW and VQIVYK suggests that growth cannot continue on the  $\beta$ -sheet across from the sheet capped by D-TLKIVW. **a**, The view perpendicular to the fibril axis shows a steric clash between adding an additional VQIVYK segment on the purple sheet opposite the  $\beta$ -strand capped by the inhibitor molecule. **b**, Rotating the view so that the fibril axis is perpendicular to the plane of the figure shows that the C $\delta$ 2 of D-Leu2 of D-TLKIVW provides steric interference, preventing the addition of a VQIVYK molecule across from it, specifically via a clash with the Ile308 C $\delta$ 1 and Val306 C $\gamma$ 1 atoms.



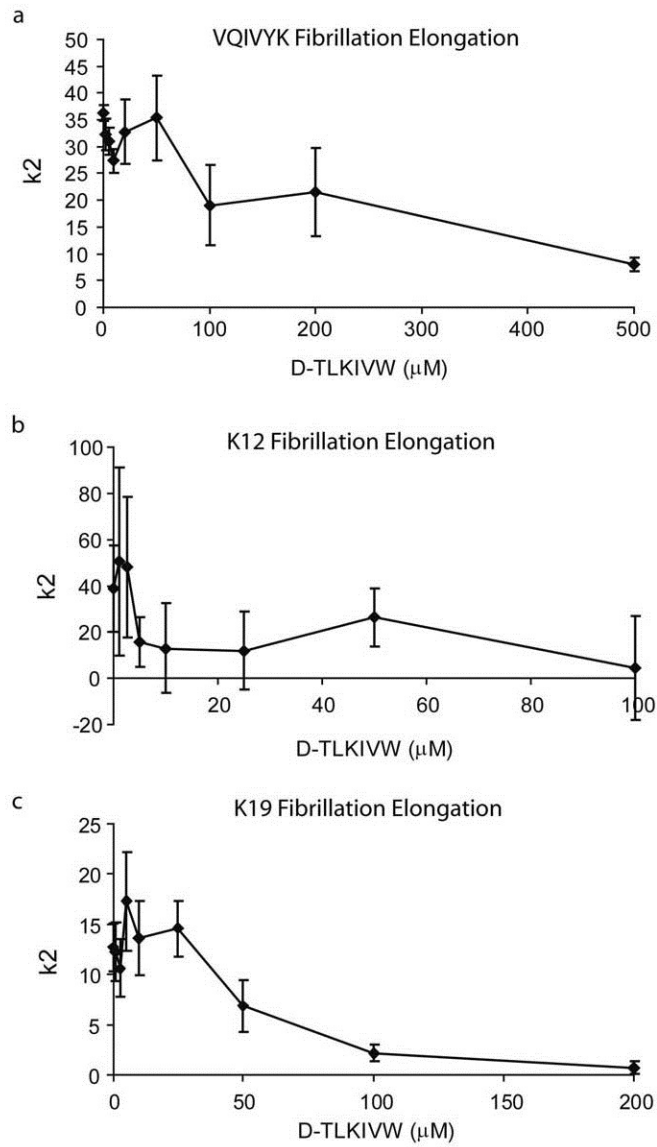
**Supplementary Figure 4. Designed D-peptides delay VQIVYK and tau K12 fibril formation.** **a**, The fibril formation of 50  $\mu$ M K12 was monitored using ThS fluorescence. Traces are shown for the replicate with median lag time. The tau K12 construct forms fibrils after about 15 hours (black). Incubating tau with equimolar quantities of each D-peptide resulted in no inhibition (D-DYYFEF, green), moderate delay (D-YVIIER, cyan), a lag of more than 50 hours (D-TWKLVL, blue), or inhibition for several days (D-TLKIVW, red). K12 fluorescence traces were smoothed to reduce signal noise. **b**, Lag time plots show the variation in the time for fibril formation to begin (error bars represent 1 s.d.). While D-DYYFEF does not show clear inhibition, the other 3 inhibitors clearly

delay fibril formation, with D-TLKIVW delaying fibril formation for more than 100 hours in this experiment. The asterisk indicates that not all replicates had begun fibril formation at the end of the experiment and mean lag time could not be accurately determined. **c**, The fibril formation of 100  $\mu$ M VQIVYK begins in about 15 minutes alone or in the presence of equimolar D-DYYFEF, but is delayed by equimolar D-YVIIEE, D-TWKLVL, and D-TLKIVW. **d**, Lag time plots indicate little variation among the 6 replicates in this experiment and a significant delay due to D-TLKIVW.



**Supplementary Figure 5. D-TLKIVW delays fibril formation in a ratio-dependent manner.** Monitoring ThS fluorescence as a function of time yields the fluorescence curves of **a**, 100  $\mu\text{M}$  VQIVYK; **c**, 50  $\mu\text{M}$  K12; and **e**, 50  $\mu\text{M}$  K19. All samples are delayed

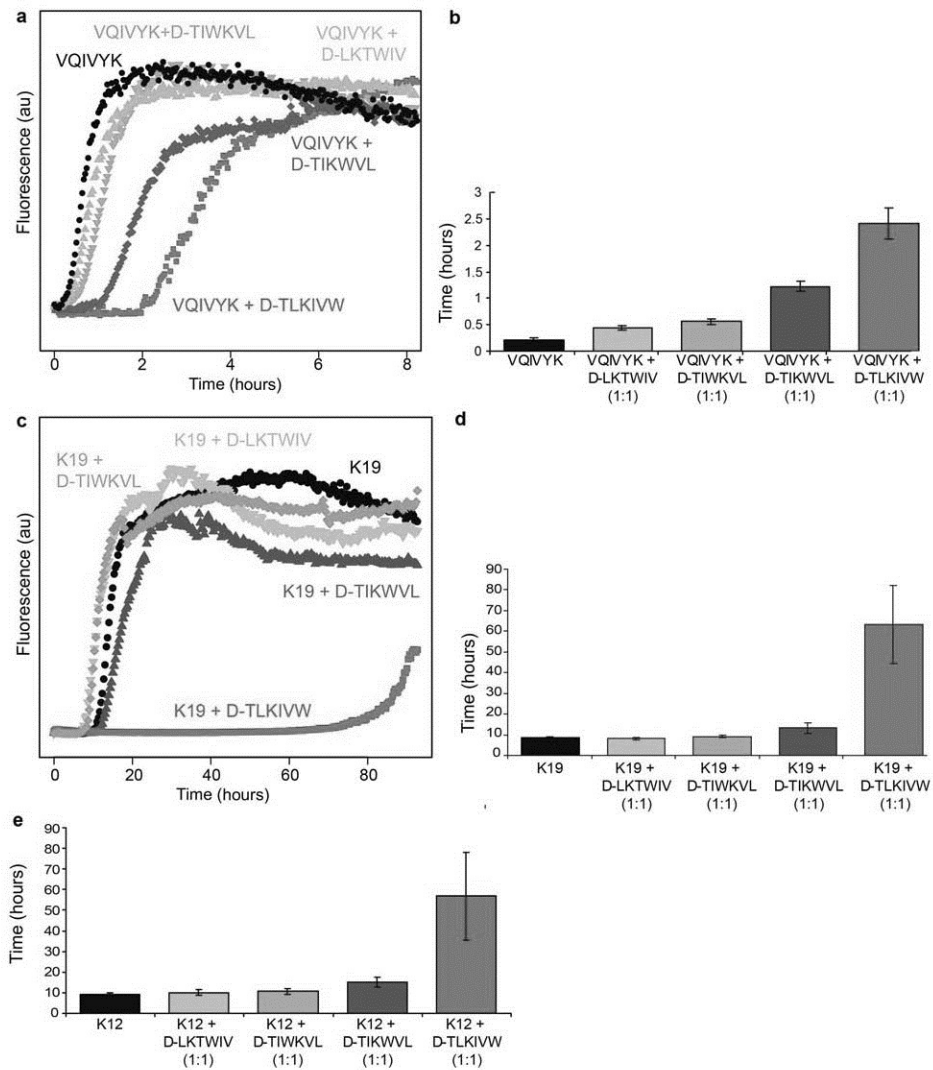
longer by higher concentrations of the D-TLKIVW peptide. The fluorescence of the replicate with the median lag time is shown. Modest inhibitory effects can be seen at sub-stoichiometric ratios for all samples. A delay of several days can be seen when excess D-TLKIVW is present. Lag times for each sample demonstrate the effect of increasing inhibitor concentrations and the variation among replicates for **b**, VQIVYK; **d**, K12; and **f**, K19. Error bars represent the standard deviation of the lag time for four (VQIVYK) and 8 (K12 and K19) replicates at each ratio in this experiment. In panel **d**, the inset expands the time axis to show the differences between the peptide ratios at lower concentrations of the D-peptide. Asterisks indicate that not all replicates had begun to form fibrils at the conclusion of the experiment and a mean lag time and standard deviation could not be determined accurately.



**Supplementary Figure 6. D-TLKIVW decreases the fibril propagation rate of VQIVYK and the tau constructs K12 and K19. Plots of  $k_2$  (proportional to the fibril**



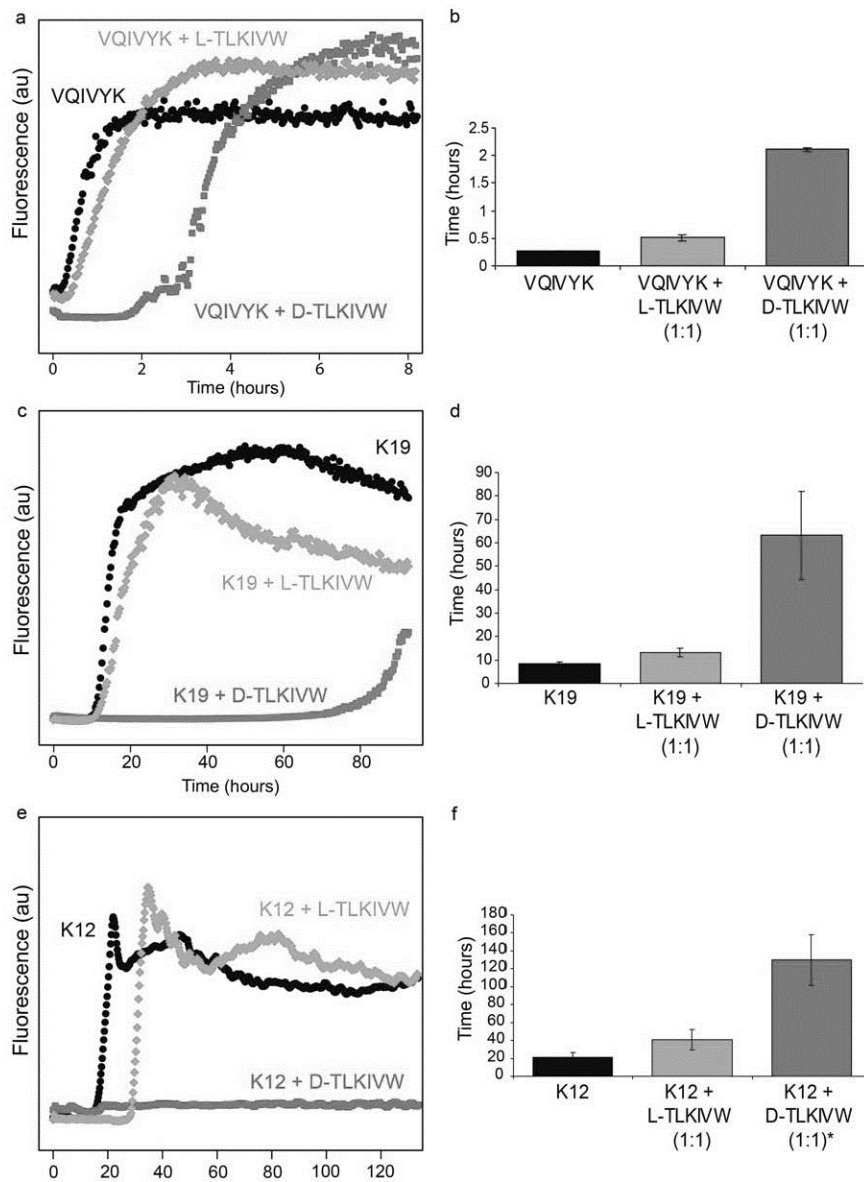
elongation rate) as a function of increasing D-TLKIVW concentrations in fibril formation experiments of **a**, 100  $\mu\text{M}$  VQIVYK; **b**, 50  $\mu\text{M}$  K12; and **c**, 50  $\mu\text{M}$  K19 show that at higher concentrations of D-TLKIVW the rate of fibril growth after initiation is slower. The plots shown are determined from the data shown in Supplementary Fig. 5 with 4 replicates for each sample in the VQIVYK assay and 8 replicates for each assay with the tau constructs.



**Supplementary Figure 7. Scrambled inhibitors demonstrate sequence specificity**

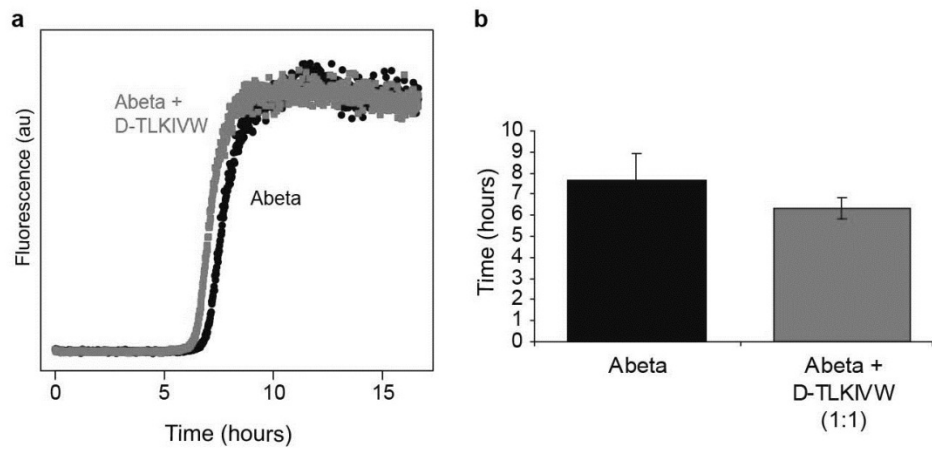
**in the design model.** Monitoring ThS fluorescence shows that in the presence of equimolar peptide the fibril formation of **a**, 100  $\mu$ M VQIVYK; **c**, 50  $\mu$ M K19; and 50  $\mu$ M K12 (Fig. 2e) is delayed significantly by D-TLKIVW and only slightly by D-TIKWVL (with

3 residues on 1 side of the  $\beta$ -strand permuted), while D-TIWKVL and D-LKTWIV have no effect on tau fibril formation. The traces of replicates with the median lag time are shown in **a** and **c**. **b**, **d**, and **e**, Lag time plots for VQIVYK, K19, and K12 fibril formation show the variation of replicates in each experiment. The error bars represent the standard deviations of the lag times for the 6, 4, and 3 replicates in the VQIVYK, K19, and K12 experiments, respectively.

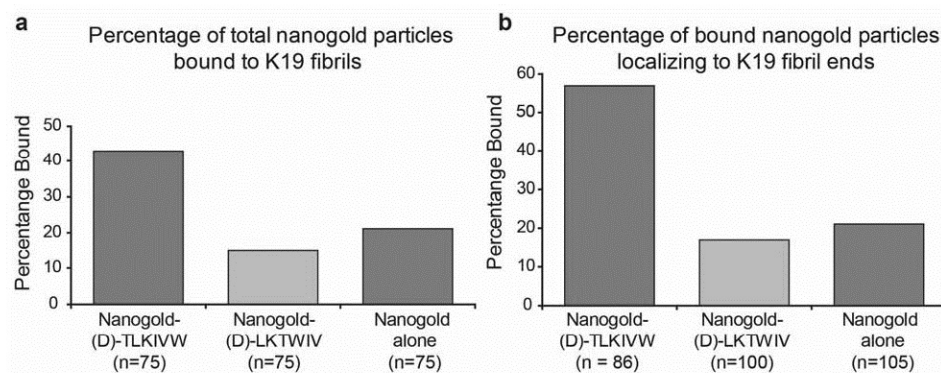


**Supplementary Figure 8. L-TLKIVW diastereomer has little effect on tau fibril formation.** The fibril formation of the tau peptide and constructs alone is shown in

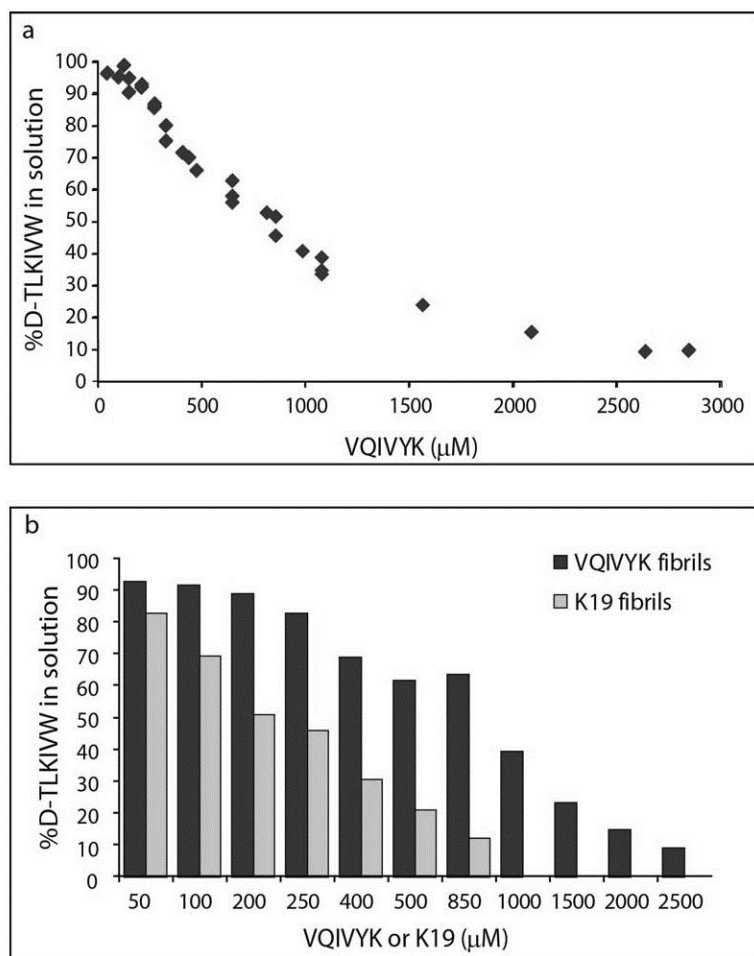
black. Comparing inhibition by equimolar D-TLKIVW to its diastereomer shows that D-TLKIVW (red) delays fibril formation much longer than L-TLKIVW (green). Fibril formation plots showing the ThS fluorescence traces of the sample with median lag time demonstrate that the designed D-amino acid peptide is much more effective than its L-amino acid diastereomer. **a** and **b**, show the fibril formation plot and lag time plots for 100  $\mu$ M VQIVYK in the presence of either D- or L-TLKIVW, with 4 replicates per sample. **c** and **d**, show the fluorescence and lag time plots for 50  $\mu$ M K19 fibril formation with 4 replicates. **e**, The fibril formation plots for 50  $\mu$ M K12 with the 2 peptides are shown. Each K12 fluorescence trace was smoothed to reduce signal noise. **f**, The lag time plot for K12 with each diastereomer shows that the L-peptide has a minor effect on K12 fibril formation compared to the much larger effect of the D-amino acid stereoisomer. The asterisk for K12 plus equimolar D-TLKIVW indicates that 7 of 8 replicates had not begun to form fibrils after 140 hours in the experiment and the mean and standard deviation could not be accurately calculated, with the mean being underestimated.



**Supplementary Figure 9. D-TLKIVW is not a general inhibitor of fibril formation. a,** As monitored by ThT fluorescence, fibril formation of 11.5  $\mu$ M amyloid beta peptide (black) is not delayed by the addition of equimolar D-TLKIVW (red). The trace of the replicate with median lag time is displayed for both samples. **b,** The lag time plot indicates that D-TLKIVW does not have a significant effect on amyloid beta fibril formation. Error bars represent the standard deviation of the lag times of the four replicates per sample.

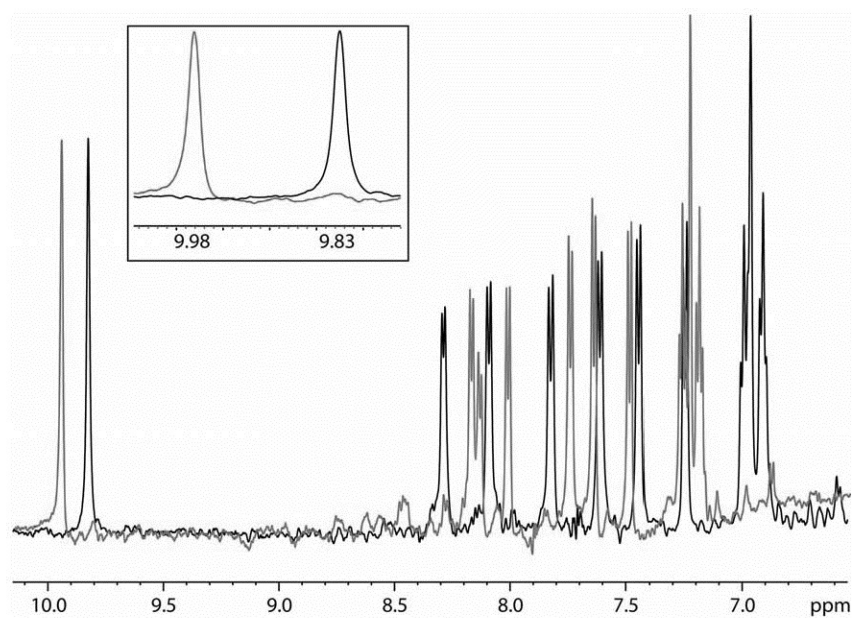


**Supplementary Figure 10. Quantification of nanogold-labeled D-TLKIVW bound to K19 fibrils.** **a**, This plot shows the percentage of nanogold particles bound to fibrils compared to those unbound. Nanogold-bound D-TLKIVW molecules have a preference to interact with K19 fibrils compared to nanogold-bound D-LKTWIV, and nanogold alone. **b**, This plot shows the percentage of nanogold particles bound to K19 fibrils that localize to fibril ends. Of nanogold particles found bound to K19 fibrils, nanogold-bound D-TLKIVW molecules have a preference for K19 fibril ends when compared to nanogold-bound D-LKTWIV, and unbound nanogold.



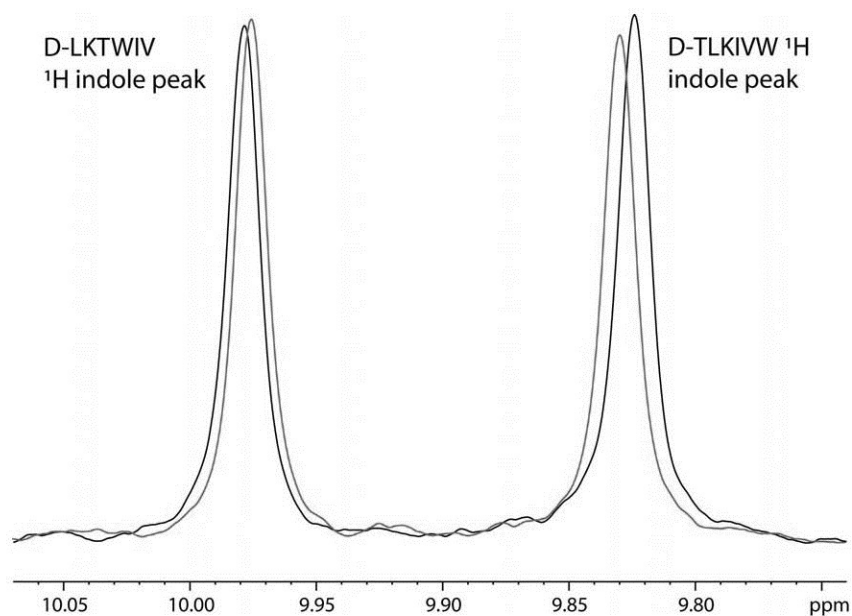
**Supplementary Figure 11. D-TLKIVW interacts with VQIVYK and K19 fibrils.** **a**, The plot shows the percentage of D-TLKIVW no longer in solution as a function of increasing concentrations of fibrillar VQIVYK. **b**, The plot compares the percentage of D-TLKIVW no longer in solution in the presence of VQIVYK fibrils (dark blue) and K19 fibrils (light blue). The concentrations shown are for VQIVYK or K19 monomers in each fibril sample, since fibril concentration can only be estimated.



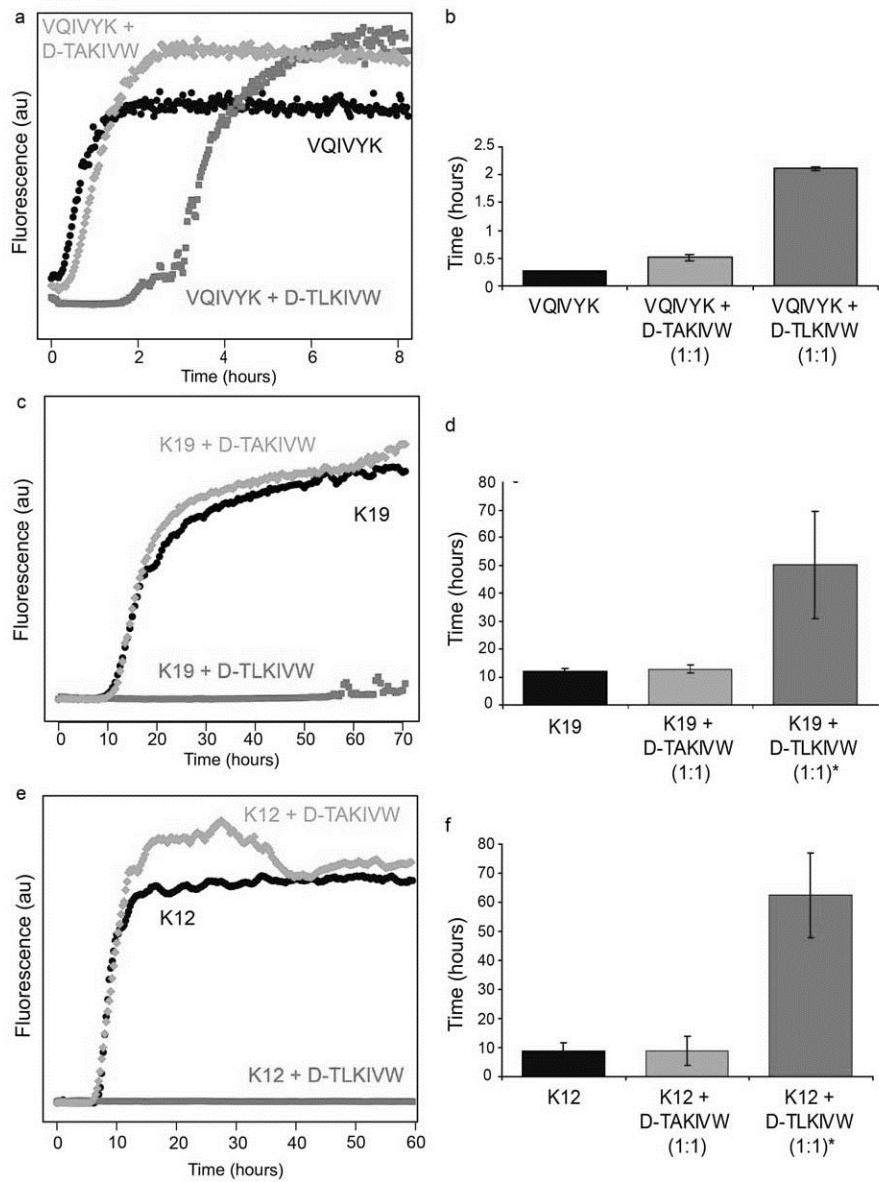


**Supplementary Figure 12. The 500 MHz <sup>1</sup>H spectra of D-TLKIVW and D-LKTWIV.**

The 500 MHz <sup>1</sup>H NMR spectra of D-TLKIVW and D-LKTWIV are shown in black and red, respectively. The inset shows the Trp indole region of both peptides, with the peak of D-TLKIVW around 9.83 ppm and D-LKTWIV around 9.98 ppm.



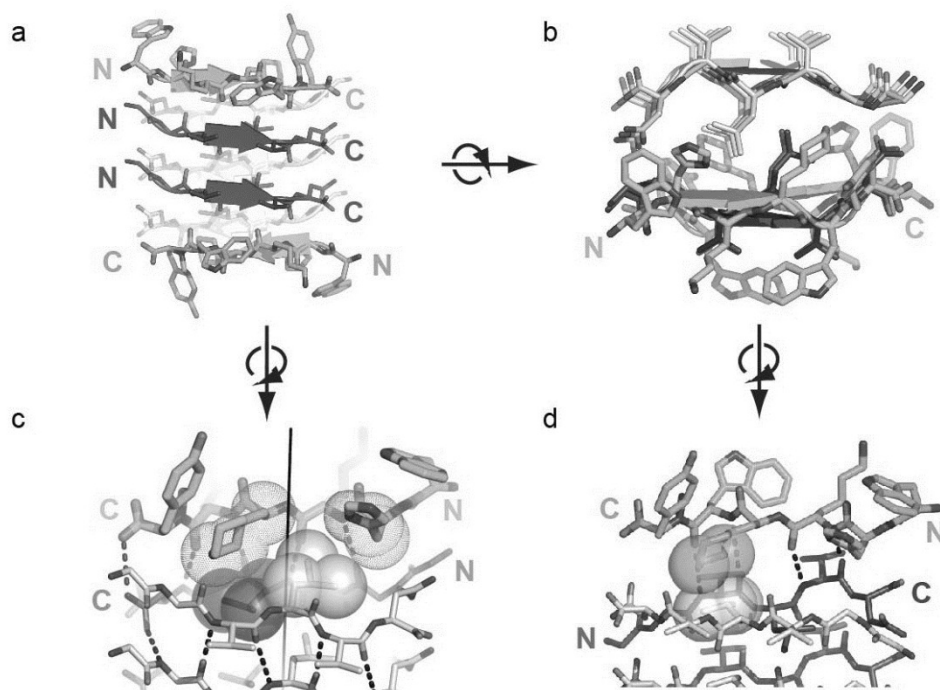
**Supplementary Figure 13. D-TLKIVW does not interact with soluble VQIVYK.** The indole region of the 500 MHz <sup>1</sup>H NMR spectra of 100  $\mu$ M D-TLKIVW and D-LKTWIV peptides in the absence (black) presence of 7 mM soluble VQIVYK (red) is shown. Small differences in the indole peaks for both D-TLKIVW and D-LKTWIV when 70-fold excess VQIVYK is present indicate that neither peptide interacts strongly with soluble VQIVYK.



**Supplementary Figure 14. D-TAKIWW has little effect on tau fibril formation.**

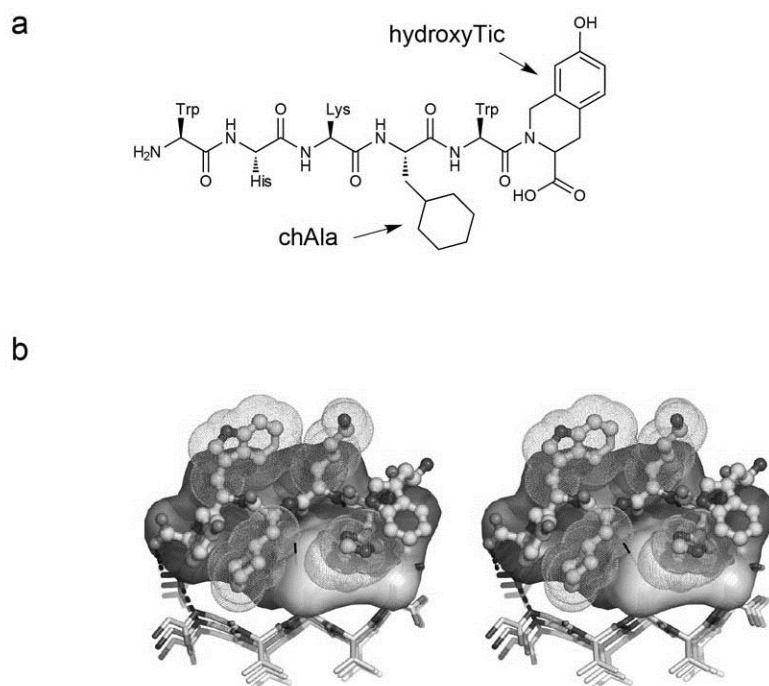
Equimolar D-TLKIVW (red) delays fibril formation while D-TAKIWW (green) has no effect.

Fibril formation plots show the ThS fluorescence trace of the sample with median lag time and indicate that the substitution of D-Leu2 with D-Ala in the designed inhibitor eliminates inhibition activity. **a** and **b**, show the fibril formation plot and lag time plots for 100  $\mu$ M VQIVYK (black) in the presence of either D-TLKIVW (red) or D-TAKIVW (green), with 4 replicates per sample. **c** and **d**, show the plots for K19 fibril formation with 8 replicates per sample. **e** and **f**, show the plots for K12 fibril formation with 12 replicates per sample. Each K12 fluorescence trace was smoothed to reduce signal noise. Asterisks indicate that not all replicates had begun fibril formation by the end of the experiment, preventing the accurate determination of the mean and standard deviation in these cases. Error bars represent the standard deviations of the replicates for each sample.

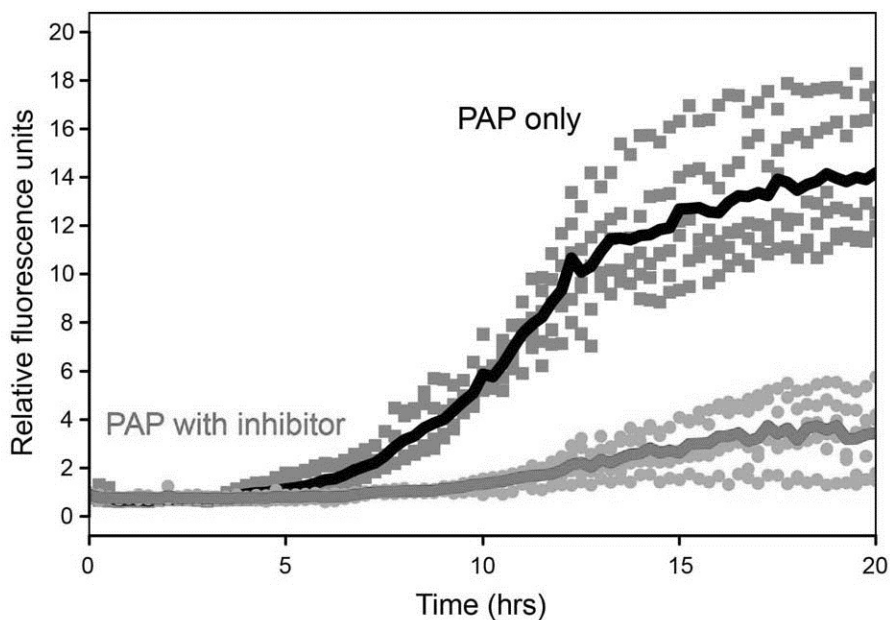


**Supplementary Figure 15. Binding orientations of designed inhibitor of  $^{248}\text{PAP}^{286}$  fibril formation.** The peptide inhibitor, WW61, designed using the GGVLVN template from PAP is shown. **a** and **b** show the side view and top-down views of the designed inhibitor interactions, respectively. Two possible binding modes are proposed: 1) the peptide inhibitor (cyan) aligns on the top of the fibril parallel to one of the  $\beta$ -sheets; 2) the peptide inhibitor (cyan) aligns on the bottom of the fibril in an anti-parallel orientation relative to one of the fibril's  $\beta$ -sheets. The N- and C- termini of the  $\beta$ -strands of the fibril and inhibitor are labeled. **c**, The side view of the parallel binding mode (1). This binding mode is from the original design with favorable calculated binding energy. The side chains of chAla and His (cyan dotted spheres) make favorable interactions with the

core residues Leu (purple and grey spheres) from the GGVLVN molecule. Only the contact atoms are shown in sphere representation to highlight their apolar interactions. The black dashed lines represent hydrogen bonds. 1 backbone-side-chain and 4 backbone-backbone hydrogen bonds between the inhibitor and fibril end are shown. **d**, The side view of the anti-parallel binding mode (2). This binding mode is not used in our original design model, and it has less favorable interactions, as calculated. The anti-parallel binding mode shares a similar binding interface to the parallel model with the same contacting residue pairs and atomic interactions. Although our original design is based on the parallel mode with more favorable calculated binding energy, we cannot exclude the possibility of the peptide inhibitor binding to the fibril end in some other way, such as in an anti-parallel orientation.

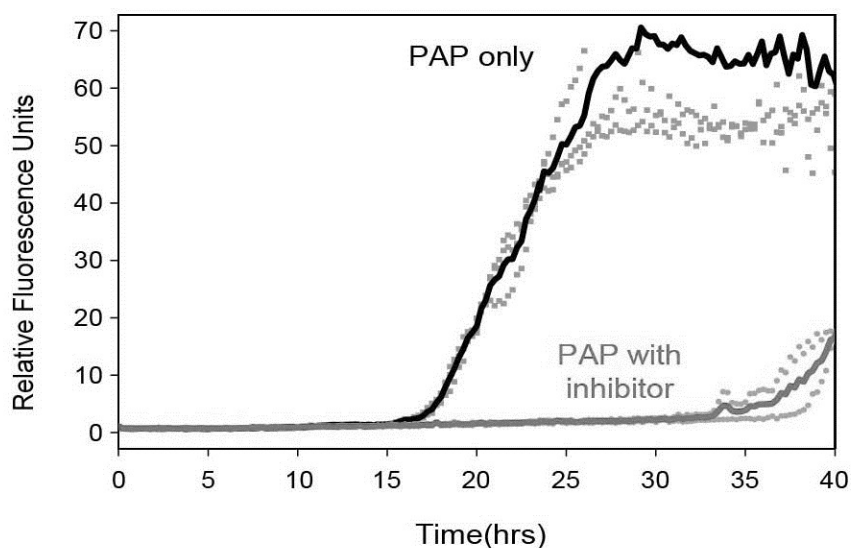


**Supplementary Figure 16. The chemical structure of the non-natural peptide Trp-His-Lys-chAla-Trp-hydroxyTic (WW61).** **a**, ChAla represents  $\beta$ -cyclohexyl-L-alanine and hydroxyTic is 7-hydroxy-(S)-1,2,3,4-tetrahydroisoquinoline-3-carboxylic acid. The N- and C-termini of the peptide are free. **b**, The wall-eyed stereo image shows how the designed inhibitor peptide (cyan ball-and-stick) is predicted to interact with the peptide segment GGVLVN. The surface representation of the fibrillar GGVLVN highlights the tight interactions between the non-natural chAla from the inhibitor and the core residue Leu from the fibrillar GGVLVN template. The 4 inner residues of the peptide inhibitor are shown in dot-sphere representation to emphasize their shape complementarity to the outer residues of the inhibitor, and to the fibrillar GGVLVN structure.

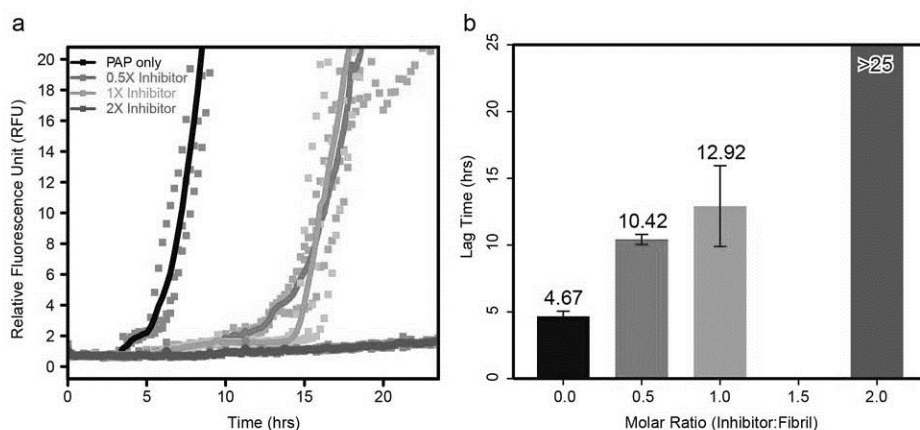


**Supplementary Figure 17. Inhibitory effect of the designed peptide WW61 on seeded  $^{248}\text{PAP}^{286}$  fibril formation.**  $^{248}\text{PAP}^{286}$  fibril formation was monitored by observing ThT fluorescence over time for samples with 5 replicates. In the presence of preformed  $^{248}\text{PAP}^{286}$  fibrils, there is an increase in fluorescence in  $^{248}\text{PAP}^{286}$  alone after about 5 hours and fibrils are observed by electron microscopy. In the presence of 2-fold excess inhibitor, there is a small rise in signal, but fibrils were not observed by electron microscopy (Supplementary Fig. 20). The signal remains low for more than 50 hours (see Fig. 4c). Solid red and black lines show mean fluorescence values with and without inhibitor, respectively.

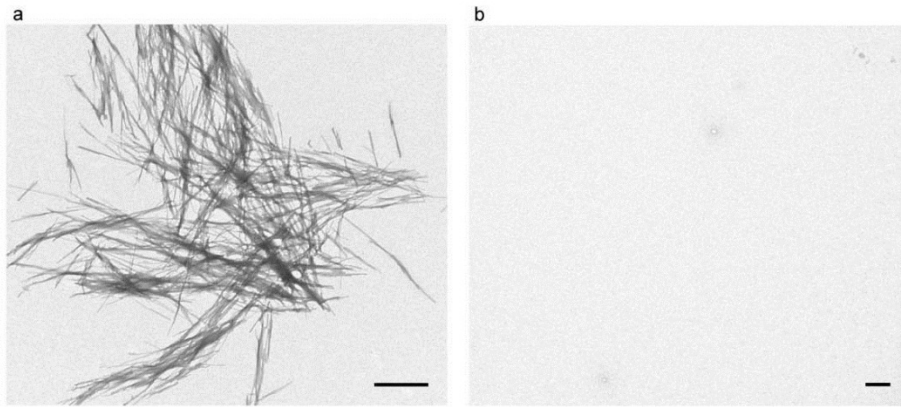




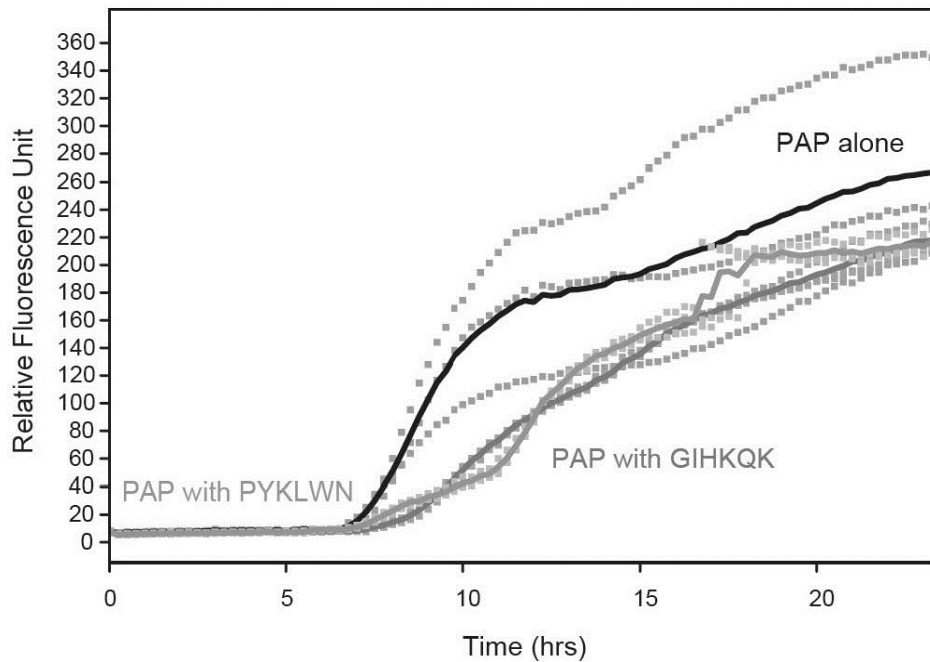
**Supplementary Figure 18. Inhibitory effect of the designed peptide, WW61, on unseeded  $^{248}\text{PAP}^{286}$  fibril formation.**  $^{248}\text{PAP}^{286}$  fibril formation was monitored by observing ThT fluorescence over time for samples in triplicate. The lag time for 0.66 mM  $^{248}\text{PAP}^{286}$  alone (grey dots) was  $17 \pm 0.2$  hours (s.d.), based on an arbitrary fluorescence value cutoff of 3. When a 2-fold molar excess of the inhibitor peptide was present, the lag time of  $^{248}\text{PAP}^{286}$  fibril formation (pale red dots) was extended to  $35 \pm 3$  hours (s.d.). Solid red and black lines show mean fluorescence values with and without inhibitor, respectively.



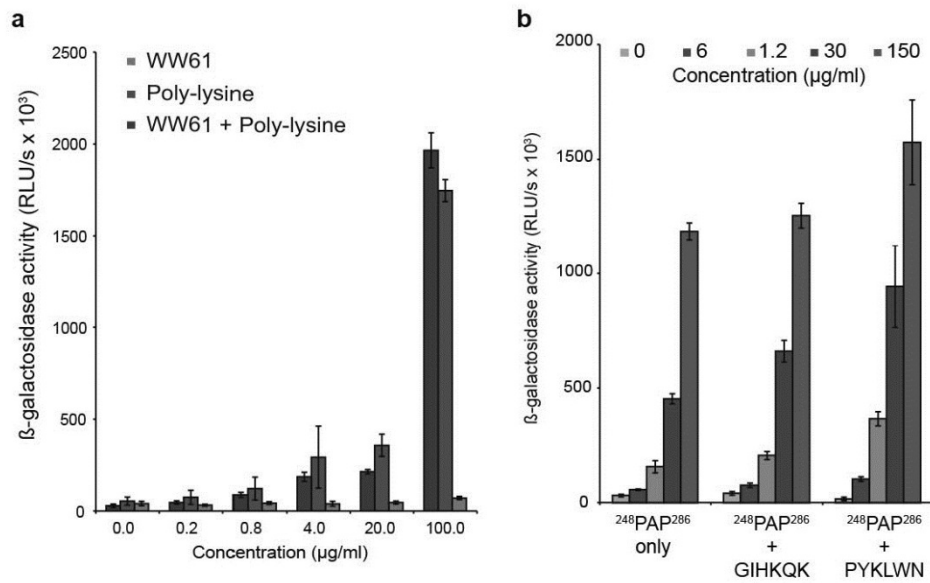
**Supplementary Figure 19. The non-natural peptide WW61 shows a ratio-dependent inhibition effect on seeded  $^{248}\text{PAP}^{286}$  fibril formation.** **a**,  $^{248}\text{PAP}^{286}$  fibril formation was monitored by observing ThT fluorescence over time when varying the molar ratio of peptide inhibitor and  $^{248}\text{PAP}^{286}$ . Three replicates were plotted for each molar ratio (PAP only, 1:2, 1:1, 1:0.5). The solid lines show the average value of the fluorescence traces. **b**, The plot of molar ratio vs. lag time of  $^{248}\text{PAP}^{286}$  fibril formation. The lag time for  $^{248}\text{PAP}^{286}$  fibril formation is determined by the starting time whose ThT fluorescence is greater than an arbitrary fluorescence value of 2. The error bar indicates the standard deviation of the lag times for the three replicates of each sample.



**Supplementary Figure 20. Negative-stain electron micrographs show the effect of the inhibitor WW61 on  $^{248}\text{PAP}^{286}$  fibril formation.** **a**, The electron micrograph shows fibrils of  $^{248}\text{PAP}^{286}$ . **b**, Fibril formation of  $^{248}\text{PAP}^{286}$  is inhibited by a 2-fold excess of the non-natural amino acid inhibitor, WW61. Samples were prepared following 20 hours of incubation with  $^{248}\text{PAP}^{286}$  seeds (scale bars, 1  $\mu\text{m}$ ).



**Supplementary Figure 21. No inhibitory effect of the control peptides GIHKQK and PYKLWN on seeded  $^{248}\text{PAP}^{286}$  fibril formation.** GIHKQK, a peptide segment from the N-terminal region of  $^{248}\text{PAP}^{286}$ , not involved in SEVI formation, and PYKLWN, an unrelated peptide with the same charge as the designed inhibitor WW61, were selected as negative controls. ThT fluorescence was used to monitor the fibril formation of 0.66 mM  $^{248}\text{PAP}^{286}$  over time in the absence (grey dots) and presence of the 2-fold molar excess of the control peptides, GIHKQK (red dots) and PYKLWN (green dots). The solid lines show the average value of the fluorescence traces.



**Supplementary Figure 22. Control HIV infectivity assays.** HIV infection rates were determined by measuring reporter enzyme activity in cellular lysates. The mean values derived from triplicate infections are shown. Error bars represent one standard deviation. RLU/s; relative light units per second. **a**, WW61 alone does not affect HIV-1 infection and does not affect poly-lysine mediated infectivity enhancement. **b**, Control peptides GIHKQK and PYKLWN do not affect HIV-1 infection rates.

**Supplementary Table 1.** Comparison of D-peptides and controls.

| <b>Sequence</b>            | <b><math>\Delta</math>Binding energy</b> | <b>Area buried (Å<sup>2</sup>)</b> | <b>Shape complementarity</b> | <b>Inhibitory activity</b> |
|----------------------------|--|------------------------------------|------------------------------|----------------------------|
| <b>Designed inhibitors</b> |  |                                    |                              |                            |
| D-TLKIVW                   | -1.7                                     | 327                                | 0.78                         | ++++                       |
| D-TWKLVL                   | 0.3                                      | 342                                | 0.81                         | +++                        |
| D-YVIIER                   | 8.8                                      | 261                                | 0.80                         | ++                         |
| D-DYYFEF                   | 1.2                                      | 358                                | 0.78                         | +                          |
| <b>Negative controls</b>   |  |                                    |                              |                            |
| D-TAKIVW                   | 3.0                                      | 313                                | 0.79                         | -                          |
| L-TLKIVW                   | 3.4                                      | 386                                | 0.72                         | +                          |
| D-TIKWWL                   | 9.9                                      | 313                                | 0.72                         | +                          |
| D-TIWKVL                   | 11.7                                     | 316                                | 0.65                         | -                          |
| D-LKTWIV                   | 12.2                                     | 350                                | 0.72                         | -                          |

Activity is ranked from highest activity (++++) to no activity (-). Each peptide model was minimized using RosettaDesign allowing both the template and inhibitor to move freely. The change in binding energy shown is in reference to an equivalent L-VQIVYK peptide in the same position. Values for area buried and shape complementarity were determined from the final models.

**Supplementary Table 2.** Data collection and refinement statistics (Molecular replacement)

|   | GGVLVN  |
|---|---|
| <b>Data collection</b>                              |   |
| Space group   | P2 <sub>1</sub> 2 <sub>1</sub> 2 <sub>1</sub> |
| Cell dimensions                                     |   |
| <i>a</i> , <i>b</i> , <i>c</i> (Å)                  | 4.83, 17.7, 40.3                              |
| $\alpha$ , $\beta$ , $\gamma$ (°)                   | 90.00, 90.00, 90.00                           |
| Resolution (Å)                                      | 1.50 (1.55-1.50)*                             |
| <i>R</i> <sub>sym</sub>                             | 0.149 (0.256)                                 |
| <i>I</i> / $\sigma$ <i>I</i>                        | 8.9 (4.5)                                     |
| Completeness (%)                                    | 86.4 (74.0)                                   |
| Redundancy  | 4.9 (2.6)                                     |
| <b>Refinement</b>                                   |   |
| Resolution (Å)                                      | 1.5   |
| No. reflections                                     | 548   |
| <i>R</i> <sub>work</sub> / <i>R</i> <sub>free</sub> | 0.182/0.219                                   |
| No. atoms   |   |
| Protein   | 39  |
| Ligand/ion  | 5   |
| Water   | 1   |
| B-factors   |   |
| Protein   | 8.7   |
| Ligand/ion  | 17.5  |
| Water   | 13.8  |
| R.m.s deviations                                    |   |
| Bond lengths (Å)                                    | 0.003   |
| Bond angles (°)                                     | 1.291   |

Datasets from two crystals were used in GGVLVN structural determination.

\*Highest resolution shell is shown in parenthesis.

## Chapter 3: The Supramolecular Structure of Tau Fibrils

### **Abstract**

Tauopathies are neurodegenerative diseases characterized by the appearance of highly-ordered aggregates found in patient brains. Tau protein fibrils constitute the principal protein component of these aggregates. The steric zipper model offers a model for how the highly-ordered amyloid fibrils are arranged at its core, but evidence for such in the context of tau protein fibrils was lacking. To address this gap, we set out to acquire mass-per-length measurements of fibrils formed by K19, a truncated form of tau protein that omits regions susceptible to proteolysis in the fibril. The data we acquired indicate that the thinnest observed filaments, sometimes called protofibrils, are comprised of a pair of beta-sheets, and coiled pairs of beta-sheets constitute the thicker fibrils. These data strongly support the steric zipper model, and aid in explaining observations we made in inhibitor localization experiments detailed in the previous chapter.



# Introduction

## Tau protein

First isolated in 1975, tau protein is a 55-62 kDa protein initially identified for its ability to induce tubule formation (Weingarten et al., 1975; Olmsted, 1986). Later, it was found to incorporate itself into growing microtubules, a major component of the eukaryotic cytoskeletal system (Witman et al, 1976; Olmsted and Borisy, 1983). For this reason, tau is also frequently referred to as microtubule associated protein (MAPT). Aside from integrating into and stabilizing microtubules, tau protein also plays essential roles in regulating microtubule dynamics, anchoring intracellular enzymes, and assisting in modulating vesicular transport (Cassimeris and Spittle, 2001; Drubin and Kirschner, 1986; Garcia and Cleveland, 2001;). Tau proteins are essential to the cellular division processes meiosis and mitosis, and constitute a major part of nerve axons (Schmitt, 1968).

Lacking a stable tertiary structure, tau was the first protein to be characterized as “natively unfolded” (Schweers et al., 1994). Tau protein also exhibits almost no secondary structure (Cleveland et al., 1977). This can likely be attributed to the high proportion of hydrophilic amino acid residues found in tau (**Figure 3.1**), which precludes typical protein folding. Using the Kyte and Doolittle approximations of hydrophobicity normalized to a scale of 0 to 1, the longest tau isoform possesses a mean hydrophobicity of just 0.40 (Kyte and Doolittle, 1982; Jeganathan et al., 2008). This value is comparable to that of heat shock transcription factor from *S. cerevisiae*, another natively unfolded protein, (0.41), and low when compared to some commonly studied proteins with a well-defined structure, such as dihydrofolate reductase (0.49) and lysozyme (0.49). Such a low proportion of hydrophobic residues results in a protein

that is still able to carry out its native function of binding and stabilizing microtubules, even after experiencing high heat or extremely acidic conditions that would render most proteins dysfunctional (Barghorn et al., 2005).

## **Tauopathies**

To date, over 20 different dementias and movement disorders have been described that manifest neurofibrillary tangles in patient brains. These diseases are collectively termed tauopathies (**Table 3.1**). There are two major hypotheses regarding the role of tau in tauopathies, though they are not mutually exclusive. The first is that its dissociation from microtubules leads to a loss of physiological function, driving toxicity (Hasegawa et al., 1998; Makrides et al., 2003; Halliday et al., 2012). The other is that some form of tau aggregates themselves is neurotoxic, representing a gain-of-function mechanism of toxicity. The strongest evidence for the gain-of-function hypothesis is that the amount of neurofibrillary tangles in patients' brains correlates with the duration and severity of Alzheimer's disease (Arriagada et al., 1992). Additionally, another group has shown that expressing full-length human tau in HEK293 cells in culture leads to large scale aggregation, and significant losses in cell viability over a period of days (Bandyopadhyay et al., 2007).

The major structural component of the tangles seen in tauopathies is the paired helical filament (PHF). One investigation that utilized spectroscopic techniques claimed PHFs to be comprised largely of alpha-helices (Sadqi et al., 2002). But, the experiments demonstrating alpha-helical characteristics were conducted on PHFs isolated from the brain, a preparation that does not guarantee sample purity. Later work on homogenous specimens of recombinantly

expressed tau showed that PHFs indeed have clear cross-beta structure, a feature of amyloid fibrils in general (Berriman et al., 2003; Inouye et al., 2006; Kirschner et al., 1986). These conclusions were supported in large part by X-ray fiber diffraction experiments. When shot with an X-ray beam, these fibrils yield a sharp meridional reflection at 4.8 Å, indicating that protein chains extend perpendicular to the long axis of the fibril, spaced 4.8 Å apart. A more diffuse equatorial signal at around 10 Å (Stromer and Serpell, 2005) shows that these extended strands organize into sheets spaced ~ 10 Å apart (Eisenberg and Jucker, 2012).

Work by several laboratories later revealed that PHFs are composed of all six full-length tau isoforms (**Figure 3.2**), hyperphosphorylated beyond what is observed in a non-disease state (Grundke-Iqbal et al. 1986; Lee et al. 1991; Goedert et al. 1992). It is largely accepted that this hyperphosphorylation is necessary for tau protein to transition from the soluble form to the aggregated state associated with disease (Braak et al., 1994). By shielding the numerous cationic amino acids found in tau from each other, repulsion between monomers is reduced, and local concentrations increased. Further supporting this theory, a polyanionic cofactor is typically required to induce tau fibrillation *in vitro*. This can be RNA (Kampers et al., 1996), heparin (Goedert et al., 1996), or arachidonic acid (Wilson and Binder, 1996).

### **The fibrillogenic core of tau filaments**

Depending on the specific isoform, tau protein contains three or four microtubule binding regions. These regions are characterized by pseudorepeat domains that contain a Pro-Gly-Gly-Gly motif (Butner and Kirschner, 1991; Good and Feinstein, 1994). By limited proteolysis, these domains were found to reside in the core of PHFs, and to readily form PHF-

like assemblies in isolation. (Wille et al., 1992; Kondo et al., 1988, Wischik et al., 1988a). Further paring down the fibrillation-prone region, others showed that the segment <sup>306</sup>VQIVYK<sup>311</sup>, derived from within the third microtubule binding region, necessarily assumes an extended beta-strand conformation in tau fibrils, and forms amyloid-like fibrils itself (von Bergen et al., 2000; Goux et al., 2004).

In 2007, Sawaya et al. published >11 atomic-level microcrystal structures of peptide segments that comprise the spine of amyloid fibrils, revealing extensive surface complementarity between mating beta-sheets. For its wholesale exclusion of solvent and the tight interdigitation of side chains, this interface was coined the steric zipper (Nelson et al., 2005). <sup>306</sup>VQIVYK<sup>311</sup> was among the structures solved in this work, and we utilized the atomic details of the spine to computationally design D-peptide inhibitors of fibril formation (Sievers et al., 2011). As part of that study, I labeled the inhibitor with Nanogold particles to confirm that it binds to fibrils of K19, a protein construct of tau. I determined that inhibitor-labeled Nanogold bound K19 fibrils nearly three times more frequently than Nanogold labeled with a control peptide, or unconjugated Nanogold alone. Our tally also revealed that, although the labeled inhibitor localized to fibril ends more frequently than labeled control peptides with statistical significance, approximately 45% of labeled inhibitor still appeared to bind distally from the targeted fibril end.

Given this observation, we sought to explain why the inhibitor appears to bind the sides of the fibril so frequently, in addition to its designated target (**Figure 3.3**). We hypothesized that the growing end of the steric zipper, which represents the targeted binding site, could be exposed distally from the apparent end of the a fibril by the presence of overhangs. This could arise from the lateral association of filaments of differing individual length, or from breakages

within intertwined filaments, akin to fraying rope. However, such a supramolecular architecture is difficult to observe via transmission electron microscopy (TEM), as the negative staining typically used to visualize fibrils can obscure finer morphological details. We therefore sought out another method.

## **Scanning transmission electron microscopy**

In contrast to transmission electron microscopy, which stains specimens with heavy metal salts, scanning transmission electron microscopy (STEM) directly visualizes unstained samples (Wall and Hainfeld, 1986). By freeze-drying the specimen, the technique also obviates the need for sample fixation. For these reasons, we opted to probe the organization of these fibrils directly, using STEM. This technique also permits us to make accurate mass per unit length (MPL) measurements of K19 fibrils, as was previously done for insulin (Ivanova et al., 2009).

## **Previous STEM work on tau protein**

Others have roughly analyzed the core of tau filaments by STEM (Wischik et al., 1998b; von Bergen et al., 2006). However, they studied full-length tau and longer protein constructs—ones which result in a “fuzzy coat” morphology under microscopy that interferes with recording precise MPL measurements. Antibody-labeling experiments established that this fuzzy coat is composed of the unstructured N- and C-terminal domains (Wegmann et al., 2012). The effect of these unstructured domains’ interference manifests in their results, wherein the recorded MPL

values exhibit standard deviations of 10% or more. In order to study just the protease-resistant core of tau fibrils, we opted to continue working with K19, a 99 amino acid construct of tau that contains microtubule binding regions R1, R3, and R4, and a short C terminal tail (**Figure 3.5**). Also, based on the histograms of recorded measurements, it is evident that previous studies only measured MPL values for the thinnest filaments within a sample. Before the current work, none has investigated the lateral association between fibrils of non-identical length.

## Results

### **K19 Morphology**

Micrographs from STEM experiments showed that individual filament ends indeed present themselves along the length of K19 fibrils, away from the apparent end of the overall fibril. We observed that this occurs in three general ways. (1) They can arise from a break in one filament that is otherwise intertwined with other filaments (**Figure 3.6a**). (2) Filaments of non-identical length can coil around each other (**Figure 3.6b, c**). And (3), individual short filaments can associate laterally (**Figure 3.6d**).

### **STEM Measurement Normalization**

Reliable absolute scaling of the electron scattering mass requires an internal calibration standard in the images. For each STEM image of the specimens, I collected as many measurements as possible from the TMV particles present (Figure xA), with a total of 380

individual measurements. The average MPL of half of the measured TMV particles was calculated to be  $11.68 \pm 0.64$  kDa/Å. A scaling factor to compute the MPL values of K19 fibrils was calculated by dividing the known TMV value of 13.10 kDa/Å by the average MPL value of TMV particles for half of the measured samples ( $13.10 \text{ kDa}/\text{Å} / 11.68 \text{ kDa}/\text{Å}$ ). To test how well the known MPL value of TMV particles is recovered, the calculated scale factor, 1.22, was used to compute the average MPL value of the remaining half of TMV measurements. The resulting calculated value was  $12.97 \pm 0.54$  kDa/Å, well in agreement with the known mass of 13.10 kDa/Å (Sousa and Leapman, 2007) (**Figure 3.7**).

### **MPL Measurements of K19 fibrils**

A total of 542 measurements were recorded, ranging from 3.46 to 16.0 kDa/Å. Visual inspection of a histogram of the K19 MPL measurements indicated a mixture of three different populations. The Kolmogorov-Smirnov (K-S) statistical test was applied to assess whether a three component model sufficiently describes the data. This test yielded the K-S test statistic  $D = 0.0264$  corresponding to a P value  $> 0.999$ , indicating that the data conform well to the proposed three component Gaussian mixture model.

The most populated grouping of MPL values, measured from the thinnest filament segments, clustered around a mean of  $4.71 \pm 0.41$  kDa/Å (**Figure 3.8**). The second and third most populated groupings clustered around two and three times this value,  $9.44 \pm 0.56$  and  $13.75 \pm 0.91$  kDa/Å, respectively.

## Discussion

### **The growing ends of steric zippers are not located exclusively at fibril ends**

In demonstrating that individual filament ends can be exposed at sites distinct from the overall fibril end, we provide a rationale for why Nanogold-labeled inhibitor binds K19 fibrils more frequently than Nanogold-labeled control peptide, even away from fibril ends. It is clear that much of what was recorded as incidents of the inhibitor binding away from fibril ends could simply be the inhibitor binding an obscured filament end, although the frequency of occurrence remains undefined. One possible method of defining this frequency in future studies would be to visualize Nanogold-labeled inhibitor bound to fibrils using STEM, instead of TEM. This approach could reduce the artifacts seen with TEM, but the additional steps required to prepare STEM samples (liquid nitrogen submersion, freeze-drying) could interfere with the inhibitor's binding of K19 fibrils. That the fibril MPL increases incrementally by two molecules per layer supports the hypothesis that overhangs within a fibril can present exposed steric zipper ends for the inhibitor to bind.

### **MPL measurements support the steric zipper model of amyloid fibrils**

The steric zipper model implies that individual filaments within tau fibrils consist of two molecules per 4.7 Å along the length of the filament. With a molecular mass of 10567 Da, this corresponds to a theoretical value of  $(2 \times 10.57 \text{ kDa}/4.7 \text{ Å}) = 4.50 \text{ kDa}/\text{Å}$  for K19 filaments held together by a steric zipper. This figure is well supported by the most commonly measured MPL value calculated from the STEM images,  $4.71 \pm 0.41 \text{ kDa}/\text{Å}$ . A similar calculation in reverse



indicates that these same filaments are composed of  $[(4.71 \pm 0.41 \text{ kDa}/\text{\AA}) \times (4.7 \text{ \AA}/\text{cross beta layer}) \times (1 \text{ K19 molecule}/10.57 \text{ kDa})] = 2.09 \pm 0.18$  K19 molecules per cross beta layer.

In further support of this model, similar calculations for the second  $[(9.44 \pm 0.56 \text{ kDa}/\text{\AA}) \times (4.7 \text{ \AA}/\text{cross beta layer}) \times (1 \text{ K19 molecule}/10.57 \text{ kDa})]$  and third  $[(13.75 \pm 0.91 \text{ kDa}/\text{\AA}) \times (4.7 \text{ \AA}/\text{cross beta layer}) \times (1 \text{ K19 molecule}/10.57 \text{ kDa})]$  most prevalent populations yield values of  $4.22 \pm 0.27$  and  $6.11 \pm 0.40$  K19 molecules per cross beta layer, respectively. This strongly suggests that these thicker fibrils are composed of intertwined thinner filaments.

## Materials & Methods

### **K19 expression and purification**

Derived from pET-3b, the pNG2 expression vector containing the K19 gene was provided by E. Mandelkow (Spiess et al., 1987; Biernat et al., 1992). Expression in BL21(DE3) *Escherichia coli* (Studier et al., 1990) was induced with 1 mM isopropyl thiogalactoside when the absorbance  $A_{600 \text{ nm}}$  was between 0.8 and 1.0, and cells were collected 3–4 hours following induction. K19 was purified on the basis of previously described methods (Barghorn et al., 2005). Cells were pelleted for 20 minutes at 4,700 x g and resuspended in 20 mM MES, pH 6.8, 1 mM EDTA, 0.2 mM  $\text{MgCl}_2$ , 5 mM DTT, 1 mM PMSF and a protease inhibitor cocktail. The cells were sonicated for 2.5 minutes and, following addition of NaCl to bring cell lysate to 0.5 M NaCl, the lysate was boiled for 20 minutes. The lysate was sedimented at 30,000 x g for 20 minutes and dialyzed twice against 20 mM MES, pH 6.8, 50 mM NaCl, 1 mM EDTA, 1 mM  $\text{MgCl}_2$ , 2 mM DTT and 0.1 mM PMSF at 4° C. The dialysate was pelleted for 20 minutes at 30,000 x g and filtered

before cation exchange chromatography on an AKTA Explorer (GE Pharmacia) with a HighTrap HP SP 5-ml column (GE Healthcare). The sample was eluted with a linear gradient of up to 60% buffer B (20 mM MES, pH 6.8, 1 M NaCl, 1 mM EDTA, 1 mM MgCl<sub>2</sub>, 2 mM DTT and 0.1 mM PMSF). Size exclusion chromatography was optionally performed with a Superdex 75 10/300 GL column (GE Healthcare) in PBS buffer (137 mM NaCl, 3 mM KCl, 10 mM Na<sub>2</sub>HPO<sub>4</sub>, 2 mM KH<sub>2</sub>PO<sub>4</sub>, pH 7.4) with 1 mM DTT on the AKTA Explorer depending on preparation purity as assessed by SDS polyacrylamide gel electrophoresis. Protein concentration was determined by the Micro BCA Protein Assay Kit (Pierce).

### **Transmission electron microscopy**

Samples (5 µl) were applied to glow-discharged, 400-mesh carbon-coated, formvar films on copper grids (Ted Pella) for 3 minutes. Grids were rinsed twice with distilled water and stained with 2% uranyl acetate for 60-75 seconds. Grids were examined in a JEOL JEM1200-EX operating at 80 keV.

### **Preparation of short K19 fibrils**

K19 fibrils were generated by incubating 100 µM of soluble K19 with 25 µM of 6 kDa heparin for 48 hours or longer at 37°C in phosphate buffer (50 mM, pH 7.4). Fibril formation was confirmed by electron microscopy. To acquire short fibrils, K19 fibrils were sonicated for 15 seconds, using a microtip set to 35% amplitude, and operating in intervals of 1 second on followed by 1 second off. Residual heparin was removed by centrifuging the sonicated mixture

through a 100 kDa Microcon concentrator for 10 minutes at 14,000 g, washing the retentate with phosphate buffer, and re-centrifuging. A total of three washes was performed, and the retentate was restored to its former volume by the addition of phosphate buffer. These short fibril segments were stored at 4°C for no longer than 1 week.

## **STEM Sample Preparation**

Samples were prepared at the STEM facility at the Brookhaven National Laboratory. 3 nm carbon substrates were prepared by carbon arc evaporation onto freshly cleaved, single crystal rock salt, floated onto a water surface, and picked up from above by touching a 2.3 mm titanium grid covered with holey film, retaining a drop of water. First, 2 µl of 100 µg/ml tobacco mosaic virus (TMV) were injected into a droplet of water covering the grids and allowed to adhere for 1 minute. After four washings, 2 µl of fibrils were injected into the droplet and allowed to adhere for 1 minute. The grid was then washed 10 times with water, pinched between two pieces of filter paper and then immediately plunged into liquid nitrogen slush. Finally, the grid was then transferred to an ion-pumped freeze dryer, freeze-dried overnight by gradually warming to -80 °C, and transferred under vacuum to the STEM.

## **STEM Data Processing**

Measurements from the STEM dark-field images of unstained samples were made with the program PCMass30 (Wall and Simon, 2001; Diaz-Avalos et al., 2005). The program subtracts the background from the images automatically and provides a measurement of electron scattering proportional to the mass inside a box. Unencumbered segments of TMV were

measured using a modeled 6 nm rod (Model 24: boxes 160 Å x 400 Å), and segments of K19 fibrils were measured using a modeled PHF (Model 59: box size 400 Å x 400 Å).

### **Statistical Modeling of MPL Measurements**

The data (n = 548) were modeled as a three component Gaussian mixture, using the  
Statistic                      Online                      Computational                      Resource                      Modeler  
([http://www.socr.ucla.edu/htmls/SOCR\\_Modeler.html](http://www.socr.ucla.edu/htmls/SOCR_Modeler.html)).

### **Preparation of peptide-gold conjugates**

Peptide–Nanogold conjugates were prepared as described earlier for similarly sized peptides (Schmidt et al., 1999). Briefly, 60 nanomoles of the peptides CGGG-(D)-TLKIVW and CGGG-(D)-LKTWIV (CS Bio) were dissolved in 110 µl of phosphate-buffered saline (20 mM, pH 6.5, 0.15 M NaCl), added to 6 nanomoles of Monomaleimido Nanogold (Nanoprobes), dissolved in 200 µl H<sub>2</sub>O and incubated for 1 hour at room temperature (22 °C) with constant rotation. Peptide–Nanogold conjugates were separated from excess unbound peptides by membrane centrifugation (Microcon-10 system, Amicon) using a molecular mass cut-off of 10 kDa. Peptide–Nanogold conjugates were then diluted into phosphate-buffered saline, aliquoted and stored at –20° C for no longer than one month.

### **Preparation of samples for Nanogold binding experiments**

Nanogold conjugated inhibitor (or control) (10 nM) was incubated with 1.67  $\mu$ M K19 fibrils (by monomer) in MOPS buffer (25 mM, pH 7.2) for 1 hour. We applied 5  $\mu$ l of it to a glow-discharged, 400-mesh carbon-stabilized copper grid (Ted Pella) for 3 minutes. The grids were washed twice with H<sub>2</sub>O and 10  $\mu$ l of the Goldenhance reagent was applied for 10 seconds. The grids were washed five times with H<sub>2</sub>O and negatively stained with 2% uranyl acetate.

Alzheimer's disease  
Amyotrophic lateral sclerosis/parkinsonism-dementia complex  
Argyrophilic grain disease  
Chronic traumatic encephalopathy  
Corticobasal degeneration  
Diffuse neurofibrillary tangles with calcification  
Down's syndrome  
Familial British dementia  
Familial Danish dementia  
Frontotemporal dementia and parkinsonism linked to chromosome 17 caused by *MAPT* mutations  
Gerstmann–Sträussler–Scheinker disease  
Guadeloupean parkinsonism  
Myotonic dystrophy  
Niemann–Pick disease, type C  
Non-Guamanian motor neuron disease with neurofibrillary tangles  
Pantothenate kinase-associated neurodegeneration  
Pick's disease  
Postencephalitic parkinsonism  
Prion protein cerebral amyloid angiopathy  
Progressive subcortical gliosis  
Progressive supranuclear palsy  
SLC9A6-related mental retardation  
Subacute sclerosing panencephalitis  
Tangle-only dementia  
White matter tauopathy with globular glial inclusions

**Table 3.1: Diseases associated with tau aggregation**

(List adapted from Goedert and Spillantini, 2011)

|     |                   |                   |                   |
|-----|-------------------|-------------------|-------------------|
| 1   | MAEPRQEFEV        | MEDHAGTYGL        | GDRKDQGGYT        |
| 31  | MHQDQEGDTD        | AGLKESPLQT        | PTEDGSEEPG        |
| 61  | SETSDAKSTP        | TAEDVTAPLV        | DEGAPGKQAA        |
| 91  | AQPHTEIPEG        | TTAEEAGIGD        | TPSLEDEAAG        |
| 121 | HVTQARMVSK        | SKDGTGSDDK        | KAKGADGKTK        |
| 151 | IATPRGAAPP        | GQKGQANATR        | IPAKTPPAPK        |
| 181 | TPPSSGEPPK        | SGDRSGYSSP        | GSPGTPGSRS        |
| 211 | RTPSLPTPPT        | REPKKVAVVR        | TPPKSPSSAK        |
| 241 | <u>SRLQTAPVPM</u> | <u>PDLKNVSKI</u>  | <u>GSTENLKHQP</u> |
| 271 | <u>GGGKVQIINK</u> | <u>KLDLSNVQSK</u> | <u>CGSKDNIKHV</u> |
| 301 | <u>PGGGSVQIVY</u> | <u>KPVDLSKVTS</u> | <u>KCGSLGNIHH</u> |
| 331 | <u>KPGGGQVEVK</u> | <u>SEKLDFKDRV</u> | <u>QSKIGSLDNI</u> |
| 361 | <u>THVPGGGNKK</u> | IETHKLTFRE        | NAKAKTDHGA        |
| 391 | EIVYKSPVVS        | GDTSPRHLSN        | VSSTGSIDMV        |
| 421 | DSPQLATLAD        | EVSASLAKQG        | L                 |

**Figure 3.1: The complete amino acid sequence of full length human tau (htau40).** The microtubule binding regions are underlined.

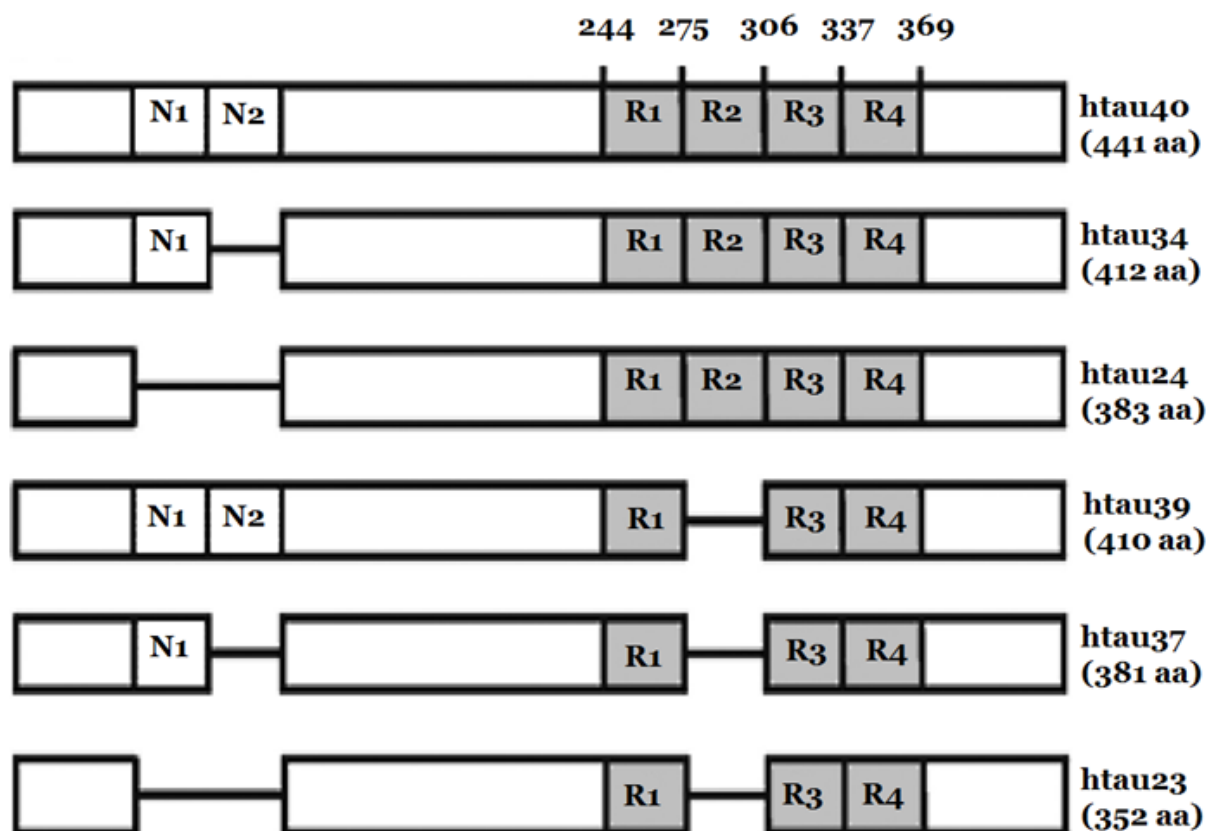


**Figure 3.2: Domain architecture of human tau isoforms.** Tau isoforms are differentiated by the inclusion or exclusion of two inserts near the N-terminus (N1 and N2), and the inclusion or exclusion of R2, the second microtubule binding pseudorepeat near the C-terminus. Isoforms range from 352 to 441 residues long, as indicated to the right.



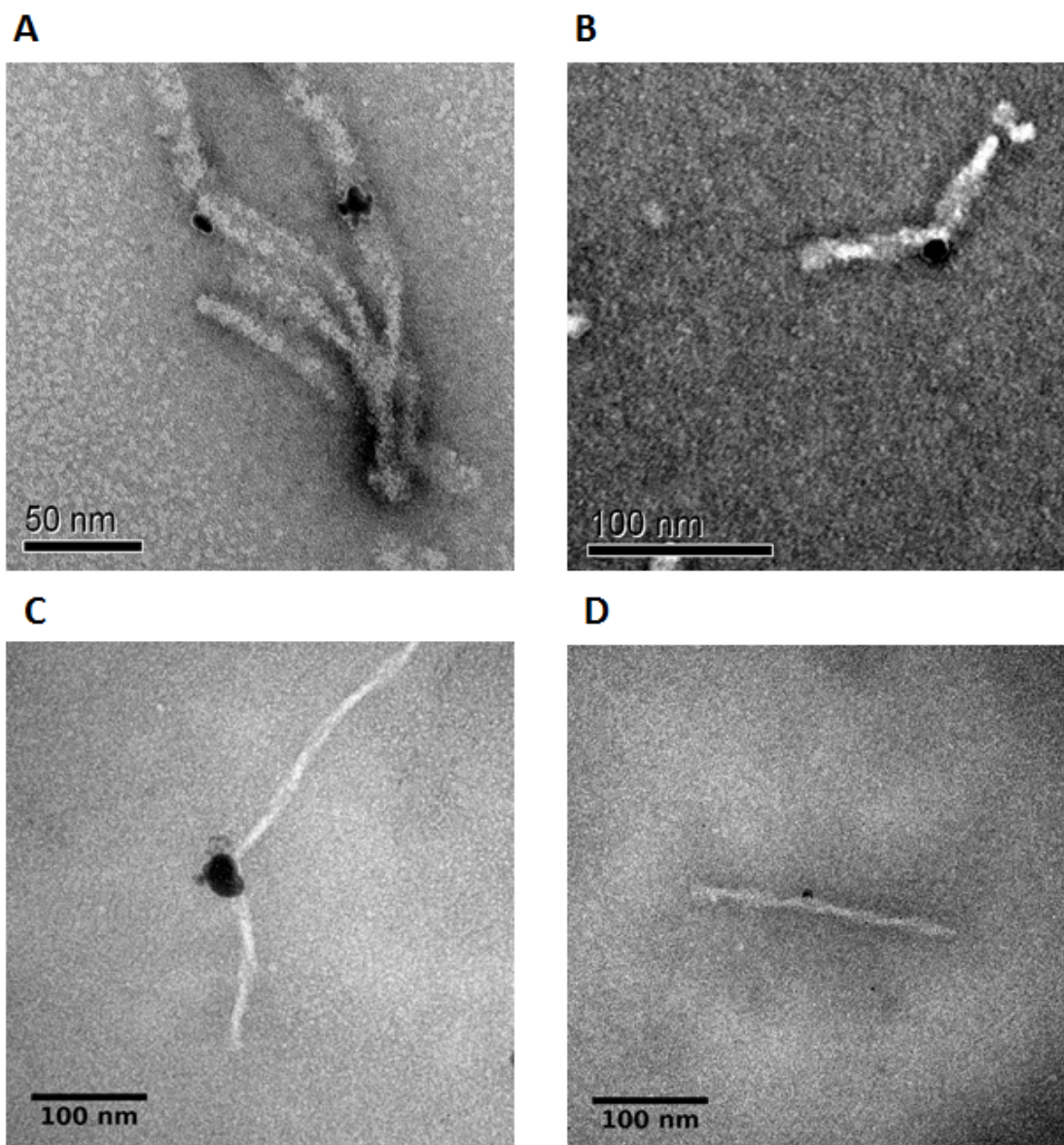


**Figure 3.3: Negatively stained transmission electron micrographs of Nanogold-labeled inhibitor apparently bound along the side of K19 fibrils.** 10 nM of conjugated inhibitor was incubated with 1.67  $\mu\text{M}$  (by monomer) of K19 fibrils for 1 hour at room temperature prior to EM grid preparation. Goldenhance reagent was used to facilitate visualization of the Nanogold particle. Scale bar for (a) is 50 nm; all others are 100 nm.

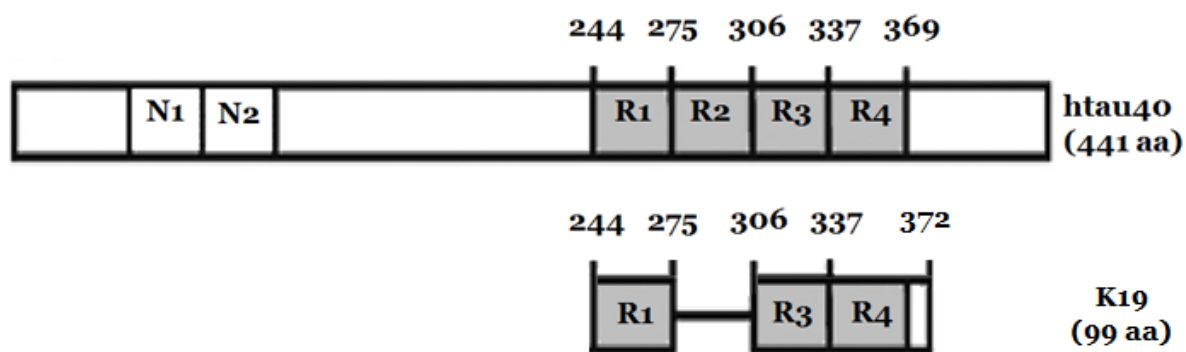


**Figure 3.4: Bar diagrams of full length tau and K19.** Htau40 is the longest isoform in the human CNS (441 residues). Construct K19 comprises microtubule binding domains R1, R3, and R4 (99 residues).

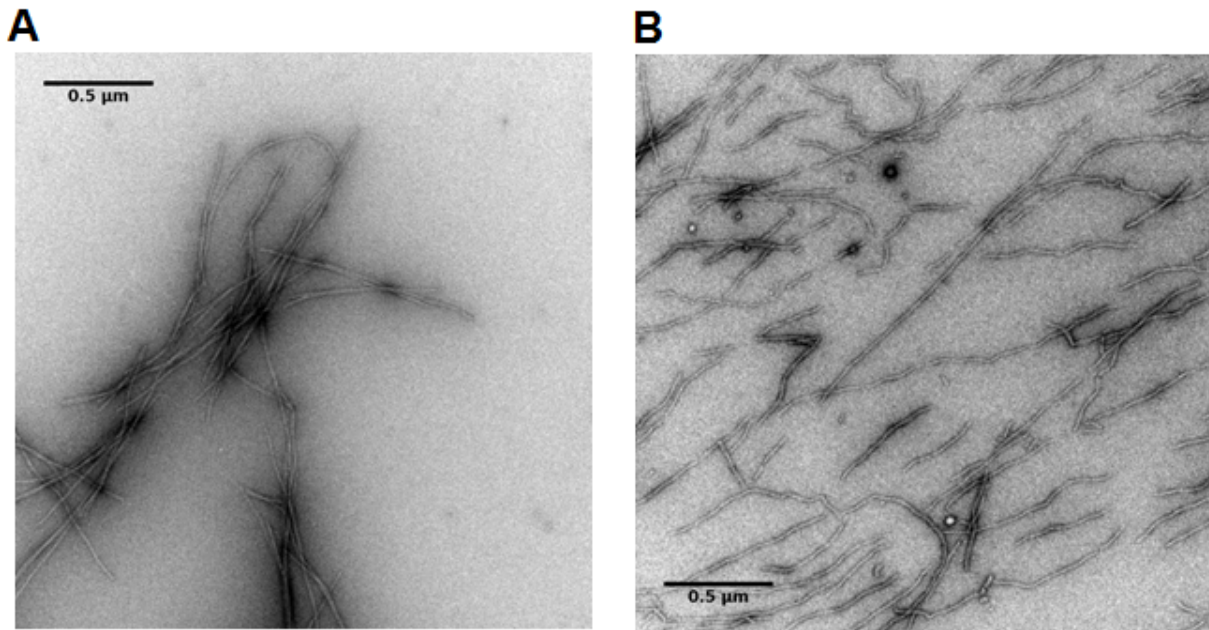


**Figure 3.5: Transmission electron micrographs of K19 fibrils.** Fibrils were formed by 100  $\mu\text{M}$  of soluble K19 with 25  $\mu\text{M}$  heparin for 48h at 37°C in 50 mM phosphate buffer, pH 7.4. Samples were negatively stained with 2% uranyl acetate. Scale bars represent 500 nm for both (A) and (B).

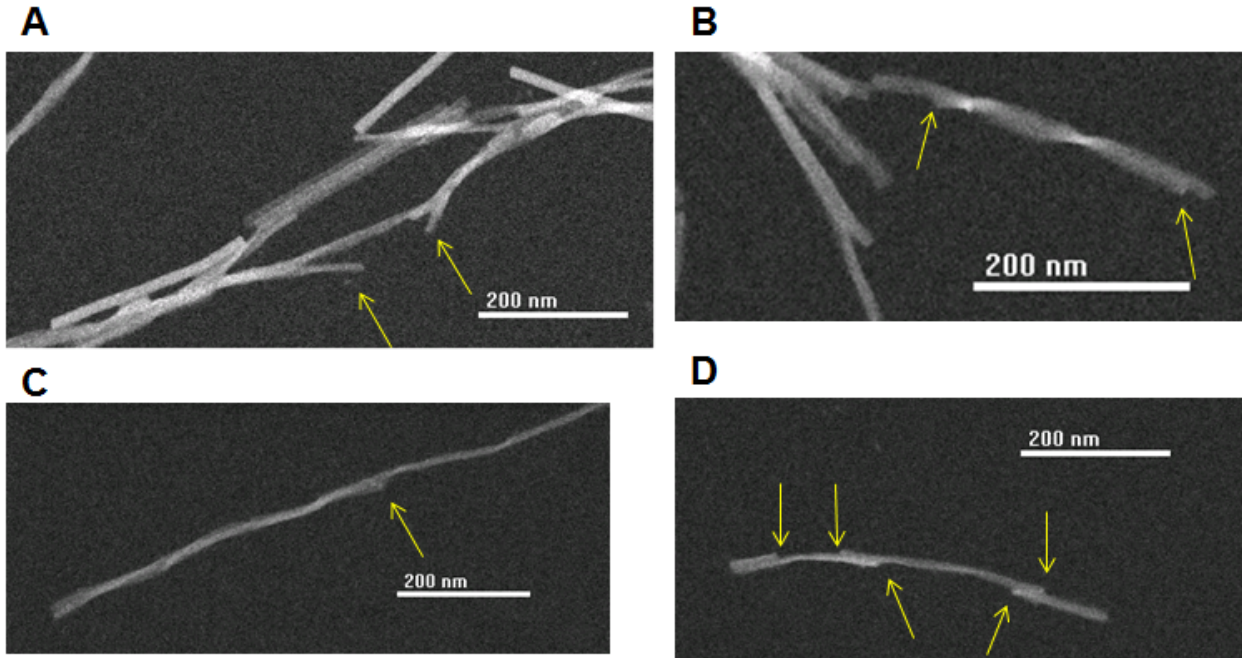


**Figure 3.6: Scanning transmission electron micrographs of K19 fibrils.** Fibrils were formed by 100  $\mu\text{M}$  of soluble K19 with 25  $\mu\text{M}$  heparin for 48h at 37°C in 50 mM phosphate buffer, pH 7.4. Yellow arrows indicate where fibril overhangs are present. Images were recorded from unstained samples of K19. Scale bars in all images represent 200 nm.

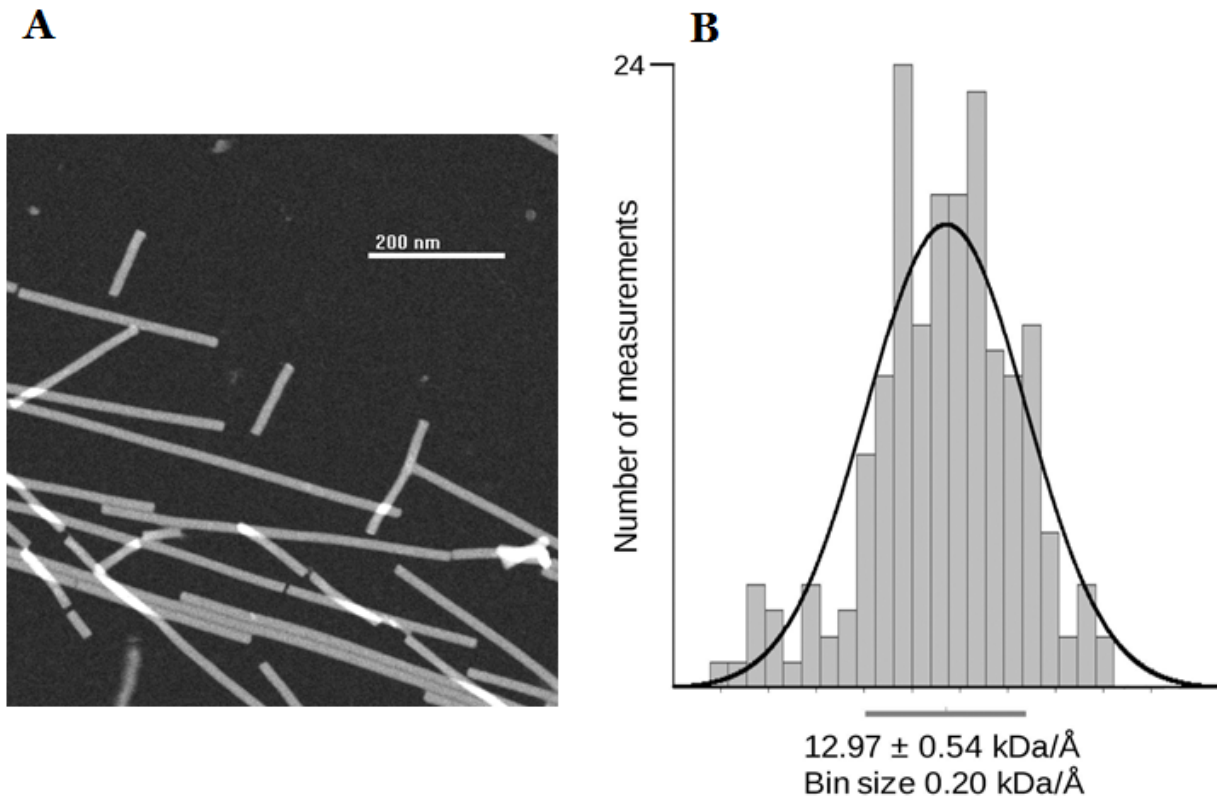


**Figure 3.7: Validation of the correction factor used to determine MPL values of K19 fibrils.** The correction factor was calculated using half ( $n = 191$ ) of the MPL values measured for the standard tobacco mosaic virus (TMV) particles, depicted in (a). In order to validate the applicability of this scaling factor, it was applied to the remaining half of TMV MPL values, yielding a normal distribution centered at  $12.97 \pm 0.54$  kDa/Å (b). This value corresponds well with the known mass of the standard, 13.10 kDa/Å.

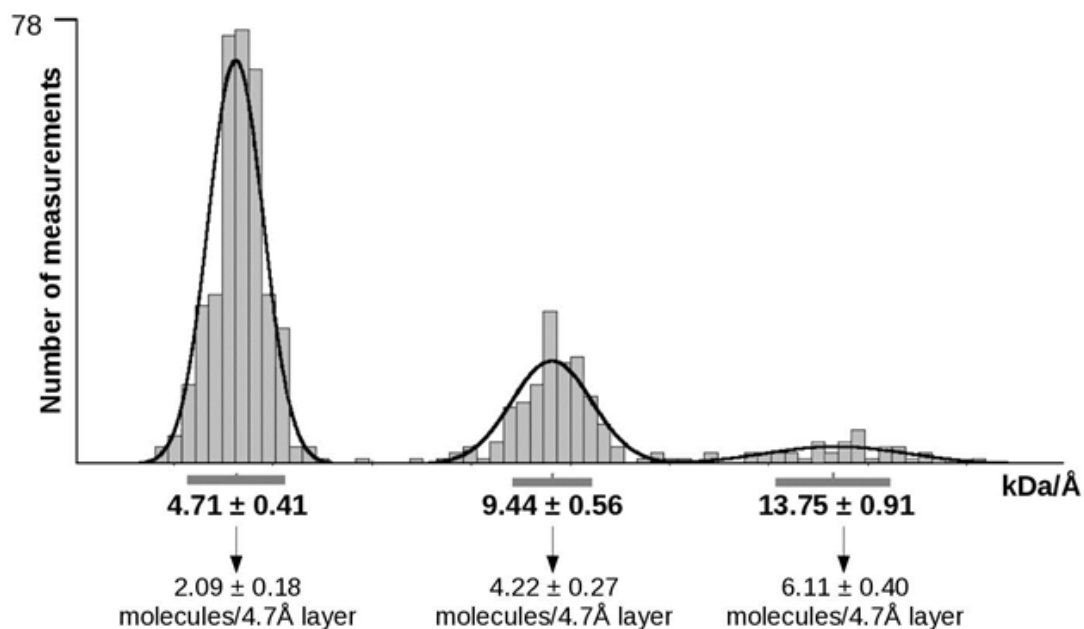


**Figure 3.8: MPL Measurements of K19 fibrils as determined by STEM.** MPL measurements for K19 were modeled as three Gaussian distributions. The most highly represented group comprised a mean MPL of  $4.71 \pm 0.41$  kDa/Å, corresponding well with the calculated value of 4.5 kDa/Å predicted for the steric zipper model, which contains two molecules of K19 per 4.7 Å cross beta layer. Thicker fibrils clustered into distributions corresponding to fibrils with four and six molecules of K19 per 4.7 Å cross beta layer. A binning window of 0.40 kDa/Å was used to produce the histogram.

## References

Arriagada, P. V., Growdon, J. H., Hedley-Whyte, E. T., and Hyman, B. T. (1992). Neurofibrillary tangles but not senile plaques parallel duration and severity of Alzheimer's disease. *Neurology*. *42*, 631-699.

Bandyopadhyay, B., Li, G., Yin, H., and Kuret, J. (2007). Tau aggregation and toxicity in a cell culture model of tauopathy. *The Journal of Biological Chemistry*. *282*, 16454-16464.

Barghorn, S., Davies, P., and Mandelkow, E. (2004). Tau paired helical filaments from Alzheimer's disease brain and assembled in vitro are based on beta-structure in the core domain. *Biochemistry*. *43*, 1694-1703.

Barghorn, S., Biernat, J., and Mandelkow, E. (2005). Purification of recombinant tau protein and preparation of Alzheimer-paired helical filaments in vitro. *Methods Mol. Biol.* *299*, 35-51.

Biernat, J., Mandelkow, E. M., Schröter, C., Lichtenberg-Kraag, B., Steiner, B., Berling, B., Meyer, H., Mercken, M., Vandermeeren, A., and Goedert, M. (1992). The switch of tau protein to an Alzheimer-like state includes the phosphorylation of two serine-proline motifs upstream of the microtubule binding region. *EMBO J.* *11*, 1593-1597.

Berriman, J., Serpell, L. C., Oberg, K. A., Fink, A. L., Goedert, M., and Crowther, R. A. (2003). Tau filaments from human brain and from in vitro assembly of recombinant protein show cross-beta structure. *Proceedings of the National Academy of Sciences, USA*. *100*, 9034-9038.

Blanco, L. P., Evans, M. L., Smith, D. R., Badtke, M. P., and Chapman, M. R. (2012). Diversity, biogenesis and function of microbial amyloids. *Trends in Microbiology*. *20*, 66-73.

Braak, F., Braak, H., and Mandelkow, E. M. (1994). A sequence of cytoskeleton changes related to the formation of neurofibrillary tangles and neuropil threads. *Acta Neuropathologica*. *87*, 554-567.

Butner, K. A., and Kirschner, M. W. (1991). Tau protein binds to microtubules through a flexible array of distributed weak sites. *The Journal of Cell Biology*. *115*, 717-730.

Cassimeris, L., and Spittle, C. (2001). Regulation of microtubule-associated proteins. *International Review of Cytology*. *210*, 163-226.

Cleveland, D. W., Hwo, S. Y., & Kirschner, M. W. (1977). Physical and chemical properties of purified tau factor and the role of tau in microtubule assembly. *Journal of Molecular Biology*. *116*, 227-247.

Daebel, V., Chinnathambi, S., Biernat, J., Schwalbe, M., Habenstein, B., Loquet, A., Akoury, E., Tepper, K., Müller, H., Baldus, M., Griesinger, C., Zweckstetter, M., Mandelkow, E., Vijayan, V., and Lange, A. (2012). Beta-sheet core of tau paired helical filaments revealed by solid-state NMR. *Journal of the American Chemical Society*. *134*, 13982-13989.

Diaz-Avalos, R., King, C. Y., Wall, J., Simon, M., and Caspar, D. L. (2005). Strain-specific morphologies of yeast prion amyloid fibrils. *Proceedings of the National Academy of Sciences, USA*. *102*, 10165-10170.

Drubin, D. G., and Kirschner, M. W. (1986). Tau protein function in living cells. *The Journal of Cell Biology*. *103*, 2739-2746.

Eisenberg, D., and Jucker, M. (2012). The amyloid state of proteins in human diseases. *Cell*. *148*, 1188-1203.



Fowler, D. M., and Kelly, J. W. (2012). Functional amyloidogenesis and cytotoxicity-insights into biology and pathology. *PLoS Biology*. *10*, e1001459.

Garcia, M. L., and Cleveland, D. W. (2001). Going new places using an old MAP: Tau, microtubules and human neurodegenerative disease. *Current Opinion in Cell Biology*. *13*, 41-48.

Goedert, M., Spillantini, M. G., Cairns, N. J., and Crowther, R. A. (1992). Tau proteins of Alzheimer paired helical filaments: abnormal phosphorylation of all six brain isoforms. *Neuron*. *8*, 159–168.

Goedert, M., Jakes, R., Spillantini, M. G., Hasegawa, M., Smith, M. J., and Crowther, R. A. (1996). Assembly of microtubule-associated protein tau into Alzheimer-like filaments induced by sulphated glycosaminoglycans. *Nature*. *383*, 550-553.

Goedert, M., and Spillantini, M. G. (2011). Pathogenesis of the tauopathies. *Journal of Molecular Neuroscience*. *45*, 425-431.

Goode, B. L., and Feinstein, S. C. (1994). Identification of a novel microtubule binding and assembly domain in the developmentally regulated inter-repeat region of tau. *The Journal of Cell Biology*. *124*, 769-782.

Goux, W. J., Kopplin, L., Nguyen, A. D., Leak, K., Rutkofsky, M., Shanmuganandam, V. D., Sharma, D., Inouye, H., and Kirschner, D. A. (2004). The formation of straight and twisted filaments from short tau peptides. *Journal of Biological Chemistry*. *279*, 26868–26875.

Grundke-Iqbal, I., Iqbal, K., Tung, Y. C., Quinlan, M., Wisniewski, H. M., and Binder, L. I. (1986) Abnormal phosphorylation of the microtubule-associated protein tau in Alzheimer cytoskeletal pathology. *Proceedings of the National Academy of Sciences, USA*. *83*, 4913–4917.

Halliday, G., Bigio, E. H., Cairns, N. J., Neumann, M., Mackenzie, I. R., and Mann, D. M. (2012). Mechanism of disease in frontotemporal lobar degeneration: gain of function versus loss of function effects. *124*, 372-382.

Hasegawa, M., Smith, M. J., and Goedert, M. (1998). Tau proteins with FTDP-17 mutations have a reduced ability to promote microtubule assembly. *FEBS Letters*. *437*, 207-210.

Inouye, H., Sharma, D., Goux, W. J., and Kirschner, D. A. (2006). Structure of core domain of fibril-forming PHF/Tau fragments. *Biophysical Journal*. *90*, 1774-1789.

Ivanova, M.I., Sievers, S.A., Sawaya, M.R., Wall, J.S., and Eisenberg, D. (2009). Molecular basis for insulin fibril assembly. *Nature*. *106*, 18990-189955.

Jeganathan, S., von Bergen, M., Mandelkow, E. M., and Mandelkow, E. (2008). The natively unfolded character of tau and its aggregation to alzheimer-like paired helical filaments. *Biochemistry*. *47*, 10526-10539.

Kampers, T., Friedhoff, P., Biernat, J., Mandelkow, E. M., and Mandelkow E. (1996). RNA stimulates aggregation of microtubule-associated protein tau into Alzheimer-like paired helical filaments. *FEBS Letters*. *399*, 344-349.

Kirschner, D. A., Abraham, C., and Selkoe, D. J. (1986). X-ray diffraction from intraneuronal paired helical filaments and extraneuronal amyloid fibers in Alzheimer disease indicates cross-beta conformation. *Proceedings of the National Academy of Sciences, USA*. *83*, 503-507.

Kondo, J., Honda, T., Mori., Hamada, Y., Miura, R., Ogawara, M., and Ihara, Y. (1988). The carboxyl third of tau is tightly bound to paired helical filaments. *Neuron*. *1*, 827-834.

Kyte, J., and Doolittle, R. F. (1982). A simple method for displaying the hydropathic character of a protein. *Journal of Molecular Biology*. *157*, 105-132.

Lee, G., Neve, R. L., and Kosik, K. S. (1989) The microtubule-binding domain of tau protein. *Neuron*. *2*, 1615–1624.

Makrides, V., Shen, T. E., Bhatia, R., Smith, B. L., Thimm, J., Lal, R., and Feinstein, S. C. (2003). Microtubule-dependent oligomerization of tau. Implications for physiological tau function and tauopathies. *Journal of Biological Chemistry*. *278*, 33298-33304.

Nelson, R., Sawaya, M. R., Balbirnie, M., Madsen, A. Ø, Riek, C., Grothe, R., and Eisenberg, D. (2005). Structure of the cross-beta spine of amyloid-like fibrils. *Nature*. *435*, 773-778.

Olmsted, J. B., and Borisy, G. G. (1973). Microtubules. *Annual Review of Biochemistry*. *42*, 507-540.

Olmsted, J. (1986). Microtubule-associated proteins. *Annual Review of Cell Biology*. *2*, 421-457.

Sadqi, M., Hernández, F., Pan, U., Pérez, M., Schaeberle, M. D., Avila, J., and Muñoz, V. (2002). Alpha-helix structure in Alzheimer's disease aggregates of tau-protein. *Biochemistry*. *41*, 7150-7155.

Schmidt, K., Segond von Banchet, G., and Heppelmann, B. (1999). Labelling of peptides with 1.4-nm gold particles to demonstrate their binding sites in the rat spinal cord. *Journal of Neuroscience Methods*. *87*, 195–200.

Schmitt, F. O. (1968). Fibrous proteins--neuronal organelles. *Proceedings of the National Academy of Sciences, USA*. *60*, 1092-1101.

Schweers, O., Schönbrunn-Hanebeck, E., Marx, A., and Mandelkow, E. (1994). Structural studies of tau protein and alzheimer paired helical filaments show no evidence for beta-structure. *Journal of Biological Chemistry*. *269*, 24290-24297.

Sievers, S. A., Karanicolas, J., Chang, H. W., Zhao, A., Jiang, L., Zirafi, O., Stevens, J. T., Münch, J., Baker, D., and Eisenberg, D. (2011). Structure-based design of non-natural amino-acid inhibitors of amyloid fibril formation. *Nature*. *475*, 96-100.

Sipe, J. D., Benson, M. D., Buxbaum, J. N., Ikeda, S., Merlini, G., Saraiva, M. J., and Westermarck P. (2012). Amyloid fibril protein nomenclature: 2012 recommendations from the Nomenclature Committee of the International Society of Amyloidosis. *Amyloid*. *19*, 167-170.

Sousa, A. A., and Leapman, R. D. (2007). Quantitative STEM mass measurement of biological macromolecules in a 300 kV TEM. *Journal of Microscopy*. *228*, 25-33.

Spiess, E., Zimmerman, H., and Lunsdorf, H. (1987). *Electron Microscopy in Molecular Biology*. IRL Press.

Stromer, T., and Serpell, L. C. (2005). Structure and morphology of the Alzheimer's amyloid fibrils. *Microscopy Research and Technique*. *67*, 210-217.

Studier, F. W., Rosenberg, A. H., Dunn, J. J. & Dubendorff, J. W. (1990). Use of T7 RNA polymerase to direct expression of cloned genes. *Methods in Enzymology*. *185*, 60–89.

von Bergen, M., Barghorn, S., Müller, S. A., Pickhardt, M., Biernat, J., Mandelkow, E. M., Davies, P., Aebi, U., and Mandelkow, E. (2006). The core of tau-paired helical filaments studied by scanning transmission electron microscopy and limited proteolysis. *Biochemistry*. *45*, 6446-57.

Wall, J. S., and Hainfeld, J. F. (1986). Mass mapping with the scanning transmission electron microscope. *Annual Review of Biophysics and Biophysical Chemistry*. *15*, 355-376.

Wall, J. S., and Simon, M. N. (2001). Scanning transmission electron microscopy of DNA-protein complexes. *Methods in Molecular Biology*. *148*, 589-601.

Weingarten, M. D., Lockwood, A. H., Hwo, S. Y., and Kirschner, M. W. (1975). A protein factor essential for microtubule assembly. *Proceedings of the National Academy of Sciences, USA*. *72*, 1858-1862.

Wegmann S., Medalsy, I. D., Mandelkow, E., and Müller, D. J. (2012). The fuzzy coat of pathological human tau fibrils is a two-layered polyelectrolyte brush. *Proceedings of the National Academy of Sciences, USA*. *110*, E313-E321.

Wille, H., Drewes, G., Biernat, J., Mandelkow, E. M., and Mandelkow, E. (1992). Alzheimer-like paired helical filaments and antiparallel dimers formed from microtubule-associated protein tau in vitro. *Journal of Cell Biology*. *118*, 573-584.

Wilson, D. M., and Binder, L. I. (1997). Free fatty acids stimulate the polymerization of tau and amyloid beta peptides. In vitro evidence for a common effector of pathogenesis in Alzheimer's disease. *American Journal of Pathology*. *150*, 2181-2195.

Wischik, C. M., Novak, M., Thøgersen, H. C., Edwards, P. C., Runswick, M. J., Jakes, R., Walker, J. E., Milstein, C., Roth, M., and Klug, A. (1988a). Isolation of a fragment of tau derived from the core of the paired helical filament of Alzheimer disease. *Proceedings of the National Academy of Sciences, USA*. *85*, 4506-4510.

Wischik, C. M., Novak, M., Edwards, P. C., Klug, A., Tichelaar, W., Crowther, R. A. (1988b). Structural characterization of the core of the paired helical filament of Alzheimer disease. *Proceedings of the National Academy of Sciences. USA.* *85*, 4884-4888.

Witman, G. B., Cleveland, D. W., Weingarten, M. D., and Kirschner, M. W. (1976). Tubulin requires tau for growth onto microtubule initiating sites. *Proceedings of the National Academy of Sciences, USA.* *73*, 4070-4074.

von Bergen, M., Friedhoff, P., Biernat, J., Heberle, J., Mandelkow, E. M., and Mandelkow, E. (2000) Assembly of tau protein into Alzheimer paired helical filaments depends on a local sequence motif (306VQIVYK311) forming beta structure. *Proceedings of the National Academy of Sciences. USA.* *97*, 5129–5134.

von Bergen, M., Barghorn, S., Müller, S. A., Pickhardt, M., Biernat, J., Mandelkow, E. M., Davies, P., Aebi, U., and Mandelkow, E. (2006). The core of tau-paired helical filaments studied by scanning transmission electron microscopy and limited proteolysis. *Biochemistry.* *45*, 6446-6457.

## Chapter 4: Development of a High-throughput Screening Assay for Disaggregants of Steric Zippers

### **Abstract**

Insoluble tau fibrils represent a defining pathological feature of tauopathies. Although the precise cytotoxic mechanism remains undefined, the unambiguous association between neurodegeneration and these insoluble protein deposits merits an investigation into disaggregation as a potential therapeutic strategy. In the present chapter, I address this challenge by developing a high-throughput screen to identify small molecules that dissolve pre-formed tau fibrils. By utilizing the structural features of the steric zipper core, and combining them with a FRET-based aggregation-monitoring system, I designed an assay to screen for tau disaggregants. A pilot screen of over 3500 compounds against peptidic tau fibrils yielded no effective disaggregants. However, with additional modifications, this method could still prove to be a viable way to screen for anti-aggregation compounds.

# Introduction

## Disaggregation of amyloid

Dozens of proteins have been found to form amyloid fibrils-highly ordered aggregates frequently associated with disease. In these illnesses, the appearance of insoluble deposits formed by specific protein(s) correlates with one or more pathologies (Westermarck et al., 2007). For example, patients of type II diabetes typically have deposits of islet amyloid polypeptide in the pancreas, and patients of the neurodegenerative ailment Alzheimer's disease (AD) present aggregates of A $\beta$  peptide and tau protein in the brain. Although the specific mechanism of cytotoxicity remains unclear in these diseases, the unequivocal association between aggregation and pathology compels the research community to explore disaggregation as a therapeutic strategy. Aggregation of tau protein specifically is associated not only with AD, but with an entire class of neurodegenerative diseases referred to as tauopathies, including Pick's disease, frontotemporal dementia linked to chromosome 17 (FTDP-17), and corticobasal degeneration (Hernández and Avila, 2007). More recently, tau inclusions have also been found in the brains of retired contact-sports athletes that exhibit cognitive and mood symptoms (Small et al., 2013).

In any therapeutic strategy against amyloid, it is also of paramount importance to identify effective agents against specific amyloid proteins, due to the recent discovery of functional amyloid (Fowler et al., 2007). We and others have collectively identified at least two dozen functional amyloids (Fowler et al., 2006; Maji et al., 2009; Si et al., 2010). For example, Pmel17 amyloid is critical to melanin production, and CPEB amyloid serves to maintain long-term learning related changes in synaptic morphology and function (Heinrich and Lindquist, 2011). Non-specific amyloid disaggregation is therefore not a prudent therapeutic strategy. One



study has shown that eliminating specific amyloid aggregates is possible, although some oligomers persisted in their experiments (Wang et al., 2008).

The field is yet to definitively conclude whether aggregates of A $\beta$  or tau protein initiates the disease cascade (Ittner and Götz, 2011). Besides the need to avoid adversely affecting physiologically necessary amyloid species, developing a disaggregant specific to tau would help resolve this debate, which has eluded consensus for decades.

### **Previously identified tau disaggregating agents**

To date, two published studies have reported small molecules capable of disaggregating tau fibrils. In one, anthroquinones were identified as an entire class of compounds with this activity (Pickhardt et al., 2005). However, their electron micrographs show that the disaggregants resulted in a remodeling of the deposits, rather than altogether dissolution. This likely stems from the authors' choice to employ the reporter dye thioflavin S (Levine, 1993) to monitor the aggregation state of their tau construct. This dye only reliably qualitatively indicates the presence or absence of fibrils, but not the non-fibrillar aggregates that remained. These breakdown products might represent the oligomers emerging as the toxic species in protein aggregation diseases (Glabe, 2008).

In other work, researchers discovered C11, a cyanine dye that reduces but does not eliminate fibril load in isolated tau transgenic mouse tissue (Duff et al., 2010). Of particular concern, however, was the observation that higher doses of C11 had the opposite effect, increasing tau aggregation. In both studies cited, no conditions completely eliminated existing tau aggregates.

## **VQIVYK as a model system for to screen for a tau disaggregants**

Structurally characterizing human tau protein is fraught with technical difficulty. Not only is tau relatively large, comprising 441 amino acids, but it is intrinsically disordered in solution (Mukrash et al., 2009). Previous work identified the six amino acid segment <sup>306</sup>VQIVYK<sup>311</sup> to be the driving force behind the aggregation of tau protein (von Bergen et al., 2000). Proline-scanning mutations in this region suppress aggregation. Our own lab built upon these findings by determining the crystal structure of the VQIVYK segment, which revealed a fiber-like dual beta-sheet along the entire length of the crystals (Sawaya et al., 2007). This structure, and others like it from other amyloid-forming proteins, elucidates the structural basis for the unusual stability of amyloid: a double  $\beta$ -sheet with an interface devoid of water, termed a steric zipper (Nelson et al., 2005). Using our structure of VQIVYK as a target, we developed a computational method to design a peptide that inhibits VQIVYK fibril formation. This inhibiting peptide, composed of non-natural amino acids, prevents amyloid formation of both VQIVYK and protein constructs of tau. These studies demonstrate that these peptide fibrils serve as effective surrogates for the investigation of tau protein fibrils (Sievers et al., 2011).

## **Current methods for monitoring amyloid aggregation**

Small molecules that bind amyloid, such as the aforementioned thioflavin family of compounds and Congo red, have come to be essential tools in studying amyloid aggregation (Kelényi, 1967). In the last decade, many other molecular probes have been developed to detect amyloid fibrils as well (Table 4.1). Still, thioflavin T and its derivatives remain the most

commonly used probe in screens for inhibitors of amyloid aggregation, since its fluorescence increases dramatically in the presence of amyloid. However, using thioflavin T leaves much to be desired, since much about its mechanism, such as the precise binding site (Levine, 2005), stoichiometry (Groenning et al., 2007), quantum yield (Lindgren et al., 2005), and affinity (Cisek and Kuret, 2012), remains ambiguous.

More globally, different polymorphs of the same protein can bind different small molecules, further complicating the assumptions one can make regarding the consequences of such binding. This was demonstrated in the only report to date that shows atomic-level structures of amyloid bound to small molecules (Landau et al., 2012). In three different co-crystal structures, <sup>306</sup>VQIVYK<sup>311</sup> was shown to bind the small molecules DDNP, orange-G, or curcumin, with different steric zipper polymorphs accommodating different compounds. It is thus clear that relying on small molecules to monitor amyloid aggregation is fraught with uncertainty.

### **FRET allows for direct monitoring of steric zipper formation**

Förster resonance energy transfer (FRET) is a sensitive way to determine whether two fluorophores are within a specific distance, termed the Förster distance (Joo et al., 2008). Several studies have incorporated FRET to probe the conformational changes in amyloid proteins as they aggregate (Onuki et al., 2002; Kaylor et al., 2005; Deng et al., 2007; Deng et al., 2008), but none has converted this method into a high throughput assay.

For the present work, we opted to utilize an approach pioneered by the Lai group (Deng et al., 2008), covalently linking the FRET pair, dansyl ( $E_{X_{Max}}/E_{M_{Max}} \approx 340/480$  nm) and

tryptophan ( $E_{x_{\text{Max}}}/E_{m_{\text{Max}}} \approx 280/340$  nm), to the N and C termini of VQIVYK, respectively. Henceforth referred to as DV7W, the fluorescent behavior of this modified tau segment depends upon its aggregation state. When excited by 280 nm light, monomeric DV7W fluoresces with  $I_{\text{max}} \sim 340$  nm. However, in the aggregated state, the same incident light results in a markedly different emission spectrum, with  $I_{\text{max}} \sim 480$  nm (**Figure 4.3**). The spectral change shows that the tryptophan and dansyl group are within their 21 Å Förster distance, a spatial arrangement predicted by our VQIVYK fibril model. Building upon these observations, we hypothesized that we could devise a screen for small molecule disaggregants that eliminate FRET, leading to a simultaneous decrease in emission at 480 nm and a restoration of emission at 340 nm.

## Results

### Assay Development

In order to demonstrate that monitoring fluorescence at 340 and 480 nm can detect disassembly of FRET-labeled aggregates, we screened several chemicals to be used as a positive control for disaggregation. Among high concentrations of hexafluoroisopropanol (HFIP), dimethylsulfoxide, formic acid, sodium hydroxide, and guanidinium hydrochloride (GdHCl), only 7M GdHCl was found to have a disaggregating effect on the fibrils (**Figure 4.4**).

To validate this method in a format conducive to HTS, we treated 10 uM of DV7W fibrils with GdHCl in phosphate-buffered saline pH 7.4 (PBS), using final volumes of 50  $\mu$ l in 384-well glass-bottom polystyrene plates. To account for residual DMSO from the solvation of small molecules, each sample also contained 1% DMSO to ensure tolerance to DMSO's quenching

effects. Taking top-read fluorescence readings, we observed a highly reproducible dose-dependent response to GdHCl after 24 hours incubation at 37° C (**Figure 4.5**).

The Z-factor has become a common metric to assess the quality and suitability of assays for high-throughput screening (Zhang et al., 1999). It is defined as  $[Z = 1 - ((3\sigma_{c+} + 3\sigma_{c-}) / (|\mu_{c+} - \mu_{c-}|))]$ , where  $\sigma_{c+}$  and  $\sigma_{c-}$  represent the standard deviations of the positive and negative controls, respectively, and  $\mu_{c+}$  and  $\mu_{c-}$  stand for the mean values of the positive and negative controls, respectively. This dimensionless statistic reflects the assay's dynamic range, as well as the inherent data variation. We therefore computed Z-factors for the observed spectroscopic effects, monitoring emission at 340 and 480 nm in response to 280 nm incident light. As a positive control for disaggregation, DV7W fibrils at 10  $\mu$ M concentration were incubated with 7M GdHCl in PBS buffer for 24 hours at 37°C. As a negative control, fibrils were similarly incubated in PBS alone. 1% DMSO was also added to each of the four replicates of each sample. As depicted (**Figure 4.6**), the mean values ( $\pm$  s.d.) of the negative and positive controls measured at 340 nm were 11.8 ( $\pm$  17.7) and 172 ( $\pm$  2.90), respectively. This results in a Z-factor of  $\{1 - ((3(17.7+2.90)) / (|172-11.8|))\} = 0.61$ . At 480 nm, the Z-factor yielded by the data is:  $\{1 - ((3(7.25+10.1)) / (|25.3-205|))\} = 0.71$ . These values exceeded the threshold of 0.5 established by Zhang et al. for an excellent high throughput assay.

### **Small Scale Pilot Screen**

Using the protocol described above, we collaborated with Robert Damoiseaux at the Molecular Screening Shared Resource facility located at the UCLA California NanoSystems Institute, to conduct a pilot screen of 3520 compounds at 10  $\mu$ M final concentration, using small

molecule libraries purchased from Preswick Chemicals and MicroSource. The small molecules were incubated with the 10  $\mu$ M DV7W fibrils for 24 hours at 37° C with constant shaking; the same conditions which allowed our positive control to dissolve the fibril. As a cutoff, we screened for compounds that met or exceeded 50% of the fluorometric effect of the positive control for disaggregation at both 340 and 480 nm. The rationale for monitoring both wavelengths was to exclude small molecules that interfere with the fluorescence readings (i.e. absorbs at 480 nm or fluoresces at 340 nm). However, we did not encounter any compounds that showed evidence of disaggregating activity (**Figure 4.7**).

## Discussion

### **The stability of DV7W aggregates and future directions**

The inability of a diverse library's 3520 small molecules to disaggregate DV7W fibrils re-illustrates the exceptionally high energy barrier to fibril dissolution (Nelson et al., 2005). Although we here and others have shown that peptidic fibrils can be broken apart, either by extreme chemical treatments (Byrne and Angell, 2009), or an enzyme, hsp104(DeSantis et al., 2012), we must consider how these agents are able to do so, and the factors that hinder a small molecule from doing the same.

GdHCl, a widely used chaotrope, decreases the impact of the hydrophobic effect (Breslow and Guo, 1990), significantly reducing the free energy barrier to dissolving aggregates. Combined with the mechanical agitation and elevated temperature in our assay, this explains how 7M GdHCl is able to serve as our disaggregant positive control so effectively. On the other

hand, Hsp104 hydrolyzes ATP, to provide the energy needed to overcome the free energy barrier to disaggregate amyloid. In hindsight, it may have been unrealistic to expect the small molecules we screened to similarly overcome this energy barrier by themselves, especially at equimolar concentrations. Future attempts at identifying disaggregants might be improved by adding concentrations of GdHCl lower than 7M to the peptide fibrils, with the desired effect of slightly destabilizing the fibrils, and decreasing the energy barrier to be overcome for disaggregation by the small molecule. Alternatively, one could also screen with higher concentrations of small molecules, though this carries the risk of the compounds being insoluble in aqueous solutions, or being cytotoxic. Yet another possibility is that the libraries we screened in the pilot study were not sufficiently diverse. Future screens with different libraries could yet yield a natural product disaggregant.

## Materials & Methods

### **Peptide Fibril Formation**

All peptides were purchased from CS Bio (Menlo Park, CA) and confirmed to be >95% pure, confirmed by MALDI-MS. The labeled peptide, with dansyl and tryptophan appended at the N- and C- termini, respectively (DV7W), was dissolved to 4 mM in 20% acetonitrile, with the pH adjusted to 2 by adding concentrated HCl. This peptide solution was then sonicated using 5-second pulses for 8 minutes with a microtip sonicator, then incubated for two days at 37° C, and then 3 weeks at 25° C to form fibrils. The formation of fibrils for both peptides was confirmed with transmission electron microscopy. Pure fibrils, isolated from soluble species, were obtained by centrifuging the mature fibril solutions at 14,000 x g for 30 minutes at 4° C. Then, the

supernatant was removed and the amyloid fibril was washed three times with PBS (137 mM NaCl, 2.7 mM KCl, 10 mM Na<sub>2</sub>HPO<sub>4</sub> • H<sub>2</sub>O, 2 mM KH<sub>2</sub>PO<sub>4</sub>, pH 7.4), and diluted to the desired concentration.

### **FRET Detection of Amyloid Peptide Aggregation**

The SpectraMax M5 fluorometer (Molecular Devices, Inc.) was used to measure the fluorescence intensity of FRET. For 96-well plate assays, black, clear-bottomed plates were used (ThermoFisher Sci. cat#152037) with 150 µl total volume for each sample. The samples were diluted and dispensed into the wells and measured with the exciting wavelength of 280 nm and scan range from 320 nm to 580 nm. During the fluorescence measurement, the concentrations of pure amyloid fibril were controlled to lower than 10 µM by dilution using PBS to reduce the fluorescence quenching. Four replicates of each sample was measured three times in parallel to be averaged. Reagents assayed for disaggregation activity were incubated with DV7W at 37° C for 24 hours, followed by detection via FRET and TEM.

### **High throughput pilot screen**

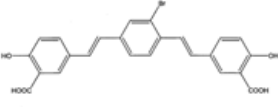
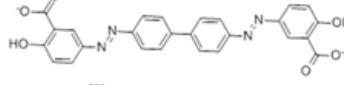
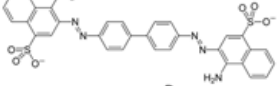
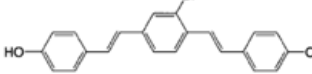
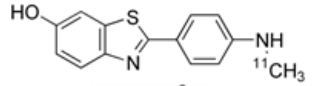
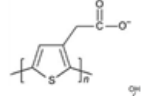
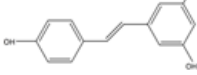
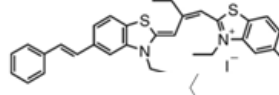
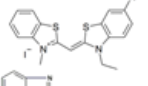
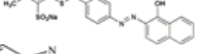
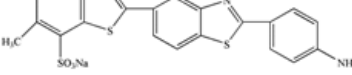
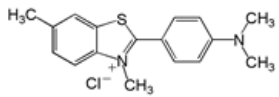
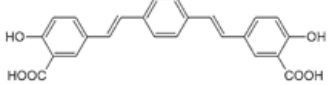
100 and 20 µM stock of DV7W fibrils were prepared as described above. Columns 1 and 2 of each microplate were set aside for internal negative controls, and columns 23 and 24 for internal positive controls. 25 µl of the 20 µM fibril stock was dispensed into columns 1-22 of a 384-well glass bottom microplates (Matrical Inc.), using a Multidrop Combi Reagent Dispenser (Thermo Scientific). Then, 25 µl of 2x PBS was added to each of these wells. Using a repeating



pipette (Eppendorf), 45  $\mu$ l of 7.78 M GdHCl was dispensed into each well of columns 23 and 24, followed by 5  $\mu$ l of 100  $\mu$ M DV7W fibril stock. This gives a final concentration of 7 M GdHCl for the positive controls. To account for DMSO quenching effects, 0.5  $\mu$ l of DMSO was pipetted into each well of columns 1, 2, 23, and 24. Then, using a Biomek FX liquid handler (Beckman Coulter), 0.5  $\mu$ l of 1 mM small molecule stocks was pipetted into each well in columns 3-22, for a final concentration of 10  $\mu$ M of small molecule. Final volumes for each sample was 50  $\mu$ l. Following dispensation, microplates were sealed with polyester adhesive film (Denville Scientific), and incubated at 37° C for 24 hours with shaking at 900 r.p.m. with a diameter of 1 mm. After the incubation, microplates were brought to room temperature, and the adhesive films removed. Then, each microplate was shaken again for 30 seconds immediately before taking fluorescence readings at 340 and 480 nm, using 280 nm incident light.

### **Transmission electron microscopy**

5  $\mu$ l of sample were applied to glow-discharged, 400-mesh carbon-coated, formvar films on copper grids (Ted Pella) for 3 minutes. Grids were rinsed twice with distilled water and stained with 1% uranyl acetate for 60-75 seconds. Grids were then examined using a JEOL JEM1200-EX operating at 80 kEV.

| Probe                 | Chemical structure  | Reference            |
|-----------------------|---|----------------------|
| BSB                   |    | Schmidt et al., 2001 |
| Chrysamine-G          |    | Klunk et al., 1994   |
| Congo Red             |    | Kelényi, 1967        |
| K114                  |    | Crystal et al., 2003 |
| Pittsburgh compound-B |    | Ye et al., 2008      |
| PTAA                  |    | Herland et al., 2007 |
| Resveratrol           |    | Ahn et al., 2007     |
| SH-516                |   | Volkova et al., 2007 |
| T-284                 |  | Volkova et al., 2008 |
| Thiazin red           |  | Mena et al., 1996    |
| Thioflavin S          |  | Levine, 1993         |
| Thioflavin T          |  | Levine, 1993         |
| X-34                  |  | Styren et al., 2000  |

**Table 4.1: Small molecules used to monitor amyloid aggregation**

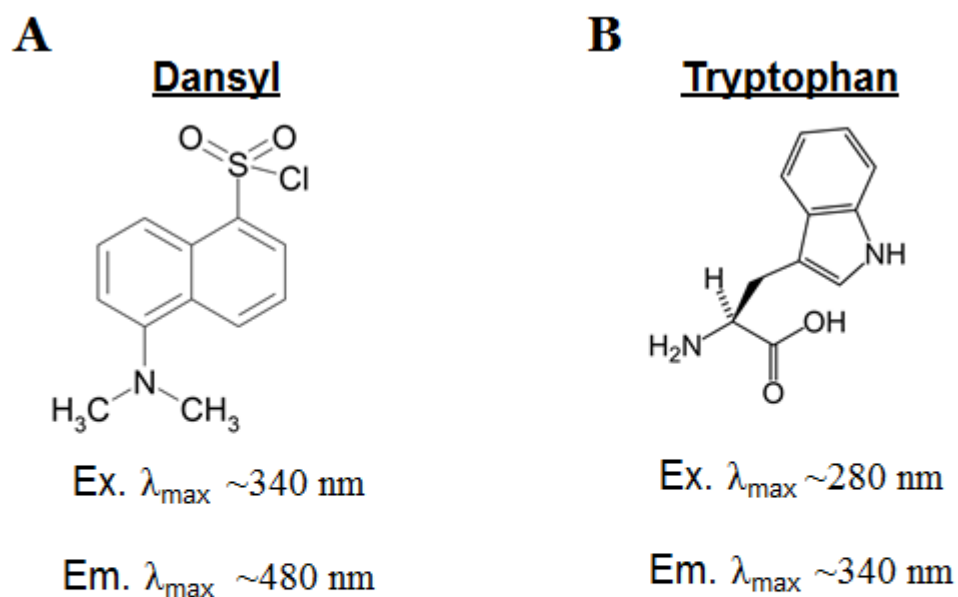


**Figure 4.1: FRET probes used to monitor VQIVYK aggregation.** (A) Dansyl and (B) tryptophan comprise a FRET pair. When the two fluorophores are within 21 Å, the fluorescence of tryptophan in response to 280 nm incident light transfers to dansyl, and the maximum emission wavelength shifts from 340 to 480 nm.

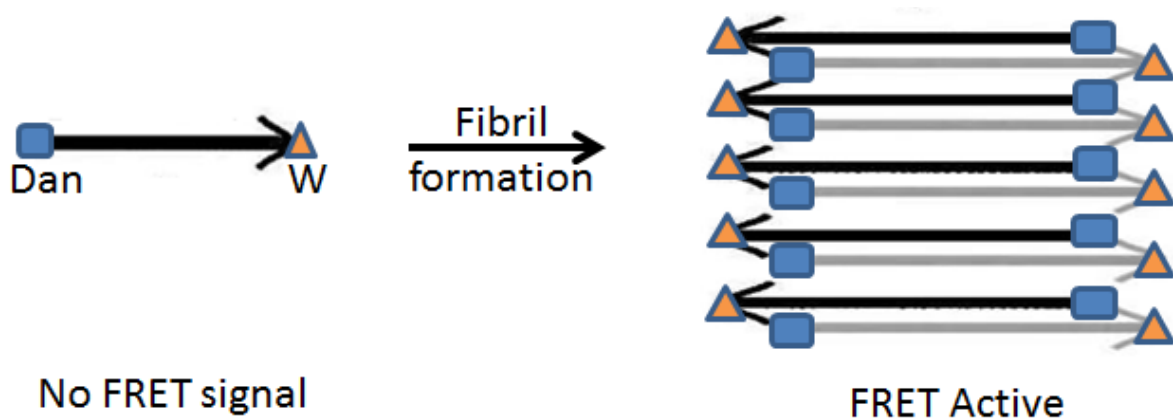


**Figure 4.2: Formation of a steric zipper induces FRET in labeled VQIVYK.** When VQIVYK labeled with dansyl (Dan) and tryptophan (W) is monomeric, FRET is inactive. When the labeled peptide forms an amyloid-like steric zipper, the fluorophores are brought to within their 21 Å Förster distance and undergo FRET.

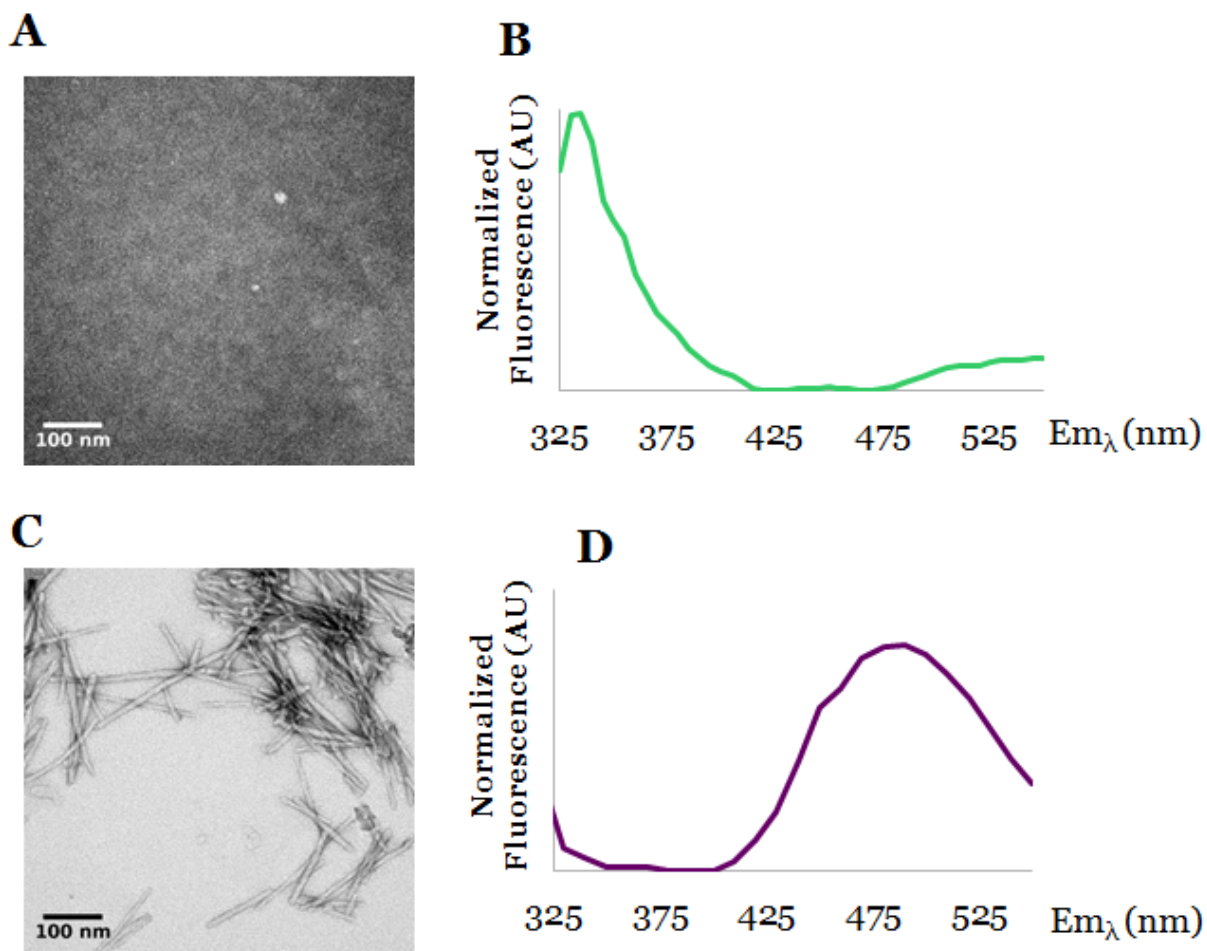


**Figure 4.3: FRET activity in DV7W is correlated with amyloid fibril formation.** Before DV7W forms fibrils (A), FRET is minimal, and the maximum emission wavelength is  $\sim 340$  nm (B). Once fibrils are formed (C), the maximum emission wavelength shifts to  $\sim 480$  nm (D). (A) and (C) are transmission electron micrographs depicting samples stained with 2% uranyl acetate, and both contain 100 nm scale bars. (B) and (D) represent emission spectra of the samples following excitation with 280 nm incident light.

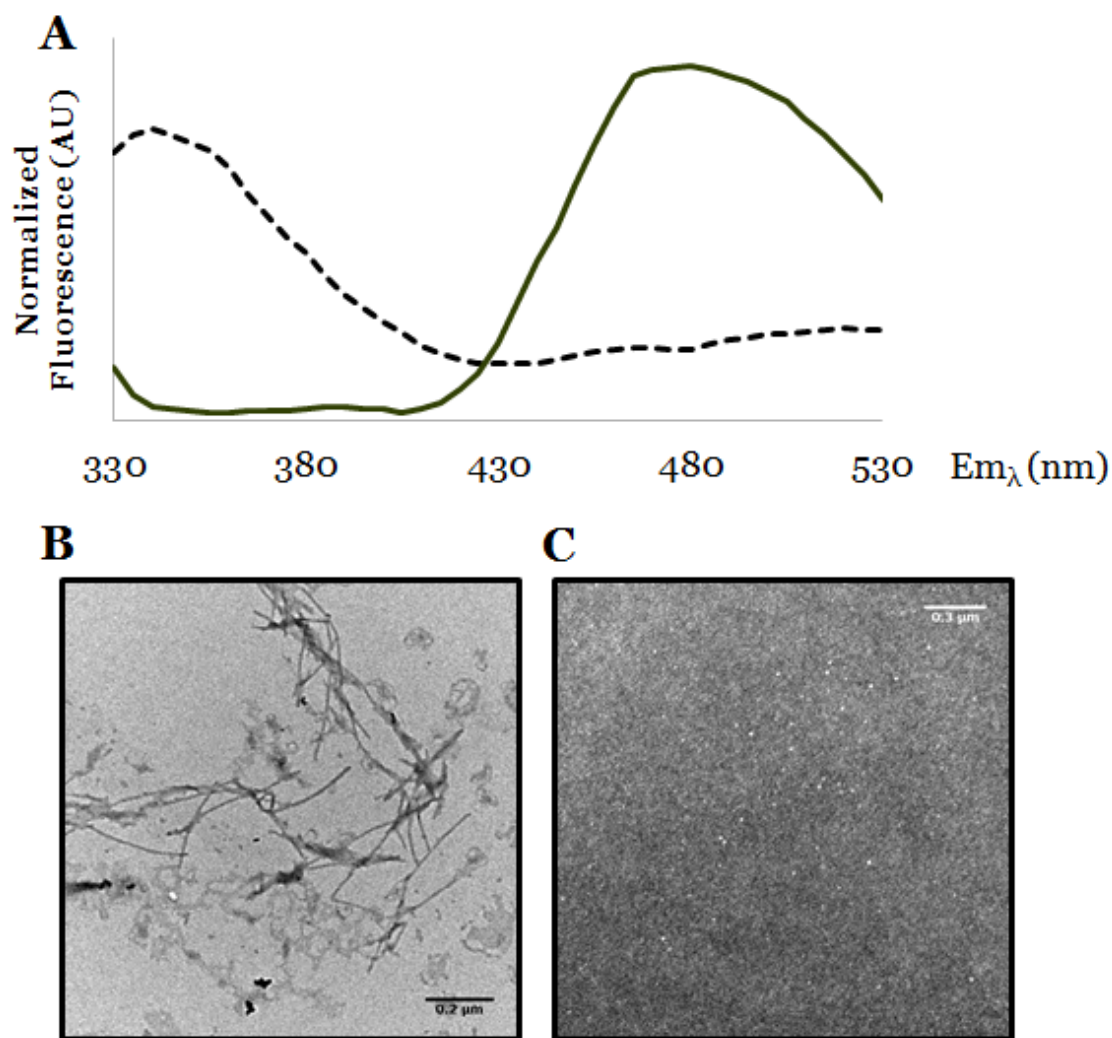


**Figure 4.4: Aggregation-induced FRET in DV7W is reversible.** (A) Emission spectra of 10  $\mu$ M DV7W aggregates before (solid) and after (dashed) dissolution with 7M guanidinium hydrochloride. 280 nm incident light was used to excite the samples. Stained with 2% uranyl acetate, transmission electron micrographs show the control sample with no guanidinium still contains aggregates (B), whereas the guanidinium-treated sample is devoid of fibrils (C).

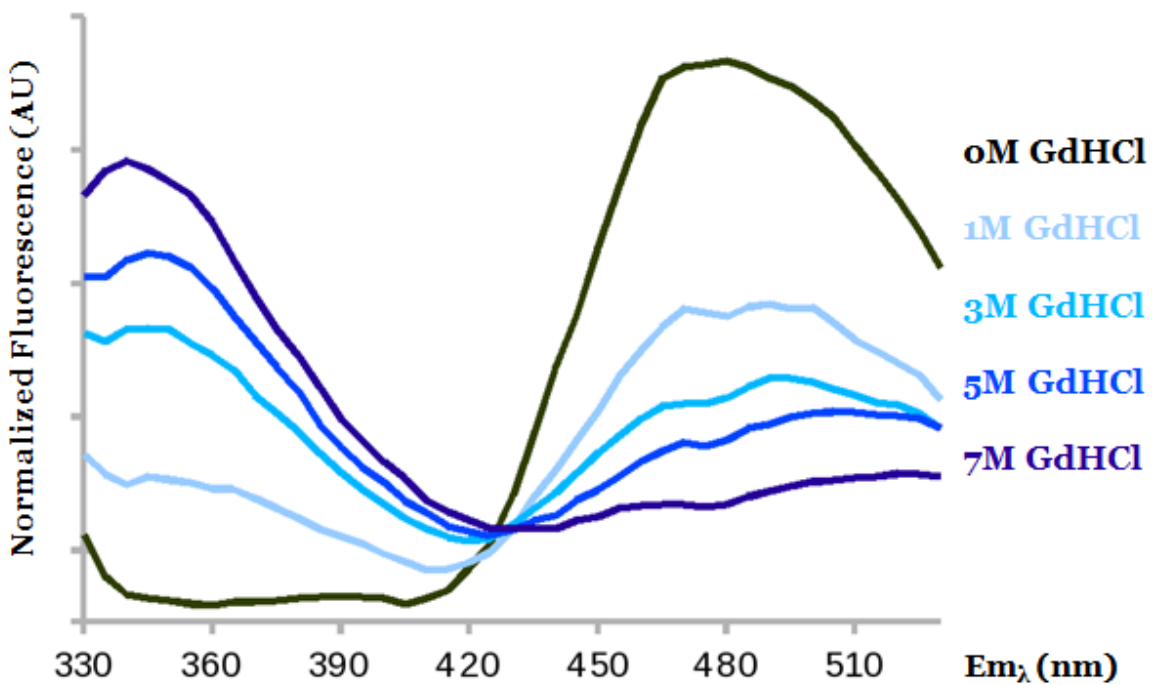


**Figure 4.5. Gadolinium hydrochloride (GdCl) dissolves DV7W fibrils in a dose-dependent manner.** FRET exhibited by DV7W fibrils is reduced as they are treated with higher concentrations of GdHCl. DV7W concentration is 10  $\mu$ M, and samples are excited with 280 nm light.

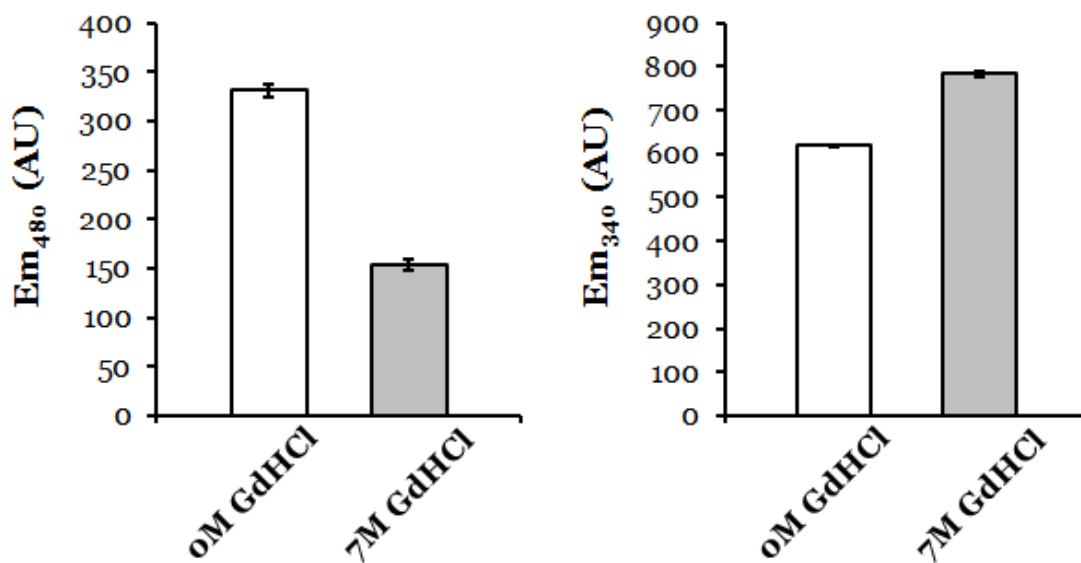


**Figure 4.6: Monitoring fluorescence at either 340 or 480 nm is suitable for a high throughput screen of Dv7W disaggregation.** All samples contained 10  $\mu$ M DV7W treated for 24 hours using the gadolinium hydrochloride (GdHCl) concentration indicated, at 37° C. Samples were excited with 280 nm incident light.



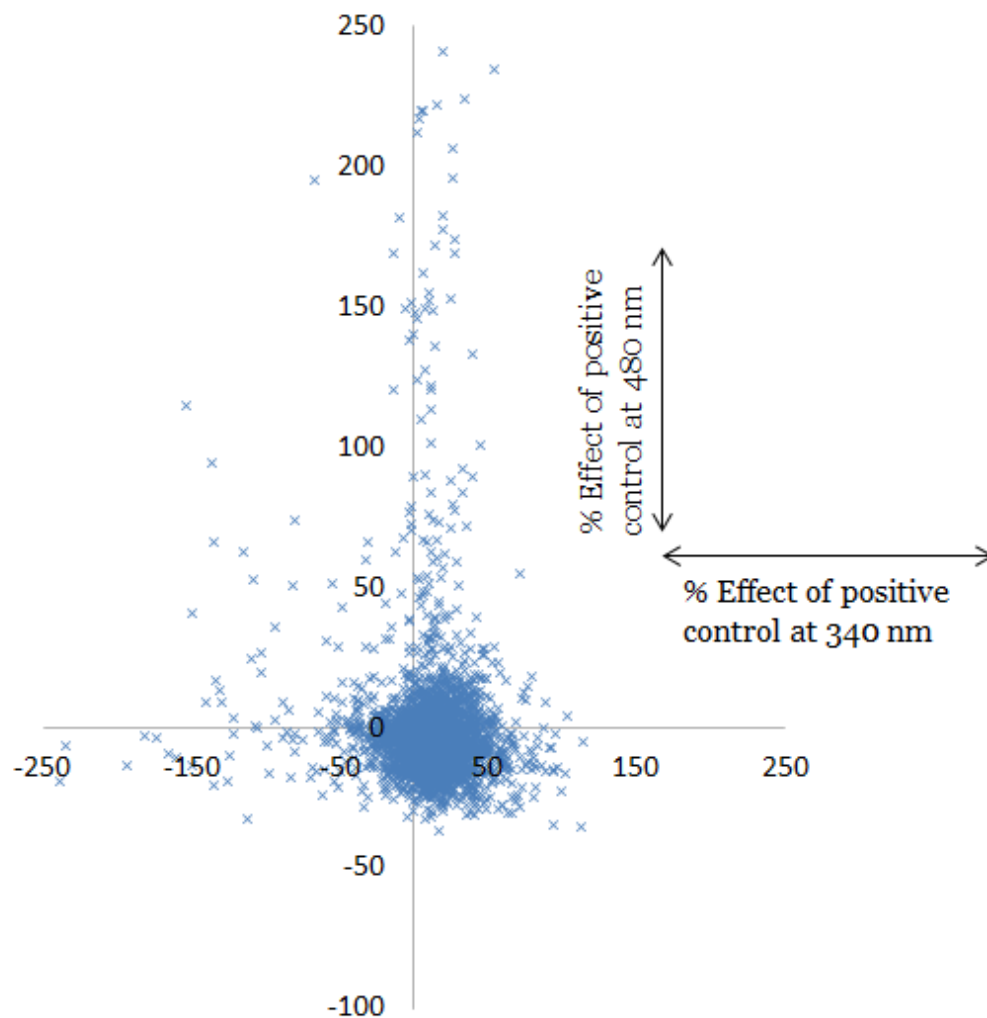


**Figure 4.7. Results from a pilot high throughput screen (HTS).** Each point represents a single compound, plotted along the x- and y-axes according to how much it affects fluorescence at 340 and 480 nm, respectively, as a % of the effect observed in the positive control for disaggregation, 7M guanidinium hydrochloride. Each sample was incubated with 10  $\mu$ M DV7W fibrils for 24 hours at 37° C, then excited with 280 nm light.

## References

- Ahn, J. S., Lee, J. H., Kim, J. H., and Paik, S. R. (2007). Novel method for quantitative determination of amyloid fibrils of alpha-synuclein and amyloid beta/A4 protein by using resveratrol. *Analytical Biochemistry*. *367*, 259-265.
- Breslow, R., and Guo, T. (1990). Surface tension measurements show that chaotropic salting-in denaturants are not just water-structure breakers. *Proceedings of the National Academy of Sciences, USA*. *87*, 167-169.
- Byrne, N., and Angell, C. A. (2009). Formation and dissolution of hen egg white lysozyme amyloid fibrils in protic ionic liquids. *Chemical Communications*. *9*, 1046-1048.
- Cisek, K., and Kuret, J. (2012). QSAR studies for prediction of cross-beta sheet aggregate binding affinity and selectivity. *Bioorganic & Medicinal Chemistry*. *20*, 1434-1441.
- Crowe, A., Ballatore, C., Hyde, E., Trojanowski, J. Q., and Lee, V. M. (2007). High throughput screening for small molecule inhibitors of heparin-induced tau fibril formation. *Biochemical and Biophysical Research Communications*. *358*, 1-6.
- Crowe, A., Huang, W., Ballatore, C., Johnson, R. L., Hogan, A. M., Huang, R., Wichterman, J., McCoy, J., Huryn, D., Auld, D. S., Smith, A. B. 3rd, Inglese, J., Trojanowski, J. Q., Austin, C. P., Brunden, K. R., and Lee, V. M. (2009). Identification of aminothienopyridazine inhibitors of tau assembly by quantitative high-throughput screening. *Biochemistry*. *48*, 7732-7745.
- Crystal, A. S., Giasson, B. I., Crowe, A., Kung, M. P., Zhuang, Z. P., Trojanowski, J. Q., and Lee, V. M. (2003). A comparison of amyloid fibrillogenesis using the novel fluorescent compound K114. *Journal of Neurochemistry*. *86*, 1359-1368.

Deng, W., Cao, A., and Lai, L. (2007). Detecting the inter-peptide arrangement and maturation process of transthyretin (105-115) amyloid fibril using a FRET pair with short Förster distance. *Biochemical and Biophysical Research Communications*. *362*, 689-694.

Deng, W., Cao, A., and Lai, L. (2008). Distinguishing the cross-beta spine arrangements in amyloid fibrils using FRET analysis. *Protein Science*. *17*, 1102-1105.

DeSantis, M. E., Leung, E. H., Sweeny, E. A., Jackrel, M. E., Cushman-Nick, M., Neuhaus-Follini, A., Vashist, S., Sochor, M. A., Knight, M. N., and Shorter, J. (2012). Operational plasticity enables hsp104 to disaggregate diverse amyloid and nonamyloid clients. *Cell*. *151*, 778-793.

Duff, K., Kuret, J., and Congdon, E. E. (2010). Disaggregation of tau as a therapeutic approach to tauopathies. *Current Alzheimer Research*. *7*, 235-240.

Eisenberg, D., and Jucker, M. (2012). The amyloid state of proteins in human diseases. *Cell*. *148*, 1188-1203.

Fowler, D. M., Koulov, A. V., Alory-Jost, C., Marks, M. S., Balch, W. E., and Kelly, J. W. (2006). Functional amyloid formation within mammalian tissue. *PLoS Biology*. *4*, e6.

Fowler, D. M., Koulov, A. V., Balch, W. E., and Kelly, JW. (2007). Functional amyloid—from bacteria to humans. *Trends in Biochemical Sciences*. *32*, 217-224.

Glabe, C. G. (2008). Structural classification of toxic amyloid oligomers. *Journal of Biological Chemistry*. *283*, 29639-29643.

Groenning, M., Olsen, L., van de Weert, M., Flink, J. M., Frokjaer, S., and Jørgensen, F. S. (2007). Study on the binding of Thioflavin T to beta-sheet-rich and non-beta-sheet cavities. *Journal of Structural Biology*. *158*, 358-369.

Groenning, M. (2009). Binding mode of Thioflavin T and other molecular probes in the context of amyloid fibrils-current status. *Journal of Chemical Biology*. *3*, 1-18.

Hattori, M., Sugino, E., Minoura, K., In, Y., Sumida, M., Taniguchi, T., Tomoo, K., and Ishida, T. (2008). Different inhibitory response of cyandin and methylene blue for filament formation of tau microtubule-binding domain. *Biochemical and Biophysical Research Communications*. *374*, 158-163.

Heinrich, S. U., and Lindquist, S. (2011). Protein-only mechanism induces self-perpetuating changes in the activity of neuronal Aplysia cytoplasmic polyadenylation element binding protein (CPEB). *Proceedings of the National Academy of Sciences, USA*. *108*, 2999-3004.

Herland, A., Björk, P., Hania, P. R., Scheblykin, I. G., and Inganäs, O. (2007). Alignment of a conjugated polymer onto amyloid-like fibrils. *Small*. *3*, 318-325.

Hernández, F., and Avila, J. (2007). Tauopathies. *Cellular and Molecular Life Sciences*. *64*, 2219-2233.

Iba, M., Guo, J. L., McBride, J. D., Zhang, B., Trojanowski, J. Q., and Lee, V. M. (2013). Synthetic tau fibrils mediate transmission of neurofibrillary tangles in a transgenic mouse model of Alzheimer's-like tauopathy. *Journal of Neuroscience*. *33*, 1024-1037.

Ittner, L. M., and Götz, J. (2011). Amyloid-beta and tau—a toxic pas de deux in Alzheimer's disease. *Nature Reviews Neuroscience*. *12*, 65-72.

- Joo, C., Balci, H., Ishitsuka, Y., Buranachai, C., and Ha, T. (2008). Advances in single-molecule fluorescence methods for molecular biology. *Annual Review of Biochemistry*. *77*, 51-76.
- Kaylor, J., Bodner, N., Edridge, S., Yamin, G., Hong, D. P., and Fink, A. L. (2005). Characterization of oligomeric intermediates in alpha-synuclein fibrillation: FRET studies of Y125W/Y133F/Y136F alpha-synuclein. *Journal of Molecular Biology*. *353*, 357-372.
- Kelényi, G. (1967). Thioflavin S fluorescent and Congo red anisotropic stainings in the histologic demonstration of amyloid. *Acta Neuropathologica*. *7*, 336-348.
- Klunk, W. E., Debnath, M. L., and Pettegrew, J. W. (1995). Development of small molecule probes for the beta-amyloid protein of Alzheimer's disease. *Neurobiology of Aging*. *15*, 691-698.
- Landau, M., Sawaya, M. R., Faull, K. F., Laganowsky, A., Jiang, L., Sievers, S. A., Liu, J., Barrio, J. R., and Eisenberg, D. (2011). Towards a phamacophore for amyloid. *PLoS Biology*. *9*, e1001080.
- LeVine, H. 3<sup>rd</sup>. (1999). Quantification of beta-sheet amyloid fibril structures with thioflavin T. *Methods in Enzymology*. *309*, 274-284.
- LeVine, H. 3<sup>rd</sup>. (2005). Multiple ligand binding sites on A-beta (1-40) fibrils. *Amyloid*. *12*, 5-14.
- Lindgren, M., Sörgjerd, K., and Hammarström, P. (2005). Detection and characterization of aggregates, prefibrillar oligomers, and protofibrils using fluorescence spectroscopy. *Biophysical Journal*. *88*, 4200-4211.
- Liu, M., Ni, J., Kosik, K. S., and Yeh, L. A. (2004). Development of a fluorescent high throughput assay for tau aggregation. *Assay and Drug Development Technologies*. *2*, 609-619.

Maji, S. K., Perrin, M. H., Sawaya, M. R., Jessberger, S., Vadodaria, K., Rissman, R. K., Singru, P. S., Nilsson, K. P., Simon, R., Schubert, D., Eisenberg, D., Rivier, J., Sawchenko, P., Vale, W., and Riek, R. (2009). Functional amyloids as natural storage of peptide hormones in pituitary secretory granules. *Science*. *325*, 328-332.

Mena, R., Edwards, P., Pérez-Olvera, O., and Wischik, C. M. (1995). Monitoring pathological assembly of tau and beta-amyloid proteins in Alzheimer's disease. *Acta Neuropathologica*. *89*, 50-56.

Mukrasch, M. D., Bibow, S., Korukottu, J., Jeganathan, S., Biernat, J., Griesinger, C., Mandelkow, E., and Zweckstetter, M. (2009). Structural polymorphism of 441-residue tau at single residue solution. *PLoS Biology*. *7*, e34.

Nelson, R., Sawaya, M. R., Balbirnie, M., Madsen, A. Ø., Riek, C., Grothe, R., and Eisenberg, D. (2005). Structure of the cross- $\beta$  spine of amyloid-like fibrils. *Nature*. *435*, 773-778.

Onuki, R., Nagasaki, A., Kawasaki, H., Baba, T., Uyeda, T. Q., and Taira, K. (2002). Confirmation by FRET in individual living cells of the absence of significant amyloid beta-mediated caspase 8 activation. *Proceedings of the National Academy of Sciences, USA*. *99*, 14716-14721.

Pickhardt, M., Gazova, Z., von Bergen, M., Khlistunova, I., Wang, Y., Hascher, A., Mandelkow, E. M., Biernat, J., and Mandelkow, E. (2005). Anthraquinones inhibit tau aggregation and dissolve Alzheimer's paired filaments in vitro and in cells. *Journal of Biological Chemistry*. *280*, 3628-3635.

Pickhardt, M., Larbig, G., Khlistunova, I., Coksezen, A., Meyer, B., Mandelkow, E. M., Schmidt, B., and Mandelkow, E. (2007). Phenylthiazolyl-hydrazide and its derivatives are potent inhibitors of tau aggregation and toxicity in vitro and in cells. *Biochemistry*. 46. 10016-10023.

Rojas Quijano, F. A., Morrow, D., Wise, B. M., Brancia, F. L. and Goux, W. J. (2006). Prediction of nucleating sequences from amyloidogenic propensities of tau-related peptides. *Biochemistry* 45, 4638–4652.

Saeed, S. M., and Fine, G. (1967). Thioflavin-T for amyloid detection. *American Journal of Clinical Pathology*. 47, 588-593.

Santa-María, I., Pérez, M., Hernández, F., Avila, J., and Moreno, F. J. (2006). Characteristics of the binding of thioflavin S to tau paired helical filaments. *Journal of Alzheimers Disease*. 9, 279-285.

Sawaya, M. R., Sambashivan, S., Nelson, R., Ivanova, M. I., Sievers, S. A., Apostol, M. I., Thompson, M. J., Balbirnie, M., Wiltzius, J. J., McFarlane, H. T., Madsen, A. Ø., Riek, C., and Eisenberg, D. (2007). Atomic structures of amyloid cross- $\beta$  spines reveal varied steric zippers. *Nature*. 447, 453–457.

Schmidt, M. L., Schuck, T., Sheridan, S., Kung, M. P., Kung, H., Zhuang, Z. P., Bergeron, C., Lamarche, J. S., Skovronsky, D., Giasson, B. I., Lee, V. M., and Trojanowski, J. Q. (2001). The fluorescent Congo red derivative, (trans, trans)-1-bromo-2,5-bis-(3-hydroxycarbonyl-4-hydroxy)styrylbenzene (BSB), labels diverse beta-pleated sheet structures in postmortem human neurodegenerative disease brains. *The American Journal of Pathology*. 159, 937-943.

Si, K., Choi, Y. B., White-Grindley, E., Majumdar, A., and Kandel, E. R. (2010). Aplysia CPEB can form prion-like multimers in sensory neurons that contribute to long-term facilitation. *Cell*. *140*, 421-435.

Sievers, S. A., Karanicolas, J., Chang, H. W., Zhao, A., Jiang, L., Zirafi, O., Stevens, J. T., Münch, J., Baker, D., and Eisenberg, D. (2011). Structure-based design of non-natural amino-acid inhibitors of amyloid fibril formation. *Nature*. *475*, 96-100.

Small, G. W., Kepe, V., Siddarth, P., Ercoli, L. M., Merrill, D. A., Donaghue, N., Bookheimer, S. Y., Martinez, J., Omalu, B., Bailes, J., and Barrio, J. R. (2013). PET scanning of brain tau in retired National Football League players: preliminary findings. *American Journal of Geriatric Psychiatry*. *21*, 138-144.

Styren, S. D., Hamilton, R. L., Styren, G. C., and Klunk, W. E. (2000). X-34, a fluorescent derivative of Congo red: a novel histochemical stain for Alzheimer's disease pathology. *Journal of Histochemistry and Cytochemistry*. *48*, 1223-1232.

Wang, H., Duennwald, M. L., Roberts, B. E., Rozeboom, L. M., Zhang, Y. L., Steele, A. D., Krishnan, R., Su, L. J., Griffin, D., Mukhopadhyay, S., Hennessy, E. J., Weigele, P., Blanchard, B. J., King, J., Deniz, A. A., Buchwald, S. L., Ingram, V. M., Lindquist, S., and Shorter, J. (2008). Direct and selective elimination of specific prions and amyloids by 4,5-dianilinophthalimide and analogs. *Proceedings of the National Academy of Sciences, USA*. *105*, 7159-7164.

Westermarck, P., Benson, M. D., Buxbaum, J. N., Cohen, A. S., Frangione, B., Ikeda, S., Masters, C. L., Merlini, G., Saraiva, M. J., and Sipe, J. D. (2007). A primer of amyloid nomenclature. *Amyloid*. *14*, 179-83.



Volkova, K. D., Kovalska, V. B., Balanda, A. O., Vermeij, R. J., Subramaniam, V., Slominskii, Y. L., and Yarmoluk, S. M. (2007). Cyanine dye-protein interactions: looking for fluorescent probes for amyloid structures. *Journal of Biochemical and Biophysical Methods*. *70*, 727-733.

Volkova, K. D., Kovalska, V. B., Balanda, A. O., Losytskyy, M. Y., Golub, A. G., Vermeij, R. J., Subramaniam, V., Tolmachev, O. I., and Yarmoluk, S. M. (2008). Specific fluorescent detection of fibrillar alpha-synuclein using mono- and trimethine cyanine dyes. *Bioorganic and Medicinal Chemistry*. *16*, 1452-1459.

von Bergen, M., Friedhoff, P., Biernat, J., Heberle, J., Mandelkow, E. M., and Mandelkow, E. (2000). Assembly of tau protein into Alzheimer paired helical filaments depends on a local sequence motif (<sup>306</sup>VQIVYK<sup>311</sup>) forming  $\beta$  structure. *Proceedings of the National Academy of Sciences, USA*. *97*, 5129-34.

Ye, L., Velasco, A., Fraser, G., Beach, T. G., Sue, L., Osredkar, T., Libri, V., Spillantini, M. G., Goedert, M., and Lockhart, A. (2008). In vitro high affinity alpha-synuclein binding sites for the amyloid imaging agent PIB are not matched by binding to Lewy bodies in postmortem human brain. *Journal of Neurochemistry*. *105*, 1428-1437.

Zhang, J. H., Chung, T. D., and Oldenburg, K. R. (1999). A simple statistical parameter for use in evaluation and validation of high throughput screening assays. *Journal of Biomolecular Screening*. *4*, 67-73.

## Chapter 5: Towards elucidation of the toxic species in tauopathies

### **Abstract**

Amyloid fibrils have long been suspected to be the toxic entities in amyloid diseases such as Alzheimer's disease and Parkinson's disease. However, emerging evidence suggests that smaller, soluble oligomers may actually represent the disease agents. A recent crystal structure of a small toxic amyloid oligomer, a general structure which we termed cylindrin, prompted us to identify segments in tau protein that might form a similar assembly. In this chapter, I identify <sup>142</sup>AKGADGKITKIA<sup>152</sup>, a segment of tau which exhibits properties of other amyloid oligomers when expressed as a tandem repeat. These include amyloidogenicity, cytotoxicity, and the ability to form an oligomeric assembly. The work in this chapter suggests that this segment is responsible for tau oligomerization and the pathology observed in tauopathies.

# Introduction

## **Amyloid oligomers**

Despite the historic association of amyloid protein diseases with ordered, fibrillar aggregates, some evidence suggests that the toxic forms of amyloid proteins are instead small oligomers of these same proteins (Kayed et al., 2003; Kodali and Wetzel, 2007; Cowan et al., 2012). These noncovalent assemblies are more cytotoxic than either monomers or fibrils of the same protein, and frequently bind A11, a conformational antibody that binds oligomers but not fibrils (Glabe, 2009). Studying oligomers is complicated by their transient nature; depending on the protein and specific preparatory method, the oligomers can vary widely in size, morphology, kinetic stability and structural plasticity.

Like other amyloid proteins, there has been recent evidence that oligomers of tau are in fact responsible for the pathology of tauopathies. Several transgenic models of tauopathy, ranging from mice (Yoshiyama et al., 2007), to flies (Wittmann et al., 2001), and zebrafish (Paquet et al., 2009), have all exhibited neuronal defects in the absence of fibril formation. Additionally, another research group found that oligomers prepared from full-length tau impaired mouse memory when injected into the hippocampus (Lasagna-Reeves et al., 2011).

## **Cylindrin**

Recently, our lab reported the first atomic resolution crystal structure of an amyloid-related oligomer (Laganowsky et al., 2012). Formed by an amyloidogenic segment from the chaperone protein alphaB-crystallin, the oligomeric structure consists of a six-stranded

antiparallel barrel of cylindrical shape, termed cylindrin. This assembly further satisfied other criteria for a small amyloid oligomer, namely cytotoxicity and reactivity towards A11. Allowing for a range of possibilities in parameters such as the number of strands and shear number of the assembly, we posit that cylindrin-like assemblies represent the general structure of small toxic amyloid oligomers, and are responsible, at least in part, for the pathology associated with amyloid diseases.

### **Identification of cylindrin-like segments in tau**

Hypothesizing that cylindrin-like oligomers can be found in other amyloid proteins, we sought to identify 11-residue segments in tau protein that might also form a cylindrin-like assembly. In analyzing the atomic structure, we generated general criteria to predict which sequences would be prone to adopting the fold. Segments ought not contain proline, for its beta-strand breaking effect, nor should they contain cysteine, for potential complications arising from disulfide bond formation. Hydrophobic residues fill the interior of the cylinder, ideally with larger side chains to provide close packing. In order to accommodate efficient packing by the other side chains, the sixth of the 11-residue segment must be glycine. And finally, to stabilize the assembly in aqueous solution, outward-facing residues should be polar.

## **Results**

## **Expression and characterization of predicted cylindrin-like tau proteins**

Based on the criteria described above, we identified six segments which we hypothesized are most likely to form a cylindrin-like assembly from the longest tau isoform, and expressed them as tandem repeats connected by a di-glycine linker, referred to as TauTR1-6 (**Table 5.1**). Briefly, the tandem repeats were expressed as fusion proteins, with hexahistidine and maltose-binding protein tags attached to the N-terminus via a Tobacco Etch Virus (TEV) protease recognition sequence. After an initial crude purification using a nickel-based column, the protein was cleaved overnight using recombinantly-expressed TEV protease, and the region comprising the tandem repeat segment was isolated by collected the flowthrough of a nickel column. A final purification step using reversed-phase HPLC and subsequent lyophilization yielded the dry peptides, which were verified using MALDI-TOF mass spectrometry. Among the six proteins expressed, TauTR1, TauTR2, TauTR5, and TauTR6 purified readily, with the remaining two irreversibly aggregating during purification.

Using a Rosetta-based 3D profile method, which identifies sequences that form steric-zipper spines (Thompson et al., 2006), we determined that all but TauTR2 are predicted to form amyloid-like fibrils (**Figure 5.1**). We confirmed this prediction using transmission electron microscopy, visualizing the samples after incubating them at elevated temperature with agitation (**Figure 5.2**).

We next sought to measure the cytotoxic potential of the constructs, comparing soluble preparations with those had formed fibrils using an MTT-based cytotoxicity assay (Berridge et al., 2005). We determined that fibrils derived from any of the constructs were of negligible cytotoxicity towards cultured human cells (**Figure 5.3**). Among the soluble samples, which were prepared in phosphate-buffered saline pH 7.4, TauTR1 was strongly cytotoxic, killing

>60% of HeLa cells. No other construct was cytotoxic in a statistically significant way. To determine whether an oligomeric assembly is responsible for the observed cytotoxicity, we subjected the cytotoxic sample to analytical size exclusion chromatography (**Figure 5.4**). The single elution peak had a retention time centered slightly below 30 minutes. This places its apparent molecular weight somewhere between cytochrome C (12.6 kDa) and insulin (5.8 kDa), which eluted at 24 and 31 minutes, respectively. Given that the molecular weight of TauTR1 is 2.3 kDa, this most likely represents a trimeric assembly, which would correspond to 6.9 kDa. A 4.6 kDa dimer would elute later than insulin, and a 9.2 kDa tetramer would likely exhibit a retention time much closer to cytochrome C.

Unfortunately, all of the tau tandem repeat constructs have been recalcitrant to crystallization efforts so far. Robot-based crystal screens of 1440 different conditions were conducted on each construct dissolved to 30 mg/ml in PBS pH 7.4 and water individually, but the only crystals obtained were of salt. “Skin”-covered drops with precipitate were observed for constructs TauTR2 and TauTR6, but could not be optimized to yield crystals.

## Discussion

This work began with several segments of tau protein that were predicted to form a small amyloid oligomer. After recombinantly producing these segments, we determined that TauTR1, a tandem repeat construct, meets many of the criteria that define these assemblies. Using an MTT-based cytotoxicity assay, we observed a 200  $\mu$ M fibrillar preparations of TauTR1 to be benign, killing < 5% of cells in a human cell line. This effect is indistinguishable from buffer alone, which killed a similar number of cells. In contrast, we found that an apparently trimeric

soluble preparation at the same concentration is highly cytotoxic, killing about 67% of cells. These experiments support the toxic oligomer hypothesis, as well as the view that a cylindrin-like assembly comprises this oligomer.

TauTR1 comprises residues 142-152 of tau. This lies outside of the microtubule-binding domains, which have been the focus of the majority of tauopathy-related research, including our own (Ballatore et al., 2012; Sievers et al., 2011; Lee and Leugers, 2012). Targeting this region is certainly a justifiable aim. Research has shown that some hereditary frontotemporal dementias, a subclass of tauopathy, can be traced to mutations in this region (Hasegawa et al., 1998; von Bergen et al., 2001). Additionally, these mutations, such as P301L and  $\Delta$ K280, drastically increase the efficiency of fibril formation *in vitro*. Thus, these microtubule-binding domains are clearly relevant to disease, and comprise the region that actually self-associate within amyloid fibrils. However, not all tauopathy-associated genetic factors lie within these domains. Of particular interest is the mutation A152T, which was initially found in a patient exhibiting many hallmarks of typical tauopathy, including filamentous tau deposits, memory disturbance, and progressive dementia (Kovacs et al., 2011). Later work described it to likely be a non-fully penetrant pathogenic mutation, strongly correlated with the entire spectrum of frontotemporal dementias and Alzheimer disease (Lee et al., 2013; Kara et al., 2012).

Our findings, in concert with these reports, lend credence to the hypothesis that fibrils are not the toxic species in tauopathies. It could be that the alanine to threonine mutation at residue 152 serves to stabilize the cylindrin-like structure. To further test the hypothesis that TauTR1 represents the effectively models the toxic tau assembly, future work could attempt to characterize TauTR1, with the A152T disease-associated mutation in place. One could also assay whether the disease-associated mutation increases the cytotoxicity of TauTR1.

## Materials & Methods

### **Recombinant Tau Tandem Repeat Peptide Plasmid Construction**

All synthetic genes for cylindrin candidates from tau (Tau-TR1, Tau-TR2, Tau-TR3, Tau-TR4, Tau-TR5, Tau-TR6), codon optimized for *Escherichia coli*, were designed using DNAWorks and constructed using PCR-based gene synthesis as described (Hoover and Lubkowski, 2002). The synthetic genes were PCR amplified with Platinum Pfx polymerase (Invitrogen, Carlsbad, CA) with the N-terminal primer containing a SacI restriction and TEV protease site, and a C-terminal primer containing a stop codon and XhoI restriction site. Agarose gel purified PCR products were extracted using the QIAquick Gel Extraction Kit (Qiagen, Valencia, CA). Gel purified PCR products and custom vector, p15-MBP (described below), were digested with SacI and XhoI according to the manufacturer's protocol (New England Biolabs, Ipswich, MA). The p15-MBP custom vector is a chimera constructed from the NdeI and XhoI digestion products pET15b (Novagen, Gibbstown, NJ), and the maltose binding protein (MBP) gene from pMALC2X (New England Biolabs, Ipswich, MA), resulting in an N-terminal His-tag MBP fusion vector. Digested vector products were gel purified and extracted as described above. DNA concentrations were determined using BioPhotometer UV/VIS Photometer (Eppendorf, Westbury, NY). A ligation mixture was performed using a Quick Ligation kit (New England Biolabs, Ipswich, MA) according to the manufacturer's protocol and transformed into *E. coli* cell line TOP10 (Invitrogen, Carlsbad, CA). Several colonies were grown overnight, and plasmid containing the synthetic genes were purified using QIAprep Spin Miniprep Kit (Qiagen,



Valencia, CA). The final constructs were sequenced prior to transformation into *E. coli* expression cell line BL21 (DE3) gold cells (Agilent Technologies, Santa Clara, CA).

### **Recombinant Tau Tandem Repeat Peptide Expression**

A single colony was inoculated into 50 mL LB Miller broth (Fisher Scientific, Pittsburgh, PA) supplemented with 100 µg/mL ampicillin (Fisher Scientific, Pittsburgh, PA) and grown overnight at 37 °C. One liter of LB Miller supplemented with 100 µg/mL ampicillin in 2 L shaker flasks was inoculated with 7 mL of overnight culture and grown at 37° C until the culture reached an OD600 ~0.6-0.8 using a BioPhotometer UV/VIS Photometer (Eppendorf, Westbury, NY). IPTG (Isopropyl β-D-1-thiogalactopyranoside) was added to a final concentration of 1 mM, and grown for 3-4 hours at 34° C. Cells were harvested by centrifugation at 5,000 x g for 10 minutes at 4 °C. The cell pellet was frozen and stored at -80 °C.

### **Recombinant Tau Tandem Repeat Peptide Purification**

The cell pellet was thawed on ice and re-suspended in buffer A (50 mM sodium phosphate, 0.25 M sodium chloride, 20 mM imidazole, pH 8.0) supplemented with Halt Protease Inhibitor Cocktail (Thermo Scientific, Rockford, IL) at 50 mL per 2 L of culture volume. The re-suspended culture was incubated on ice for 15 minutes prior to sonication. Crude cell lysate was clarified by centrifugation at 14,000 x g for 25 minutes at 4 °C. The clarified cell lysate was filtered through a 0.45 µm syringe filtration device (HPF Millex-HV, Millipore, Billerica, MA) before loading onto a 5 mL HisTrap-HP column (GE Healthcare,

Piscataway, NJ). The HisTrap-HP column was washed with five column volumes of buffer A and protein eluted with using 60% buffer B (50 mM sodium phosphate, 0.3 M sodium chloride, 500 mM imidazole, pH 8.0). Protein eluted around 50-70% buffer B and peak fractions pooled. A final concentration of 5 mM beta-mercaptoethanol (BME) and 1 mM ethylenediaminetetraacetic acid (EDTA) was added to the pooled sample prior to transferring to a Slide-A-Lyzer 10,000 MWCO dialysis cassette (Pierce, Thermo Fisher Scientific, Rockford, IL), and dialyzed against buffer C (25 mM sodium phosphate pH 8.0, 20 mM imidazole, 200 mM sodium chloride) at room temperature overnight. The dialyzed sample was pooled and 1/500 volume of TEV protease stock was added. The TEV protease reaction was incubated overnight at room temperature before loading over a 5 mL HisTrap-HP column equilibrated in buffer A. The flow through was collected, containing the recombinant cylindrin peptide with an additional N-terminal glycine residue resulting from TEV protease cleavage. Pooled recombinant Tau-TR1 peptide was 0.22  $\mu$ m filtered (Steriflip, Millipore, Billerica, MA) and further purified by reverse phase high performance liquid chromatography (RP-HPLC) on a 2.2 x 25 cm Vydac 214TP101522 column equilibrated in buffer RA (0.1% trifluoroacetic acid (TFA)/water) and eluted over a linear gradient from 0% to 100% buffer RB (Acetonitrile/0.1% TFA) in 40 minutes at a flow rate of 9 mL/min. Absorbance at 220nm and 280nm were recorded using a Waters 2487 dual  $\lambda$  absorbance detector (Waters, Milford, MA). Peak fractions containing peptide were assessed for purity by MALDI-TOF mass spectrometry (Voyager-DE-STR, Applied Biosystems, Carlsbad, CA). Samples were co-precipitated with matrix on a stainless steel MALDI plate (Applied Biosystems) in a 1:1 (v:v) ratio of protein sample to  $\alpha$ -cyano-4-hydroxycinnamic acid (saturated solution in 50% acetonitrile, 0.1% trifluoroacetic acid). Pooled fractions were frozen in liquid nitrogen and lyophilized. Dried peptide powders were stored in desiccant jars at -20° C.

## **TEV Expression and Purification**

The plasmid, pRK793, containing TEV protease with his- and polyarg-tag was expressed and purified as described previously with minor modifications (Kapust et al., 2001). After purification using the HisTrap-HP column, peak fractions were quickly pooled and dialyzed against TDB (20 mM Tris pH 8.0, 100 mM sodium chloride, 10% glycerol, 1mM EDTA, 5mM BME( $\beta$ -mercaptoethanol) ) for eight hours. Dialyzed sample was loaded onto HiTrap S HP column (GE Healthcare, Piscataway, NJ) equilibrated in TIA buffer (50 mM sodium chloride, 20 mM Tris pH 8.0). TEV was eluted with 50% TIB buffer (1 M sodium chloride, 20 mM Tris pH 8.0). Peak fractions were pooled and dialyzed against TSB (20mM Tris pH 8.0, 100mM sodium chloride, 1mM EDTA, 5mM BME, 30% glycerol) for several hours at 4 °C. Dialyzed protein sample was concentrated to 1.5 mg/mL, flash frozen and stored at -80 °C prior to use.

## **Size Exclusion Chromatography (SEC)**

One to five milligrams of lyophilized peptide was dissolved in 1 mL of SEC buffer (50 mM sodium phosphate, 150mM sodium chloride pH 7.0) and filtered through a 0.22 or 0.45  $\mu$ m Microporous Durapore polyvinylidene fluoride membrane (Millipore, Billerica, MA). Filtered samples were injected on a Superdex 200 10/300 GL column (GE Healthcare, Piscataway, NJ) equilibrated in SEC buffer at a flow rate of 0.4 mL/min. Absorbance at 220nm and 280nm were recorded using AKTA Explorer FPLC system (GE Healthcare, Piscataway, NJ). Protein standards were monitored by absorbance at 280nm, and cylindrin peptides monitored by absorbance at 220nm.

## **Cell Culture and Viability Assay**

Cell viability was investigated using a CellTiter 96 aqueous non-radioactive cell proliferation assay kit (MTT) (Promega cat. #G4100). PC-12 (ATCC; cat. # CRL-1721) and HeLa were used to assess the toxic effect of cylindrin peptides. HeLa cells were cultured in DMEM medium with 10% fetal bovine serum. PC-12 cells were cultured in ATCC-formulated RPMI 1640 medium (ATCC; cat.# 30-2001) with 10% heat-inactivated horse serum and 5% fetal bovine serum. Cells were maintained at 37 °C in 5% CO<sub>2</sub>. For all toxicity experiments, 96-well plates (Costar cat. # 3596) were used. HeLa, PC-12 cells were plated at 10,000 cells per well and SH-SY5Y cells were plated at 25,000 cells per well. Cells were cultured for 20h at 37 °C in 5% CO<sub>2</sub> prior to addition of peptide samples. 10 µl of sample was added to each well containing 90 µL medium, and allowed to incubate for 24h prior to the addition of 15 µl Dye solution (Promega. cat. #G4102) into each well, followed by incubation for 4h at 37°C in 5% CO<sub>2</sub>. After incubation, 100 µl solubilization Solution/Stop Mix (Promega cat. #G4101) was added to each well. After 12h incubation at room temperature, the absorbance was measured at 570nm. Background absorbance was recorded at 700nm. Each of the experiments was repeated 3 times with 4 replicates per sample per concentration. Abeta at 0.5 µM was a positive control. The results were normalized using the buffer-treated cell as 100% viability and 0.2% SDS-treated as 0% viability.

| Construct Name | Tau Residue # | Amino Acid Sequence |
|----------------|---------------|---------------------|
| Tau TR1        | 142 – 152     | AKGADGKTKIA         |
| Tau TR2        | 396 – 406     | SPVVSGDTSPR         |
| Tau TR3        | 410 – 420     | NVSSTGSIDMV         |
| Tau TR4        | 23 – 33       | RKDQGGYTMHQ         |
| Tau TR5        | 32 – 42       | GQDQEGDTDAG         |
| Tau TR6        | 115 – 125     | EDEAAGHVTQA         |

**Table 5.1. Tau tandem repeat constructs predicted to form cylindrin-like assemblies.** The tandem repeats consist of two copies of the amino acid sequence listed, connected by a di-glycine linker.

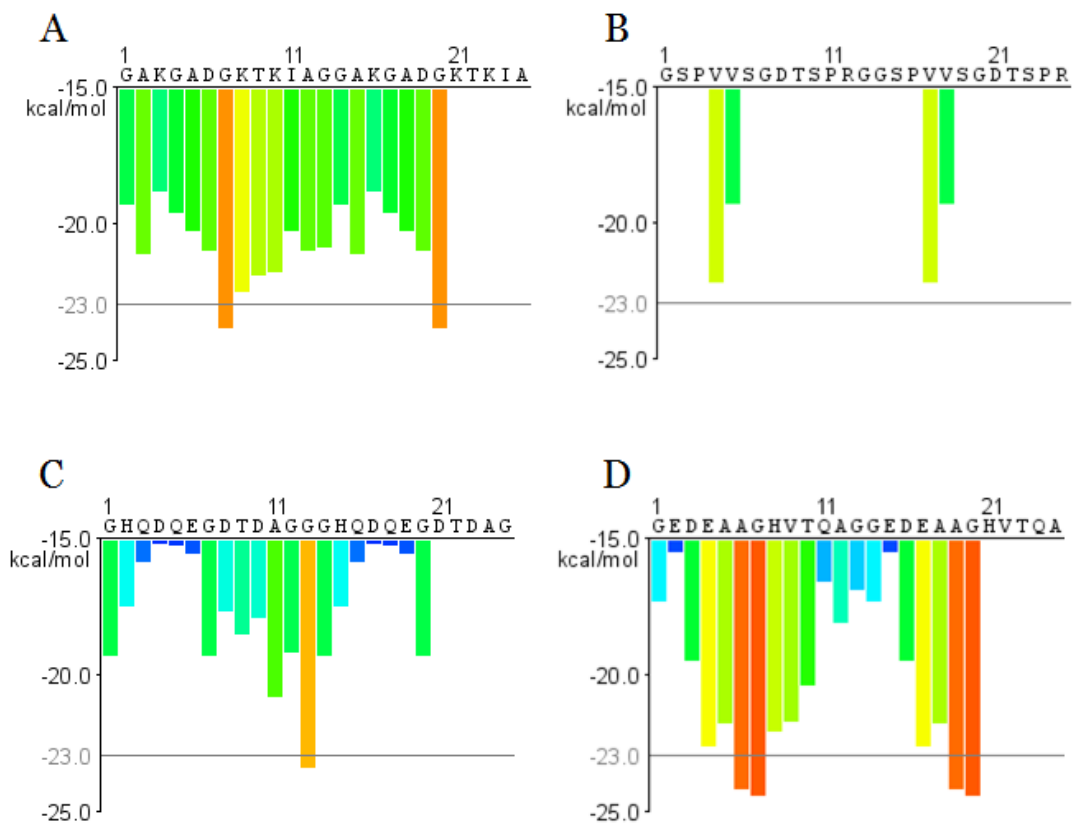


**Figure 5.1: The 3D profile method predicts that TauTR1, TauTR5, and TauTR6 will form amyloid-like fibrils, but not TauTR2.** The algorithm calculates the RosettaDesign energy (Kuhlman and Baker, 2000) for the self-association of six amino acid segments. The histogram of peptide segments is colored in rainbow from blue to red for segments with low-to-high predicted amyloid propensity. Tau Tr1 (A), TauTR5 (C), and TauTR6 are predicted to form fibrils, but TauTR2 (B) is not. We have previously identified -23 kcal/mol as an empirically-determined threshold for fibrillation (Goldschmidt et al., 2010).

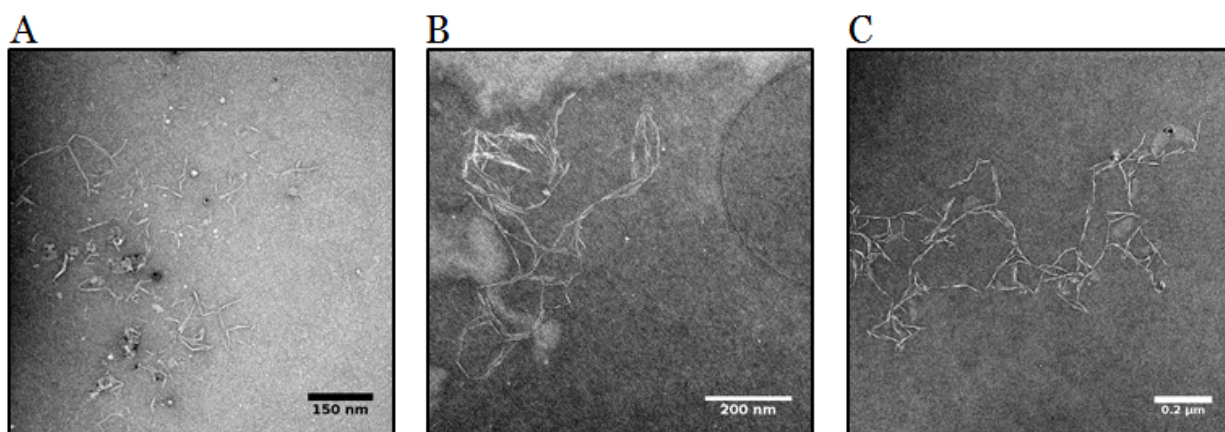


**Figure 5.2: Transmission electron micrographs of amyloid-like fibrils formed by tau tandem repeats TauTR<sub>1</sub> (A), TauTR<sub>5</sub> (B), and TauTR<sub>6</sub> (C).** Fibrils were formed by incubating 10 mg/ml of the purified constructs in PBS at 37° C with agitation for 48 hours. Samples were negatively stained with 2% uranyl acetate. Scale bars represent 150 nm for (A), and 200 nm for (B) and (C).

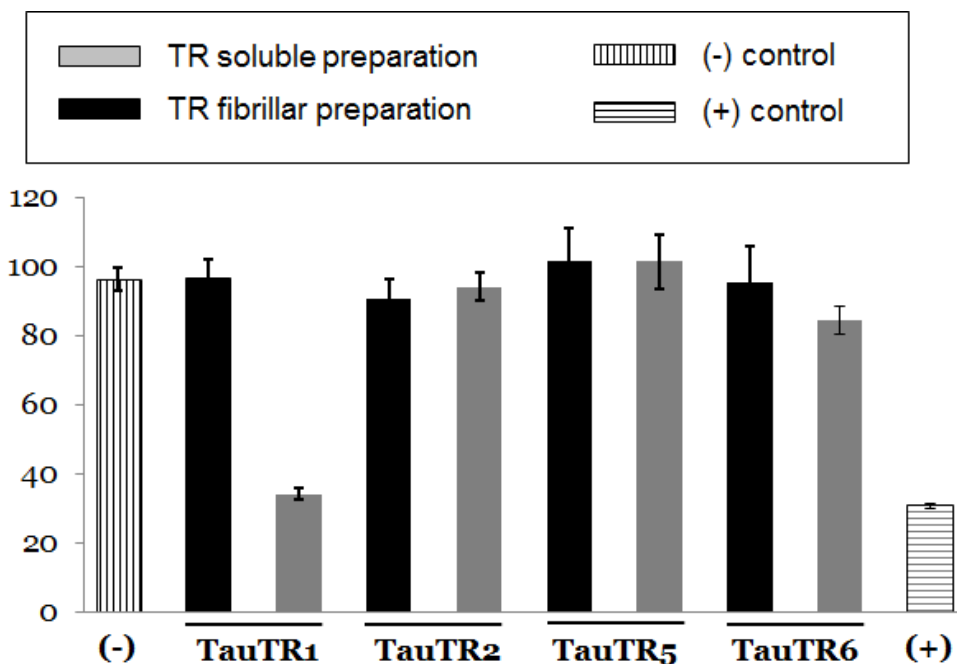


**Figure 5.3: MTT assays indicate that a soluble preparation of TauTR<sub>1</sub> is toxic to a human cell line.** 200  $\mu$ M of tau tandem repeat samples were administered to HeLa cells as fibrillar (black) or soluble (grey) preparations. Viabilities were determined after exposing the cells to samples for 24 hours. PBS buffer alone served as the negative control (vertical hatch) and 1  $\mu$ M of islet amyloid polypeptide oligomers served as the positive control (horizontal hatch) for cytotoxicity.



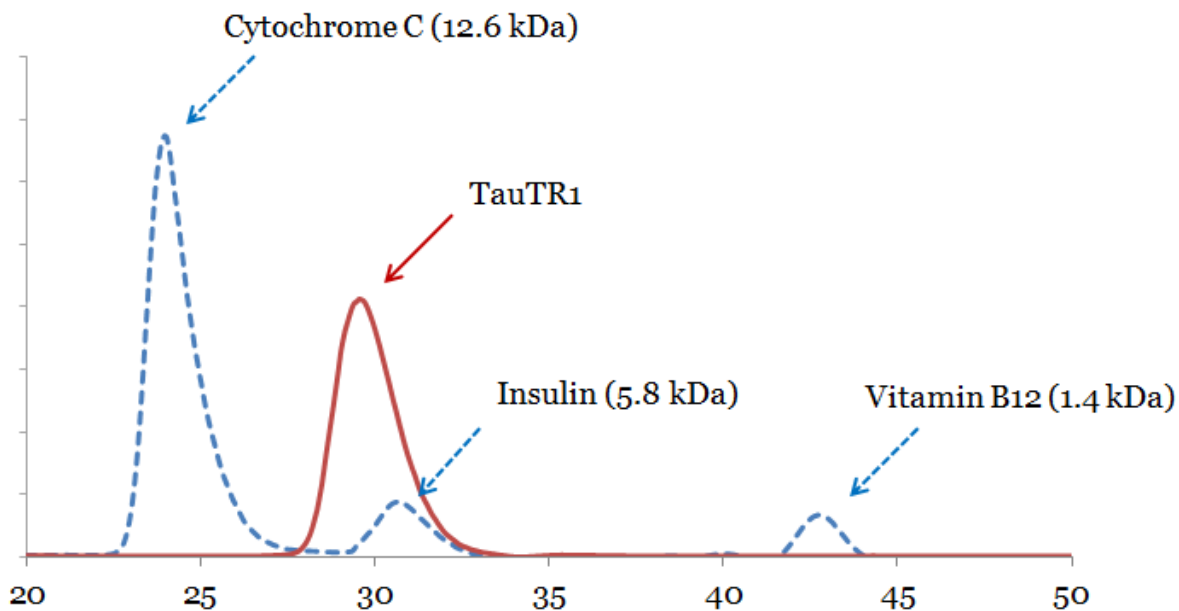


**Figure 5.4: The toxic form of TauTR1 is in an oligomeric state.** Overlaid size-exclusion chromatograms show the elution of protein standards cytochrome C, insulin, and vitamin B12 (dashed curve) with 50  $\mu$ M TauTR1 (solid curve). Chromatograms were obtained using an analytical size-exclusion column (GE HealthcareSuperdex 200 10/300 GL) with phosphate-buffered saline pH 7.0. Standards and TauTR1 were monitored at 280 and 220 nm, respectively.

## References

Ballatore, C., Brunden, K. R., Hurn, D. M., Trojanowski, J. Q., Lee, V. M., and Smith, A. B. 3<sup>rd</sup>. (2012). Microtubule stabilizing agents as potential treatment for Alzheimer's disease and related neurodegenerative tauopathies. *Journal of Medicinal Chemistry*. *55*, 8979-8996.

Berridge, M. V., Herst, P. M., and Tan, A. S. (2005). Tetrazolium dyes as tools in cell biology: new insights into their cellular reduction. *Biotechnology Annual Review*. *11*, 127-152.

Coppola, G., Chinnathambi, S., Lee, J. J., Dombroski, B. A., Baker, M. C., Soto-Ortolaza, A. I., Lee, S. E., Klein, E., Huang, A. Y., Sears, R., Lane, J. R., Karydas, A. M., Kenet, R. O., Biernat, J., Wang, L. S., Cotman, C. W., Decarli, C. S., Levey, A. I., Ringman, J. M., Mendez, M. F., Chui, H. C., Le Ber, I., Brice, A., Lupton, M. K., Preza, E., Lovestone, S., Powell, J., Graff-Radford, N., Petersen, R. C., Boeve, B. F., Lippa, C. F., Bigio, E. H., Mackenzie, I., Finger, E., Kertesz, A., Caselli, R. J., Gearing, M., Juncos, J. L., Ghetti, B., Spina, S., Bordelon, Y. M., Tourtellotte, W. W., Frosch, M. P., Vonsattel, J. P., Zarow, C., Beach, T. G., Albin, R. L., Lieberman, A. P., Lee, V. M., Trojanowski, J. Q., Van Deerlin, V. M., Bird, T. D., Galasko, D. R., Masliah, E., White, C. L., Troncoso, J. C., Hannequin, D., Boxer, A. L., Geschwind, M. D., Kumar, S., Mandelkow, E. M., Wszolek, Z. K., Uitti, R. J., Dickson, D. W., Haines, J. L., Mayeux, R., Pericak-Vance, M. A., Farrer, L. A.; Alzheimer's Disease Genetics Consortium, Ross, O. A., Rademakers, R., Schellenberg, G. D., Miller, B. L., Mandelkow, E., and Geschwind, D. H. (2012). Evidence for a role of the rare p.A152T variant in MAPT in increasing the risk for FTD-spectrum and Alzheimer's diseases. *Human Molecular Genetics*. *21*, 3500-3512.

Cowan, C. M., Quraishe, S., and Mudher, A. (2012). What is the pathological significance of tau oligomers? *Biochemical Society Transactions*. *40*, 693-697.

de Calignon, A., Fox, L. M., Pitstick, R., Carlson, G. A., Bacskai, B. J., Spires-Jones, T. L., and Hyman, B. T. (2010). Caspase activation precedes and leads to tangles. *Nature*. *464*, 1201-1204.

Fatouros, C., Pir, G. J., Biernat, J., Koushika, S. P., Mandelkow, E., Mandelkow, E. M., Schmidt, E., and Baumeister, R. (2012). Inhibition of tau aggregation in a novel *Caenorhabditis elegans* model of tauopathy mitigates proteotoxicity. *Human Molecular Genetics*. *21*, 3587-3603.

Glabe, C. G. (2009). Structural classification of toxic amyloid oligomers. *Journal of Biological Chemistry*. *283*, 29639-29643.

Goldschmidt, L., Teng, P. K., Riek, R., and Eisenberg, D. Identifying the amyloids, proteins capable of forming amyloid-like fibrils. *Proceedings of the National Academy of Sciences, USA*. *108*, 16938-16943.

Hasegawa, M., Smith, M. J., and Goedert, M. (1998). Tau protein with FTDP-17 mutations have a reduced ability to promote microtubule assembly. *FEBS Letters*. *437*, 207-210.

Hoover, D. M., and Lubkowski, J. (2002). DNA Works: An automated method for designing oligonucleotides for PCR-based gene synthesis. *Nucleic Acids Research*. *30*, e43.

Kapust, R. B., Tozser, J., Fox, J. D., Anderson, D. E., Cherry, S., Copeland, T. D., and Waugh, D. S. (2001). Tobacco etch virus protease: mechanism of autolysis and rational design of stable mutants with wild-type catalytic proficiency. *Protein Engineering*. *14*, 993-1000.

Kara, E., Ling, H., Pittman, A. M., Shaw, K., de Silva, R., Simone, R., Holton, J. L., Warren, J. D., Rohrer, J. D., Xiromerisiou, G., Lees, A., Hardy, J., Houlden, H., and Revesz, T. (2012). The MAPT p.A152T variant is a risk factor associated with tauopathies with atypical clinical and neuropathological features. *Neurobiology of Aging*. *33*, 2231, e7-2231.e14.

Kayed, R., Head, E., Thompson, J. L., McIntire, T. M., Milton, S. C., Cotman, C. W., and Glabe, C. G. (2003). Common structure of soluble amyloid oligomers implies common mechanism of pathogenesis. *Science*. *300*, 486-489.

Kodali, R., and Wetzel, R. (2007). Polymorphism in the intermediates and products of amyloid assembly. *Current Opinion in Structural Biology*. *17*, 48-57.

Kopeikina, K. J., Hyman, B. T., and Spires-Jones, T. L. (2012). Soluble forms of tau are toxic in Alzheimer's disease. *Translational Neuroscience*. *3*, 223-233.

Kovacs, G. G., Wöhrer, A., Ströbel, T., Botond, G., Attems, J., and Budka, H. (2011). Unclassifiable tauopathy associated with an A152T variation in MAPT exon 7. *Clinical Neuropathology*. *30*, 3-10.

Laganowsky, A., Liu, C., Sawaya, M. R., Whitelegge, J. P., Park, J., Zhao, M., Pensalfini, A., Soriaga, A. B., Landau, M., Teng, P. K., Cascio, D., Glabe, C., and Eisenberg, D. (2012). Atomic view of a toxic amyloid small oligomer. *Science* *335*, 1228-1231.

Lasagna-Reeves, C. A., Castillo-Carranza, D. L., Sengupta, U., Sarmiento, J., and Troncoso, J., Jackson, G. R., and Kaye, R. (2012a). Identification of oligomers at early stages of tau aggregation in Alzheimer's disease. *FASEB J*. *26*, 1946-1959.

Lasagna-Reeves, C. A., Castillo-Carranza, D. L., Sengupta, U., Clos, A. L., Jackson, G. R., and Kaye, R. (2011). Tau oligomers impair memory and induce synaptic and mitochondrial dysfunction in wild-type mice. *Molecular Neurodegeneration*. *6*, 39.

Lasagna-Reeves, C. A., Castillo-Carranza, D. L., Sengupta, U., Guerrero-Munoz, M. J., Kiritoshi, T., Neugebauer, V., Jackson, G. R., and Kaye, R. (2012b). Alzheimer brain-derived tau oligomers propagate pathology from endogenous tau. *Scientific Reports*. *2*, 700.

Lee, S. E., Tartaglia, M. C., Yener, G., Genç, S., Seeley, W. W., Sanchez-Juan, P., Moreno, F., Mendez, M. F., Klein, E., Rademakers, R., Munain, A. L., Combarros, O., Kramer, J. H., Kenet, R. O., Boxer, A. L., Geschwind, M. D., Gorno-Tempini, M. L., Karydas, A. M., Rabinovici, G. D., Coppola, G., Geschwind, D. H., and Miller, B. L. (2013). Neurodegenerative disease phenotypes in carriers of MAPT p.A152T, a risk factor for frontotemporal dementia spectrum disorders and Alzheimer disease. *Alzheimer Disease and Associated Disorders*. *Epub March 25*.

Liu, C., Zhao, M., Jiang, L., Chen, P. N., Park, J., Sawaya, M. L., Pensalfini, A., Gou, D., Berk, A. J., Glabe, C. G., Nowick, J., and Eisenberg, D. (2012) Out-of-register beta-sheets suggest a pathway to toxic amyloid aggregates. *Proceedings of the National Academy of Sciences, USA*. *109*, 20913-20918.

Mocanu, M. M., Nissen, A., Eckermann, K., Khlistunova, I., Biernat, J., Drexler, D., Petrova, O., Schönig, K., Bujard, H., Mandelkow, E., Zhou, L., Rune, G., and Mandelkow, E. M. (2008). The potential for beta-structure in the repeat domain of tau protein determines aggregation, synaptic decay, neuronal loss, and coassembly with endogenous tau in inducible mouse models of tauopathy. *Journal of Neuroscience*. *28*, 737-748.

Sievers, S. A., Karanicolas, J., Chang, H. W., Zhao, A., Jiang, L., Zirafi, O., Stevens, J. T., Münch, J., Baker, D., and Eisenberg, D. (2011). Structure-based design of non-natural amino-acid inhibitors of amyloid fibril formation. *Nature*. *475*, 96-100.

Stroud, J. C., Liu, C., Teng, P. K., and Eisenberg, D. (2012). Toxic fibrillar oligomers of amyloid-beta have cross-beta structure. *Proceedings of the National Academy of Sciences, USA*. *109*, 7717-7722.

Thompson, M. J., Sievers, S. A., Karanicolas, J., Ivanova, M. I., Baker, D., and Eisenberg D. (2006). The 3D profile method for identifying fibril-forming segments of proteins. *Proceedings of the National Academy of Sciences, USA*. *103*, 4074-4078.

von Bergen, M., Barghorn, S., Li, L., Marx, M., Biernat, J., Mandelkow, E. M., and Mandelkow, E. (2001). Mutations of tau protein in frontotemporal dementia promote aggregation of paired helical filaments by enhancing local beta-structure. *Journal of Biological Chemistry*. *276*, 48165-48174.

Ward, S. M., Himmelstein, D. S., Lancia, J. K., and Binder, L. I. (2012). Tau oligomers and tau toxicity in neurodegenerative disease. *Biochemical Society Transactions*. *40*, 667-671.

Yoshiyama Y., Higuchi M., Zhang B., Huang S. M., Iwata N., Saido T. C., Maeda J., Suhara T., Trojanowski J. Q., and Lee V. M. (2007). Synapse loss and microglial activation precede tangles in a P301S tauopathy mouse model. *Neuron*. *53*, 337-351